Implementing Segmented Ion Trap Designs For Quantum Computing

A thesis submitted for the degree of
Doctor of Philosophy

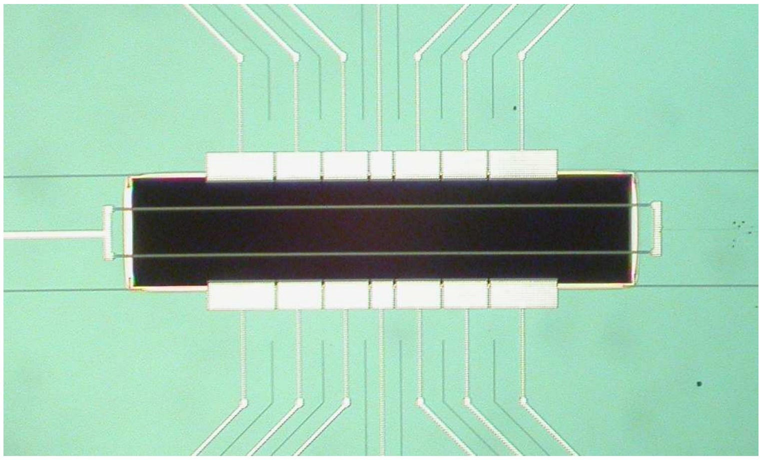

Gergely Imreh

Trinity Term
2008

St Peter's College
Oxford

Abstract

Implementing Segmented Ion Trap Designs For Quantum Computing.
A thesis submitted for the degree of Doctor of Philosophy
Trinity Term 2008

Gergely Imreh
St. Peter's College, Oxford

With all the key elements of quantum computing in ion traps demonstrated by the research community, the focus is now placed on building more sophisticated traps with larger numbers of ions to allow practical scale information processing. One promising avenue is to store ions in and shuttle them between many independent traps which serve as potential interaction sites.

The core of the work described in this thesis is the experimental evaluation of a microfabricated segmented ion trap, built by Sandia National Laboratories ("Sandia trap"). These experiments required construction of a wholly new optical setup including laser and detection systems, a vacuum system and control electronics. Among our experimental achievements were: successful loading of single and pairs of ions in the microscale trap, measurement of ion storage lifetime, measurement of the motional heating rate with a time-resolved Doppler-cooling method — which showed above than average heating, and implemented a single-ion shuttling method — which reliably transferred the ion through a distance of $360\,\mu$m (two DC electrode widths away) and back. These results have been used to improve the next version of the Sandia trap design.

We also used computer modelling to study several aspects of ion traps: a mesoscopic ion trap designed for fast ion separation, simulated ion loading to quantify requirements for successful trapping in small and shallow traps, and analyzed a precise shuttling method — where the time dependence of the trapping potential is engineered such that there is minimal motional heating.

The results show that ion trap arrays at the $100\,\mu$m distance scale are feasible and suggests that such multiple trap designs merit further study.

Acknowledgements

I wish to say thanks to my supervisor, Professor Andrew Steane, who gave me a chance to study at one of the best places in the world for physics and guided me through these years. I am also extremely grateful for all fellow ion-trappers, past and present. To Professor Derek Stacey, whose logic was always there to help and never got tired of my questions; David Lucas, whose knowledge of every single knob in the lab and every variable in our software was invaluable, just as much as his enthusiasm; to Jonathan Home, Simon Webster, Matthew McDonnell, Nick Thomas and Jeff Sherman who showed me where I should be headed if I want to be a good researcher; to David Szwer, Spike Curtis, Alice Myerson and David Allcock for the long nights shared in the lab as well as the long chats every tea time, and for all the fun that is doing research in physics; to Graham Quelch and Rob Harris for their cheerful help in all things electronic and mechanical. I will certainly miss your company.

I must say thanks all my friends in St. Peter's College Middle Common Room and in many other colleges, who have shown me a completely different way one can be attached to people. Being Social Secretary for a year at St. Peter's gave me a chance to give back a little for all the things I got from you.

I want to say thanks to my parents, who brought me up to be a really curious person and encouraged me all the way: Köszönöm!

And I owe a lot to YuJie, who supported me in the lows and shared the highs with me. Thank you.

Contents

List of Figures

Chapter 1

Introduction

> *“[W]e choose to go to the moon [...] and do the other things, not because they are easy, but because they are hard...”*
>
> **John Fitzgerald Kennedy**

Undoubtedly, we are living in an Age of Information, which is made possible by the advances in computer science. Miniaturisation has enabled the manufacture of increasingly powerful computers. As the individual components of such classical computers become smaller, they are nearing a regime where progress is complicated by quantum mechanical effects. Materials have unwanted behaviour when constructed in nanometre scale layers. Quantum tunnelling leads to current leaks, unreliable calculations, reduced power efficiency, and so on. Quantum mechanics, however, can be used to our advantage as well, allowing us to process information in previously unattainable ways.

Richard Feynman [1, 2] proposed the idea of the universal quantum simulator, which is capable of simulating the physical behaviour of any quantum system. Since all computer operations are physical processes, this would be a universal computer as well. David Deutsch [3] developed this idea into a set of requirements for a universal quantum computer. In his network model [3], the information is stored in two-state quantum systems (qubits) and the computer manipulates these qubits. It has been shown [4, 5] that it is sufficient to implement one- and two-qubit quantum gates for universal computation. The measurement of these qubits provides the output of the computing process.

Theoretical work in the field of quantum information processing showed that certain mathematical problems could be computed more efficiently in a quantum computer than in any classical computer. There are a number of such "quantum algorithms"; important examples are Shor's factorizing algorithm [6] and Grover's search algorithm [7]. Both rely on entanglement to give a result much more quickly than classical computation.

Many different physical systems have been proposed for quantum information processing, including nuclear magnetic resonance (NMR) [8], photons [9], Josephson junction circuits [10], quantum dots [11], trapped neutral atoms [12, 13] and ions [14, 15]. NMR has been used to demonstrate small quantum algorithms, but faces great difficulty in scaling the system up to many qubits and operations. Photonic qubits deliver high fidelity single qubit operations and measurements, but implementing multi-qubit operations is challenging. Ion traps are among the most advanced of these technologies; indeed, all key functions of a quantum computer have already been demonstrated.

Research groups with a good deal of experience with these techniques include NIST in Boulder, the Institute for Quantum Optics in Innsbruck, the University of Maryland[1], the University of Oxford, the University of Aarhus, Denmark, the University of Barcelona and the University of Ulm. The landmark results in quantum computing experiments have so far emerged primarily from NIST, Innsbruck, Michigan and Oxford.

A Controlled-NOT gate proposed by J. I. Cirac and P. Zoller [14] was implemented by the NIST group [16] and the Innsbruck group [17]. It was followed by deterministic entanglement of four ions [18], a controlled-phase gate with 97% fidelity [19], basic quantum error correction [20], quantum state teleportation [21], creation of a 6-qubit Schrödinger cat state [22], 8-qubit entanglement [23], ion-photon entanglement [24], demonstration of the Deutsch-Jozsa algorithm [25], a basic implementation of Grover's search [26], and a simple quantum Fourier transform [27].

Ion trapping groups use different species of ions for their experiments. The most common ones are Be^+, Mg^+, Ca^+, Cd^+, Ba^+, Yb^+ and Hg^+. There is no obvious choice for ion species used in large scale ion trap arrays, and practical quantum information processors might even use a number of different species for different purposes (information storage, cooling, etc.). Some of the issues regarding this problem are covered in [28, 29].

---

[1] The group moved from the University of Michigan in 2007.

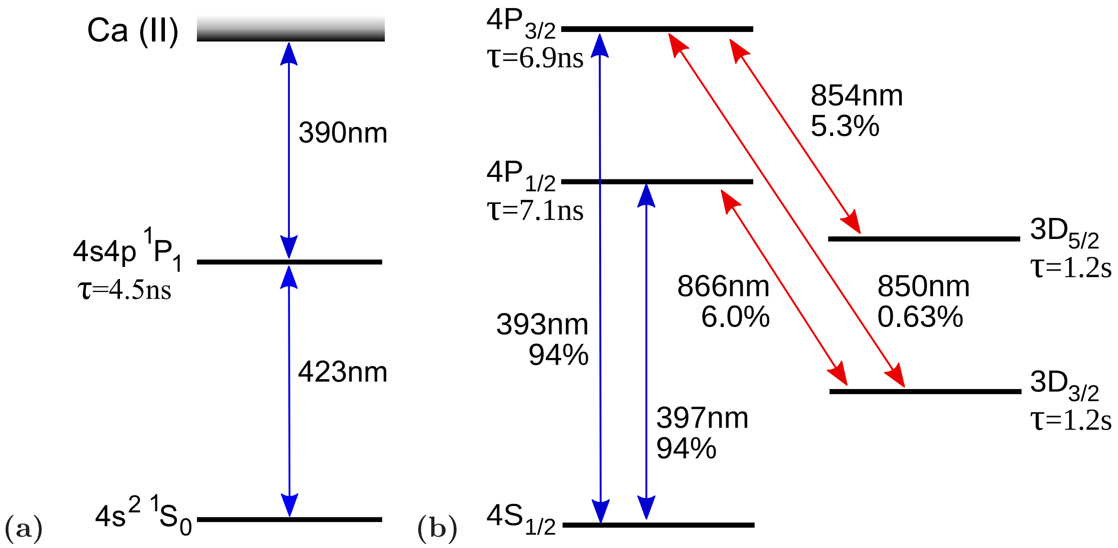

Figure 1.1: Level structure of (a) neutral Ca and (b) Ca^+. The wavelength of the transitions are noted, as well as the level lifetimes and branching ratios in the case of Ca^+.

In the Ion Trap Quantum Computing Group at the University of Oxford, Ca^+ ions are used. One of their advantages is that all relevant energy levels are addressable by diode lasers without frequency doubling, even including those in the neutral atom involved in the ionizing process, see Figure 1.1. Experiments in Oxford included Schrödinger's cat states [30], deterministic entanglement of a pair of spin qubits [31], long lived memory qubits with $T_2 \gtrsim 45\,\mathrm{s}$ [32], qubit readout with 99.991(1)% fidelity [33], and sympathetic cooling with two different isotopes of Ca [34]. These experiments were conducted in a linear Paul trap with a single trapping region.

1.1 The transition to microfabricated trap arrays

The focus of research is now placed on more sophisticated trap designs, to allow larger scale information processing with large numbers of ions. The present thesis represents a contribution to this research.

The most popular approach is to use an array of ion traps with the ions being moved between the different trapping regions. Other ideas include using photonic qubits to couple together ion qubits at separate trapping regions, or using a large array of ions in a single trap.

The issue is now how to build multiple trap arrays. This approach of scaling up is being tackled by different research groups with a number of prototype traps. However there is no consensus about the ideal trap design and ion confinement in such trap arrays is in itself a major achievement. Surface traps [35], two [36] and three layer [37] structures are competing in terms of ease of manufacturing, trap stability, trapping strength, electric field noise and ease of optical access. Methods of shuttling ions [37, 38] as well as splitting and joining pairs of ions [37] in such traps are also an important area of investigation. The first successful loading of ions in a microfabricated trap was reported in 2006 by the Michigan [36] and NIST groups [35]. It was recognised in the "Scientific American 50" awards for 2006.

The work presented in this thesis has two major parts: computer modelling and theoretical description of segmented ion traps and their operation, and experimental evaluation of one microfabricated segmented ion trap. A completely new optical, electronic and vacuum apparatus was built to facilitate this and further studies of novel traps. A microfabricated trap array (electrode size of order $10\,\mu$m) was built at Sandia National Laboratories, with design input from an international team including our group. Ion loading and experiments in this trap are presented in Chapters 4-7. This was the first observation of ions in a microfabricated trap outside the USA.

A trap with an unusual three-layer geometry, designed for fast ion separation, is also modelled theoretically in Chapter 2, and issues relevant to its operation are explored. The trap itself has subsequently been successfully commissioned and use to trap ions.

The other theoretical studies presented in this thesis concern the issues of loading ions into small, shallow traps, and transporting ions through trap arrays with high speed and low heating. The former helped us to optimise the parameters for loading the Sandia trap, and should prove similarly helpful in future work with small traps. The latter introduces a method to allow the exact transport function of the potential well to be calculated, to make the ion follow a desired trajectory. This improves on previous treatments where transport functions were identified by trial and error or optimized imperfectly. A modest experimental demonstration was achieved by shuttling ions through the Sandia trap array.

1.2 Thesis layout

The first two chapters contain the theoretical topics of the thesis. Chapter 2 presents our computer modeling of ion traps, in particularly a mesoscopic segmented ion trap designed for fast ion separation and constructed by the University of Liverpool. The trap's behaviour is studied and the effect of micromotion and of manufacturing imperfections is explored. A microfabricated segmented ion trap design (prepared by Sandia National Laboratories, USA) is also introduced and modelled.

Chapter 3 contains theoretical calculations of two topics concerning ion traps. The first is the reliable, fast transport of ions with low heating. The second is a numerical simulation study of ion loading in the Sandia trap, performed to understand voltage and atomic beam requirements for successful ion trapping.

The subsequent four chapters contain the description of experiments with the Sandia trap. Chapter 4 introduces the experimental setup: the vacuum system, the laser system, the optical layouts. Since the experiment was built up from scratch, the chapter includes observations of several issues encountered, including unusual laser modes, the stability of polarisation and the effect of the air conditioning system. Chapter 5 describes the preparation of the vacuum system as well as the first observation of neutral atom fluorescence in the Sandia trap. The neutral atom density in the trap and thus the calcium oven temperature is deduced. Chapter 6 describes details of a number of experiments to characterize the behaviour of the Sandia trap. Ion loading, micromotion compensation, ion lifetime estimation, trap frequency measurements and multiple ion loading are presented. Chapter 7 first describes the characterization of the Doppler-cooling beams, which is important for the experiments to measure the heating rate of the ion trap. Heating rate measurements are then presented using time-resolved fluorescence during Doppler-cooling of ions. Finally, experiments implementing single ion shuttling in the Sandia trap are presented. Chapter 8 gives a summary and conclusion.

Chapter 2

Numerical modelling of multiple-electrode traps

To predict the behaviour of ion traps, generally computer models of the traps are created and their operation is simulated. This chapter discusses this modelling, the particular ion trap designs used in our research group and results of simulations of two previously untested designs. Further information on the software is continued in the appendices.

2.1 Ion trap modeling

The main aim of a numerical model of an ion trap is the prediction of potentials created by DC and radio-frequency voltages applied to the electrodes. The highest frequency RF fields used are of order 10 MHz, thus wavelengths are of order 10 m. Since the characteristic size of the ion traps is $< 1\,\mathrm{mm}$, quasi-static modelling is a good approximation.

There are two widely used methods to solve Laplace's equation in the region around an ion trap: the Finite Element Method (FEM) and the Boundary Element Method (BEM). Both find approximate solutions of partial differential equations. In FEM, the whole volume of interest (the electrodes and the free space in between them) is subdivided into a discrete mesh of nodes. The nodes are connected to their neighbours by linear or quadratic functions. An energy minimization algorithm is then used to calculate the potential on the mesh, subject to boundary conditions (voltages applied to the electrodes).

The BEM attempts to solve partial differential equations by forming them into integral equations. As opposed to FEM, in BEM only the surfaces are subdivided. The method uses boundary conditions to find the boundary values to the integral equations. When the BEM is applied to ion traps, one finds the charge distribution on the electrodes subject to electrode geometry and applied voltages. Then the potentials can be calculated at arbitrary positions in the space between the electrodes.

Each method has advantages and disadvantages. Since in BEM only surfaces are discretized as opposed to volume discretization in FEM, BEM scales better when larger structures are modelled. However, because in FEM only neighbouring nodes are connected, the matrix describing the system of equations of the model is very sparse; the number of non-zero elements in the matrix scales as $O(n)$ with the number of nodes n. In BEM all subdivisions of an object (such as an electrode) are described by joint boundary conditions. Thus, the matrix describing the model is usually densely-packed, and the number of non-zero elements in the matrix scales as $O(n^2)$. In BEM, the potential can be calculated at arbitrary positions, while in FEM the potential is given only at the nodes and approximated in between. FEM can incorporate material inhomogeneities, while the BEM only deals with linear homogeneous materials.

Due to these differences, the efficiency and speed of the calculations is highly dependent on the design to be modelled. Both methods have several implementations (FEM: Opera[1],SIMION[2]; BEM: CPO[3]). For ion traps with relatively simple geometry and small/medium number of electrodes, the BEM method proved to be efficient, and the results presented here were obtained using Charged Particle Optics (CPO) by Scientific Instrument Services.

Due to the linear nature of Laplace's equation, potentials generated by the different electrodes are independent and can be calculated separately. Generally, unit voltage is set on a selected electrode i, while all other electrodes are grounded. The potential $\phi_i(\vec{r})$ is then calculated at the position of interest $\vec{r}$. The calculation is repeated with all other electrodes. This procedure is the same for both DC and RF electrodes, because of the

---

[1] Vector Fields Opera, `http://www.vectorfields.com/`

[2] Scientific Instrument Services, Inc., `http://www.simion.com/`

[3] Charged Particle Optics, SIS Inc., `http://www.simion.com/cpo/`

quasi-static approximation. The electric potential set up by a given voltage configuration is then given by

$$\phi(\vec{r},t) = V_{\mathrm{rf}}\phi_{\mathrm{rf}}(\vec{r})\sin(\Omega_{\mathrm{rf}}t) + \sum_i V_i\phi_i(\vec{r}) \tag{2.1}$$

where V_{rf} and V_i are the voltages on the RF electrode and DC electrodes, and Ω_{rf} is the RF drive frequency. Equation 2.1 is used when a complete description of the ion's motion (both secular and micromotion) is sought. If only the secular motion of the ion is of interest, the effect of the RF field on the secular motion can be approximated by the RF pseudopotential

$$U_p(\vec{r}) = \frac{q^2V_{\mathrm{rf}}^2}{4m\Omega_{\mathrm{rf}}^2}|\nabla\phi_{\mathrm{rf}}(\vec{r})|^2 \tag{2.2}$$

where q and m are the charge and mass of the ion. Thus the complete expression for the potential energy in the pseudo-potential approximation is

$$\Phi_p(\vec{r},t) = \frac{q^2V_{\mathrm{rf}}^2}{4m\Omega_{\mathrm{rf}}^2}|\nabla\phi_{\mathrm{rf}}(\vec{r})|^2 + q\sum_i V_i\phi_i(\vec{r}) \tag{2.3}$$

The simulations were performed as follows. A model of the trap was created in the structural description language of CPO. Locations of interest were chosen, e.g., positions along the trap axis, or points to represent 2D cross sections in the radial direction at different positions along the trap axis. We then proceeded as above; setting the voltage of a single electrode to unity while keeping everything else grounded we calculated $\phi_i(\vec{r})$ for one electrode at the locations of interest. This process was repeated for all electrodes (both DC and RF). The resulting potential was stored in a database, and was used in a numerical computation software, such as Matlab[4] or GNU Octave[5] to calculate the potentials at the location of interest for arbitrary voltage configuration on the electrodes, as needed by the experiments.

---

[4] The MathWorks, Inc., http://www.mathworks.com/

[5] GNU Octave, http://www.gnu.org/software/octave/

2.2 Trap designs

The evolution in ion trap design can be illustrated by the different ion traps that are in use and are planned in our research group.

Macroscopic traps are manually assembled, and have ion-electrode separation of order $\approx 1\,\mathrm{mm}$. Advantages of macroscopic traps include generally a low heating rate and a large trap depth which result in very long ion lifetimes. The design is tried and tested, and the trap is relatively cheap to produce. Its disadvantages are its lack of scalability to a large number of ions due to its single trapping region and the difficulty of achieving high trap frequencies because of the large voltages required as a consequence of the large electrode-ion distances. The first ion trap in our research group, a linear Paul trap, is an example of a macroscopic trap (see [39]).

Mesoscopic traps present a transition stage between traditional style traps with a single trapping region and microscopic traps with good scalability. Built using traditional methods, they nevertheless can have multiple trapping regions and provide a testing ground of procedures being developed for microscopic traps. However, the manual assembly can be a weak point because imprecisions have a magnified effect as the ion trap design is scaled down in size. The Liverpool trap, described in the next section, is a mesoscopic ion trap.

The smallest kind are microscopic ion traps. They can have very high trap frequencies even with low electrode voltages, a large number of trapping regions for dealing with multiple ions, and precise manufacturing by microfabrication methods. However, while some of the microfabrication methods are well-established (e.g. because of their use in computer chip manufacturing industry), some are highly experimental and can have a significant error-rate. Another disadvantage is the smaller trap depth and higher heating rate compared to larger traps. Small scale production of microscopic traps is very expensive, but a successful mass-produced design would be much cheaper. Examples of microscopic traps include the Sandia trap (see Section 2.4), and the traps designed by the MICROTRAP Consortium[6].

---

[6] MICROTRAP Consortium, `http://www.microtrap.eu/`

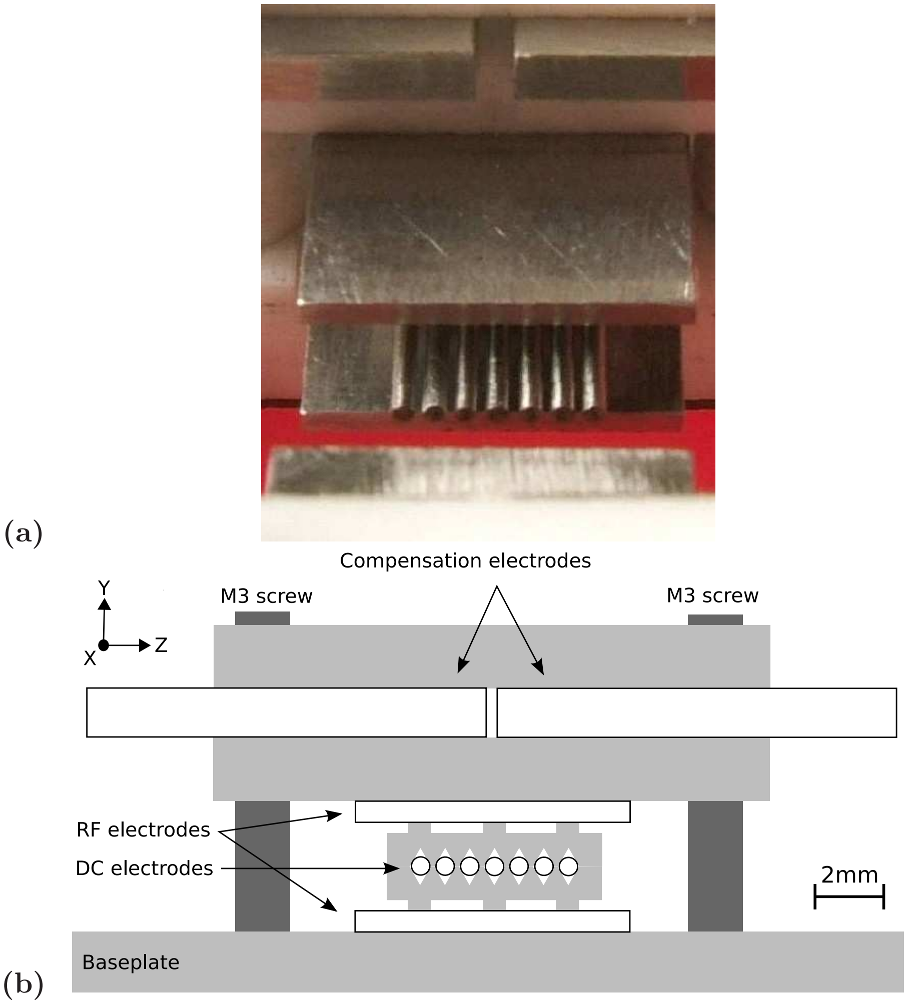

Figure 2.1: a) A view of the Liverpool trap, b) Cross-section of the trap. The DC electrodes are specified to have a nominal diameter of 0.5775 mm, and axis-to-axis separation of 0.7525 mm. The electrodes are separated by machined Macor blocks (light gray areas on the plot), and the structure is assembled using M3 non-magnetic steel screws (dark gray). The smallest ion-electrode distance is 0.7 mm.

2.3 The Liverpool trap

The Liverpool trap (see Figure 2.1) was built by S. Taylor and B. Brkic from the University of Liverpool. Its electrodes are machined from non-magnetic stainless steel, and separated by Macor (a type of machinable glass ceramic) spacers. It is a three layer-design, with DC electrode "fingers" in the middle layer and RF electrodes below and above. A set of 4 compensation electrodes is also present to adjust for stray fields, mostly in the direction perpendicular to the plane of the DC electrodes (Y direction).

2.3.1 Design of the trap

The Liverpool trap has an unusual design. Most experiments involving the transport of ions among multiple trapping zones have adopted a design philosophy in which the RF potential is as smooth as possible. To achieve this one can, for example, make the DC electrodes have the shape of a single long electrode, extending either side of the trap axis Z, interupted by narrow cuts to make the segments. This allows structure to be introduced in the DC potential as a function of Z, while the RF ground at these electrodes is consistent with a smooth RF potential, almost without variation in the Z direction.

A problem that arises with small traps, however, is electric field breakdown. One wants to have tight trapping potentials, but if the DC electrodes are close to one another and have sharp edges then the problems of field emission and breakdown of insulating surfaces are exacerbated. This issue was studied theoretically in [40], and a number of trap geometries were modelled. The issue of trap tightness arises especially when one wants to split apart or join together strings of ions. During such a "split" or "splice" operation, the potential as a function of z must change from the usual simple quadratic function to a quartic function, so that two wells with a barrier in between them can be formed. To achieve this without reducing the confinement places the most stringent conditions on the electric field breakdown. Therefore in [40] a geometric factor γ was defined as

$$\gamma = \frac{\beta \rho^3}{E_{\max}} \tag{2.4}$$

where β is the coefficient of the quartic term in the DC potential $\sum_i V_i \phi_i(z)$ along the trap axis at the origin, ρ is the distance of the origin to the nearest electrode surface, and $E_{\max}$ is the largest electric field at any electrode surface. By this measure, a "good" trap structure would have a high value of γ.

Another important issue is the tightness of the RF confinement. In large traps this is typically limited by the size of the available RF voltages, but in a small trap the voltages are manageable and again electric field breakdown presents an important limit. This can be characterised by another geometric factor

$$\mu = \frac{Q_{\rm ac}\rho}{E_{\rm max}} \tag{2.5}$$

where $Q_{\rm ac}$ is the coefficient of the quadratic term in the potential $\phi_{\rm rf}$ generated by the RF electrodes at the trap centre.

In [40] it was shown that a geometry that achieves a good combination of values for these geometric factors consists of a row of DC "fingers" nearest to the trap axis, with RF electrodes above and below and set back somewhat. It is this geometry that the Liverpool trap was designed to realise. This trap is not microfabricated. It has a larger (of order 1 mm) scale, so will not suffer from electric field breakdown at the voltages we can achieve, but it will enable us to test whether this approach is viable. In particular, this type of geometry results in much more structure in the RF potential along Z than is the case in the "traditional" approach. This means the ions will undergo considerable micromotion at most positions along the trap axis. We will be able to test whether this micromotion in practice leads to problems when ions are moved along the trap axis, or when ion strings are split and recombined.

In the pseudopotential model, the RF oscillation is perfectly harmless: it merely contributes to the total potential experienced by the ion and thus influences the location of the "trap centre" at any given configuration of the DC voltages. Numerical modelling taking the RF oscillation into account also suggests that it need not be a problem. However, practical experience with trapped ions has given evidence, albeit inconclusive, that micromotion can be associated with heating or other problems. It is not yet known whether or not this will prove to be a significant issue, so it is one aim of the planned work with the Liverpool trap to resolve this.

In the next section we will present the main characteristics of the trap, such as the expected potential in the radial and axial directions, as a function of position along the axis, and comment on how the DC voltages are chosen to realise a given desired situation. We also briefly study the issue of manufacturing imprecision.

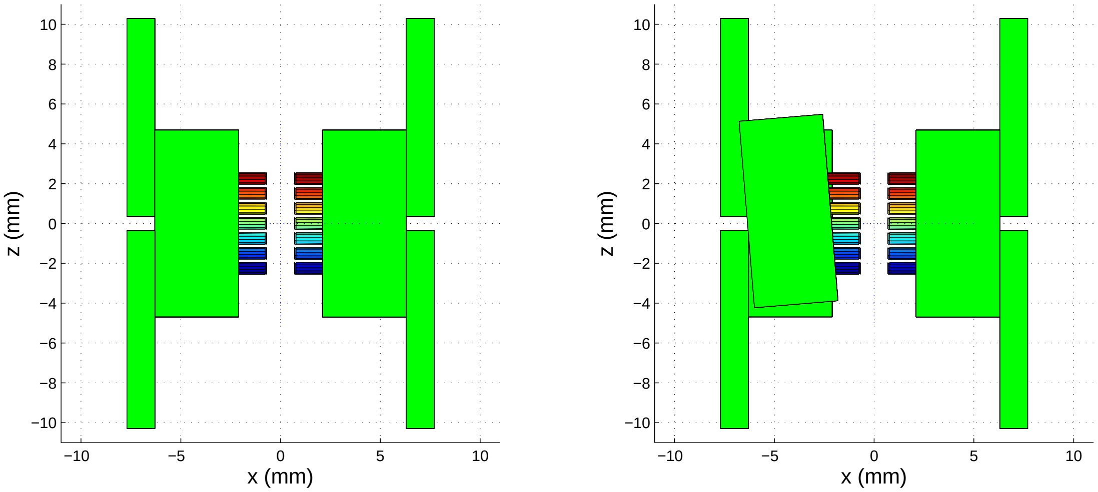

Figure 2.2: Computer models of the Liverpool trap, as used in the simulations. The trap is viewed from above (along the Y axis, see Figure 2.1 for note on directions). (Left) The Liverpool trap as it was designed. (Right) The trap with one of the RF electrodes twisted and displaced, as it was found to be after assembly. The electrode is displaced by $\Delta z \approx 0.9\,\mathrm{mm}$,$\Delta y \approx 0.3\,\mathrm{mm}$ and twisted by $\theta \approx 4.7^\circ$ in the X-Z plane. The model is based on photographs taken of the trap. (Colour in electronic version)

2.3.2 Analysis of trap geometry

Figure 2.2 shows the trap's computational model, looked at from the Y direction. The first version (Figure 2.2, left) corresponds to the originally intended design, and used for benchmark calculations, to explore the expected behaviour of the Liverpool trap.

As an illustration, Figure 2.3 shows the calculated electric field potential in the $X-Y$ plane at the trap centre, when the DC electrodes are grounded and the RF electrodes are at the set voltage.

Figure 2.4 shows a calculation of voltages on the DC electrodes to produce a single $\omega_{\mathrm{dc}}/2\pi = 1\,\mathrm{MHz}$ potential well at an arbitrary position along the trapping axis (the Z direction). The RF voltages are not included because in the ideal situation the RF field has no component in the axial direction. The computational model can be used to derive the voltage configuration in the case of different constraints, such as 2 or 3 trapping regions (instead of only 1) or with different oscillation frequencies. This is useful in the ion-shuttling experiments, for example.

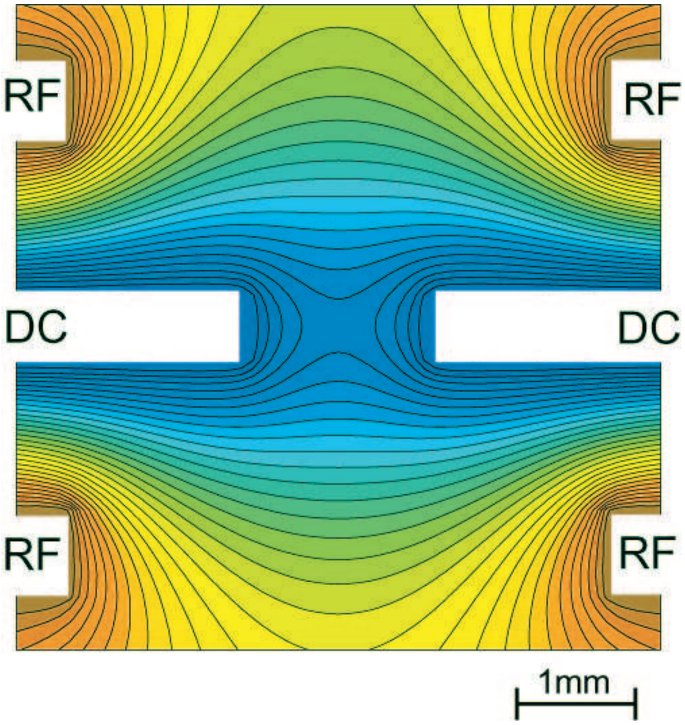

Figure 2.3: Electric field due to a fixed voltage on the RF electrodes in the Liverpool trap. Cross section in the X-Y plane, as shown in Figure 2.1b.

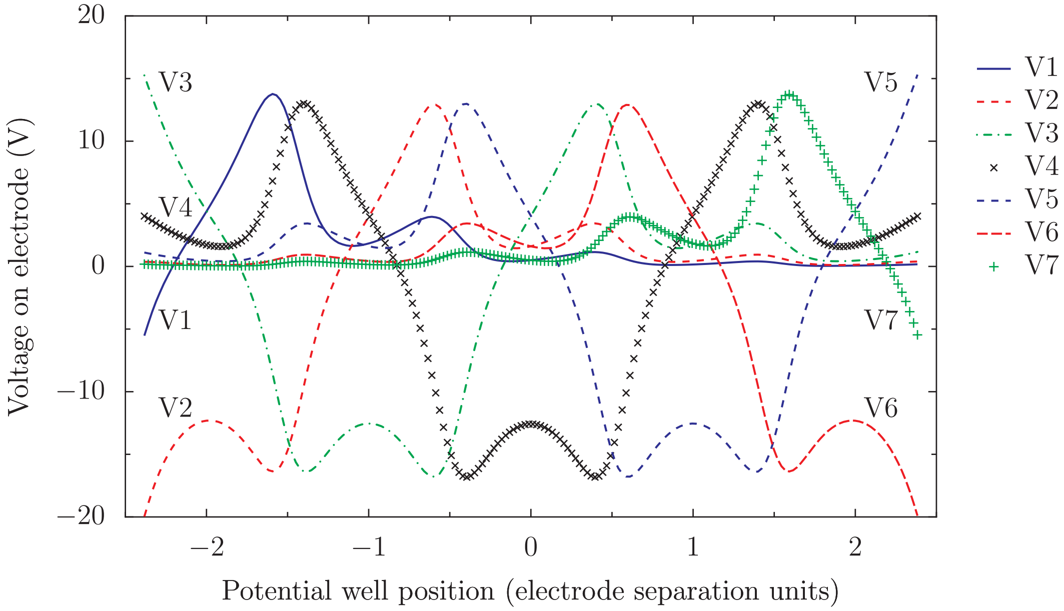

Figure 2.4: Voltages on electrodes to generate a single DC potential well with $\omega/2\pi = 1\,\text{MHz}$ as a function of well position along the axis. Position is shown relative to the centre positions of the 7 DC electrodes. The electrode-electrode separation is nominally 0.7525 mm. Positions left of electrode -2 and right of electrode +2 are not shown, as it is not possible to trap in those regions. (Colour in electronic version)

The geometric factors γ and μ, defined in Equations 2.4 and 2.5 respectively, can also be calculated. One finds

$$\gamma \simeq 0.02, \tag{2.6}$$

$$\mu \simeq 0.146. \tag{2.7}$$

The Liverpool trap was designed to have high γ value compared to other traps (see e.g. Section 2.4), which facilitates ion pair splitting.

A point of interest is the effect of the segmented DC electrodes on the RF field along the trapping (Z) axis. The main effects can be understood by expanding the RF potential at any point z_0 as a power series in $z - z_0$, and examining the first few terms:

$$\phi_{\mathrm{rf}}(z) \simeq \phi_{\mathrm{rf}}(z_0) + a(z - z_0) + b(z - z_0)^2 \tag{2.8}$$

where

$$a = \left.\frac{\mathrm{d}\phi_{\mathrm{rf}}}{\mathrm{d}z}\right|_{z_0}, \qquad b = \frac{1}{2}\left.\frac{\mathrm{d}^2\phi_{\mathrm{rf}}}{\mathrm{d}z^2}\right|_{z_0}. \tag{2.9}$$

The size of the oscillating electric field is given by a. It is important because it causes micromotion, see Figure 2.6 (right). The micromotion maximum velocity reaches some hundreds of m/s at the extreme trapping positions, under typical operating conditions. This will complicate laser interactions with the ions at those locations, suggesting that they could be used for storing ions temporarily but not for logical quantum gate operations.

In the pseudo-potential approximation (Equation 2.2), the contribution to the potential energy (i.e. the function describing the secular motion) is proportional to

$$|\nabla\phi_{\mathrm{rf}}|^2 = a^2 + 2ab(z - z_0) + 4b^2(z - z_0)^2 \tag{2.10}$$

The constant offset a^2 has no effect on the motion. The linear term represents a force which displaces the local trapping centre slightly away from the location calculated from the d.c. potential alone; the quadratic term represents a (small) increase in the confinement along Z.

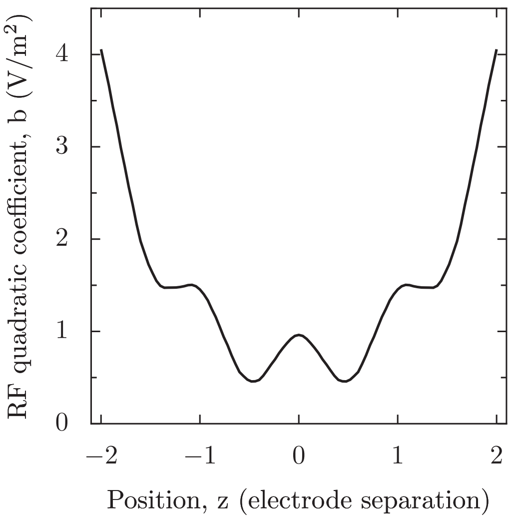

Figure 2.5: The quadratic coefficient b in the expansion of the RF field along the Z axis, as a a function of position along Z (see Equation 2.9). The shielding effect of the DC electrodes appears as “bumps” at the position of the DC electrodes.

Figure 2.5 shows the quadratic coefficient as a function of z. At electrode positions 2 and -2 the effect is to increase the secular frequency from 300 kHz (DC well) to 320 kHz (DC plus RF). Figure 2.6 (left) shows the displacement of the trapping centre away from that calculated from the DC potential, when the vibrational frequency in the DC potential well is 300 kHz. It is seen that the displacement is a small correction that needs to be taken into account.

2.3.3 Effect of manufacturing imprecision

The actual trap geometry differs from the design. The most obvious difference is the displacement of one of the RF electrodes, possibly during assembly. Figure 2.2 (right) shows the computer model of the trap with the twisted RF electrode. The displacement of the electrode was estimated from photographs, which suggests $\Delta z \approx 0.9\,\mathrm{mm}$,$\Delta x \approx 0.3\,\mathrm{mm}$ and a twist of $\theta \approx 4.7^\circ$ in the X-Z plane. Rather than reassemble the trap, it was decided to operate it with this substantial asymmetry, in order to learn whether in practice this degree of manufacturing imprecision is a problem. An additional defect, the two lines of DC electrodes appear to have been shifted relative to each other, along the trap axis, by as much as half an electrode width ($\approx 290\,\mu$m). Precise measurements of this shift and

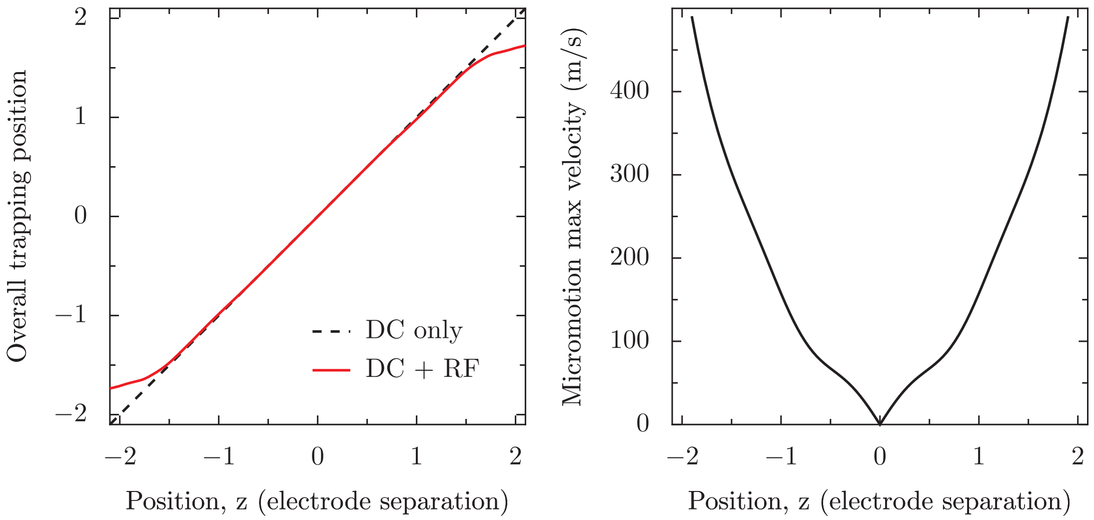

Figure 2.6: (Left) The position of the pseudo-potential well as a function of the position of the DC potential well along the trap axis. (Right) The estimated micromotion of the ion in the Z direction due to the non-zero RF axial quadratic coefficient. In both cases, parameters are set to typical operating values: $\omega_{\mathrm{dc}}/2\pi = 300\,\mathrm{kHz}$, $V_{\mathrm{rf}} = 200V$ and $\Omega/2\pi = 5.92\,\mathrm{MHz}$.

evaluating its implications still to be investigated.

First we simulated the trap with the displaced RF electrode. When compared to the benchmark simulations, the most notable difference was in the position of the RF minima in the radial directions (X and Y). Figure 2.7 shows the position of the RF minima as a function of location along the Z axis, in the original design and the one with the twisted electrode.

The original design is symmetrical in the X direction (across the trap), thus the location of the RF minimum is at the trap centre. In the twisted electrode model, the symmetry is broken and the minimum is displaced, though through a relatively small distance ($\sim 1\,\mu$m maximum). In the Y direction (perpendicular to the plane of the DC electrodes) the RF minimum is already displaced from the geometrical centre of the RF electrodes (which is the origin of the scale presented in Figure 2.7(right)). This is due to the symmetry breaking of the compensation electrodes. In the twisted electrode model the RF potential minimium is displaced by up to $6\,\mu$m compared to the benchmark model. The 4 compensation electrodes were designed to allow compensation for just this sort of contingency. With them, it is possible to match the DC minimum to the RF minimum for up to 2 different

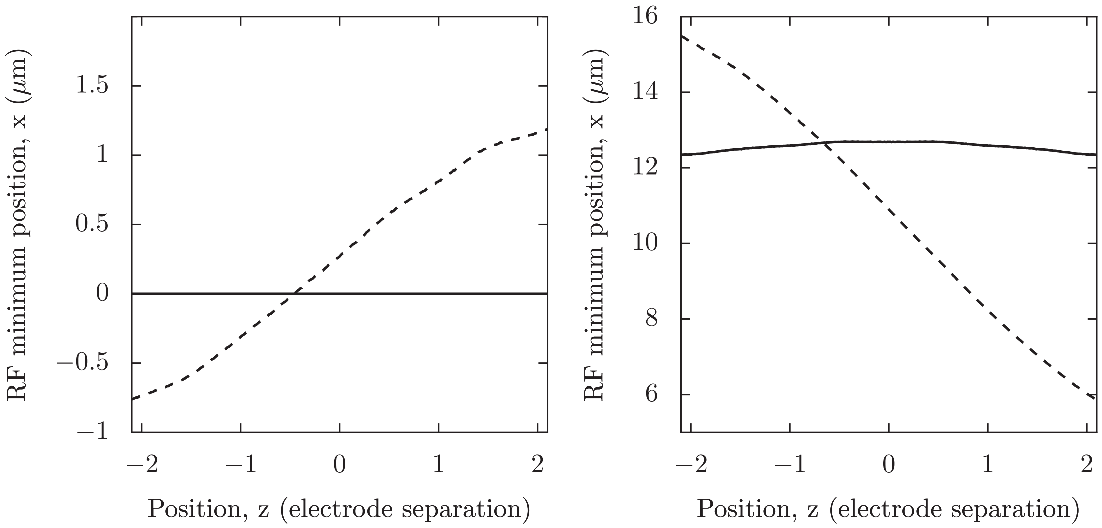

Figure 2.7: The position of the RF minimum as function of position along the trap axis, (left) in the X direction, across the trap, (right) in the Y direction, perpendicular to the plane of DC electrodes. The solid line is for the model as designed, the dashed line shows the effect of the twisted RF electrode. In the X direction the change is smaller ($\sim 1\,\mu$m maximum), while in the Y direction the twist causes more substantial changes.

positions in the trap.

Recently the Liverpool trap has been tried in experimental conditions. Ions were trapped and initial trap frequency and compensation measurements were performed.

2.4 The Sandia trap

Another trap design was simulated, a DTO Module 4 ion trap (or “Sandia trap”) provided by Sandia National Laboratories in Albuquerque, New Mexico, USA. It has a planar electrode arrangement on a chip carrier (Figure 2.8). 14 DC control electrodes are arranged around a $2000\,\mu\text{m} \times 400\,\mu\text{m}$ slot cut into the carrier. The DC electrodes have $7\,\mu$m separation and have lengths of $100\,\mu$m (centre electrode), $200\,\mu$m (next two electrodes either side) and $300\,\mu$m (the outermost electrodes). Along the slot, there are 2 RF rails, approx. $10\,\mu$m wide and $200\,\mu$m apart. The sides of the slot were coated with gold and electrically connected to the common ground (“ground plane”). The trapping axis is along the slot, in between the RF rails. Experiments with this microfabricated segmented ion trap are presented in Chapters 5-7. More details of the trap hardware are given in Section 4.1.2.

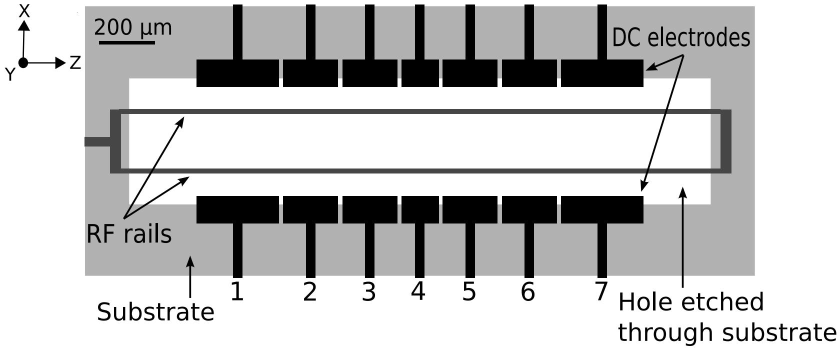

Figure 2.8: Schematics of the Sandia trap. Details are presented in Section 4.1.2.

As most of the simulation software tools were developed in detail with the Liverpool trap, applying the same analysis to a different trap design was relatively straightforward. The computational model of the trap was as in Figure 2.9 and Figure 2.10 shows a calculated electric field potential when the DC electrodes (as well as the ground plane) are grounded and the RF electrodes have a non-zero voltage applied to them.

By requiring the trapping frequencies to match the experimentally measured frequencies the voltage amplitude on the RF electrodes was calibrated in terms of RF input voltage, see Section 6.4. The trap was used for the ion shuttling experiments described in Section 7.3, so we are interested in the geometrical factors γ and μ for the Sandia trap. They are

$$\gamma \simeq 5 \times 10^{-5}, \tag{2.11}$$

$$\mu \simeq 0.02. \tag{2.12}$$

Compared to the Liverpool trap, γ is much smaller. This is because the DC electrodes are placed “behind” the RF electrodes from the ion’s point of view; as a result the RF electrodes “smooth” out the potential created by the DC electrodes, reducing its quartic and higher order terms. Thus the Sandia trap is less suited for ion pair splitting than the Liverpool trap.

As the results in Section 6.4 show, the trap parameters predicted by the calculation are largely consistent with those determined by the experiment. There are discrepancies, though, e.g. in the prediction of the axial trap frequency (see Figure 6.9). These discrepancies are most probably due to simplifications and inaccuracies in our representation of the trap, as follows.

On the lower side of the trap, the etched substrate surface is covered with gold (the "ground plane"), to eliminate charging of the dielectric material close to the trap. The position and angle of this surface, however, are not well determined due to the nature of the manufacturing process. Relatively minor issues include uncertainty in the size of the gaps between the adjacent electrodes, also the actual design of the RF rails is a complicated connecting ring structure, while in the simulation the RF rails were simplified to a pair of square rods with the appropriate dimensions.

To properly evaluate the effect of such misrepresentations of the geometry would require additional simulations. This becomes impractical because of the large number of parameters. In fact for most purposes the current model is adequate, as shown in Section 6.4. Experiments beyond the scope of this thesis, such as multiple ion shuttling, may require more detailed analysis.

2.5 Future traps

Ion traps are being developed with even larger numbers of electrodes and to model these would strain the capabilities of our current simulations software. CPO is able to calculate up to 6000 elementary segments or divisions of electrodes. The simulation of the Sandia trap already uses up to 5960 segments, and comparing results of the calculation with models of the same trap with smaller number of elementary segments shows that this number cannot be decreased without loss in precision. Thus, for subsequent ion traps, more powerful Laplace equation solving software needs to be used. One such program is under development at the University of Ulm [38].

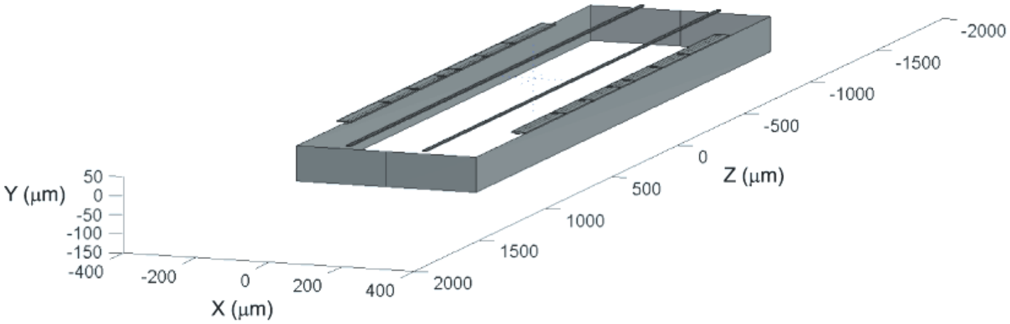

Figure 2.9: The 3D computational model of the Sandia trap, created in Matlab. The end section of the DC electrodes, the parallel portion of the RF rails and the ground plane on the side of the hole through the substrate is included (see Figure 2.8).

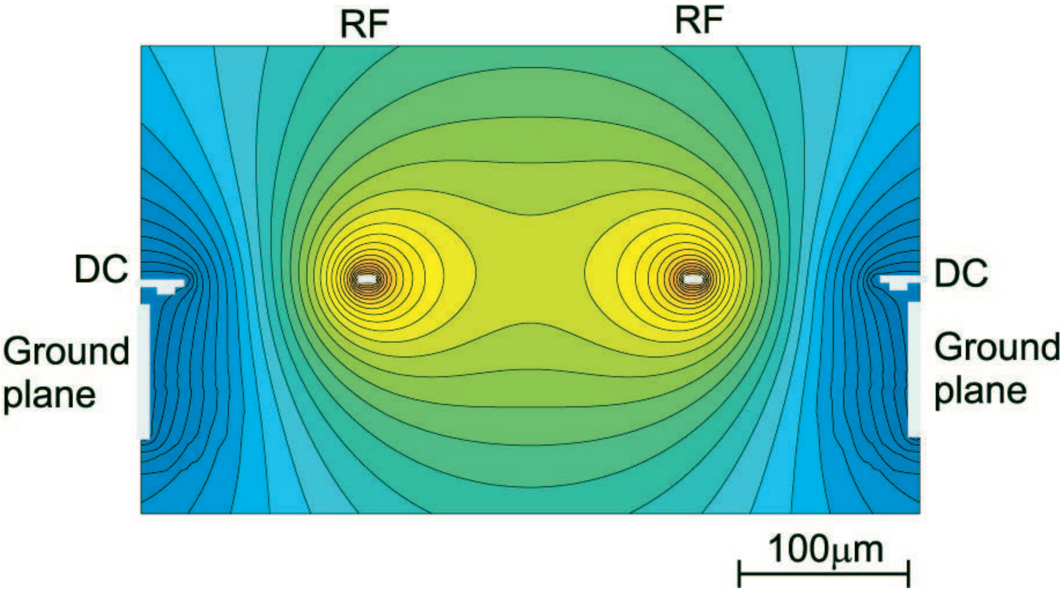

Figure 2.10: Electric field due to a fixed voltage on the RF electrodes. Cross section in the X-Y plane, as shown in Figure 2.8.

Chapter 3

Ion shuttling and loading theory

In this chapter we present theoretical treatments of two issues relevant to the use of multiple-trap architectures for quantum computing.

The first is the controlled transport or "shuttling" of ions among an array of traps. The method envisaged to achieve this is the application of suitably chosen waveforms to the DC electrodes of the trap array, so that the potential well holding one or more ions moves in a controlled way. For example, one might want to maintain a well at a given tightness while its centre accelerates, moves uniformly, then decelerates. The main target is to achieve fast shuttling while minimising "heating", that is, the injection of motional energy into the ions (for example owing to limited control of the waveforms or knowledge of the initial conditons).

The second issue is loading of ions into shallow traps. The longer term aim is to have arrays of thousands of tight traps positioned close together. This is a feasible concept but only if microfabrication methods are adopted. One problem is that physically smaller traps are much harder to load: they are either more shallow or have a smaller trapping volume, or (usually) both. For this reason it becomes of interest to investigate the loading process itself. In our experiments we photoionise atoms from an atomic beam [41]. The sorts of questions that we would like to answer are, what is the trap depth? Where is the best place to focus the ionisation beams? What proportion of atoms from a given thermal distribution will enter stable orbits when they are ionised? In this chapter we present numerical calculations providing some specific information for one of our traps, and some general insights into the issues that arise.

3.1 Precise shuttling

Physically moving ions to transport quantum information inside ion trap quantum computers is a promising method to allow ion trap methods to be extended to a practical computer. In highly segmented large scale ion traps, the ions are stored in different trapping regions. Quantum gate operations are performed on a small number (e.g. a pair) of ions, and some of these ions are then shuttled to a different trapping region to interact with other ions.

For practical quantum computation a large number of ions and quantum gates must be used; thus it is likely that a significant portion of the quantum computer's operation time will be devoted to ion shuttling. It is desirable to devise control schemes to transport ions reliably, quickly and with minimal motional heating.

Reliability is important, since loss of ions (qubits) during transfer introduces errors to the algorithms being performed. High speed is desirable to keep the operation time minimal. Reduced motional heating eases requirements on cooling of ions after transport and potentially result in a simpler experimental arrangement.

In the simplest 1D description of ion shuttling, the motion of the ion can be described by a moving harmonic well as

$$a(t) = -\omega^2(x(t) - x_0(t)) \tag{3.1}$$

where $x(t)$ is the ion's position, $a(t) = \ddot{x}(t)$ is the ion's acceleration, $x_0(t)$ is the position of the well, and ω is the trap frequency. Heating is considered to be the excess motional energy of the ion, compared to its starting energy.

In previous theoretical studies [42, 43] and experimental realizations [44, 37], the focus was mainly on choosing $x_0(t)$, and then describing the resulting motion of the ion $x(t)$, including residual motional energy after the shuttle.

Example trap motions include sinusoidal [42]:

$$x_0(t) \sim \sin(t\pi/2t_0) \text{ for } -t_0 \leq t \leq t_0 \tag{3.2}$$

error function [42]:

$$x_0(t) \sim \mathrm{Erf}(2t/t_p)/\mathrm{Erf}(2t_0/t_p) \text{ for } -t_0 \leq t \leq t_0 \tag{3.3}$$

and hyperbolic function [43]:

$$x_0(t) = \frac{x_{tot}}{2} \frac{\tanh\left(N\frac{2t-T}{T}\right) + \tanh(N)}{\tanh(N)} \text{ for } 0 \leq t \leq T \tag{3.4}$$

In the limit $t \gg \omega^{-1}$ the differences in the residual heating for different choices of $x_0(t)$ tend to vanish. For short operation times (t in the order of few oscillation cycles), residual heating is very dependent on the choice of $x_0(t)$.

An alternative approach is presented in this section. Instead of searching for the ideal $x_0(t)$ through a library of functions, it can be derived directly from the desired ion motion. The requirement for no motional heating is that the final velocity $v(\tau) = 0$ and $x(\tau) = x_0(\tau)$ (where τ is the total ion transport time). Combined with the assumption that the ion starts stationary (i.e. cooled down to a low motional state), the constraints for the ion's velocity and acceleration are:

$$v(0) = 0, \tag{3.5}$$

$$\dot{v}(0) = a(0) = 0, \tag{3.6}$$

$$v(\tau) = 0, \tag{3.7}$$

$$\dot{v}(\tau) = a(\tau) = 0. \tag{3.8}$$

Any function that fulfils these constraints and is differentiable can be used as a design-function for the ion shuttle. Once a general form of $v(t)$ is chosen, the ion's position and acceleration is calculated:

$$\int_0^t v(t')dt' = x(t), \tag{3.9}$$

$$\dot{v}(t) = a(t). \tag{3.10}$$

and equation 3.1 can be rearranged to express the position of the potential well as a function of time:

$$x_0(t) = \frac{a(t)}{\omega^2} + x(t) = \frac{\dot{v}(t)}{\omega^2} + \int_0^t v(t')dt' \tag{3.11}$$

Thus, if the potential well is moved following $x_0(t)$, the ion will take the defined velocity function $v(t)$.

The total transport distance is

$$x_{tot} = \int_0^\tau v(t')dt' \tag{3.12}$$

which allows for easy scaling of the shuttle distance with the same general form of the velocity design function.

Equation 3.11 contains a static expression for the trap frequency ω. We can instead include a position dependence $\omega = \omega\left(x_0(t)\right)$. This complicates the calculation of $x_0(t)$, but does not prevent a solution.

The effect of an initial non-zero motional energy depends on whether or not ω varies during the shuttle. For fixed ω the final motional energy will be equal to the starting energy because of the nature of the simple harmonic motion. In case of varying ω, the uniformity of the simple harmonic motion is broken, and the ion's initial motional energy has a similar effect to timing-imprecisions of the control of the potential, resulting in heating. An oscillation in ω can cause parametric heating.

As a simple example, one can choose a sinusoid voltage design function (as shown in Figure 3.1)

$$v(t) = \frac{x_{tot}}{\tau}\left(1 - \cos\left(\frac{2\pi t}{\tau}\right)\right) \tag{3.13}$$

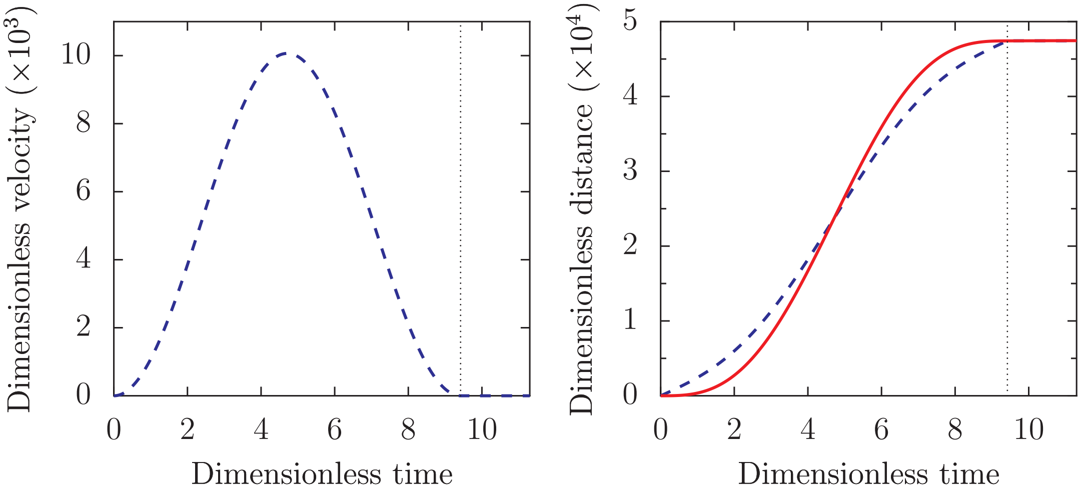

Figure 3.1: (Left) Desired ion velocity and (Right) corresponding ion position (solid line) and well position (dashed line) as functions of time, in scaled units. The vertical line denotes the end of the shuttle sequence. The shuttle distance is one electrode separation away from the trap centre (752.5 μm). The time is expressed in units of ω^{-1}, the distance in units of $\sqrt{\hbar/m\omega}$ and the velocity in units of $v_0 = \sqrt{\hbar\omega/m}$.

where x_{tot} is the total transport distance. Then the ion's position and acceleration are

$$x(t) = \frac{x_{tot}t}{\tau} - \frac{x_{tot}}{2\pi}\sin\left(\frac{2\pi t}{\tau}\right) \tag{3.14}$$

$$a(t) = \frac{2\pi x_{tot}}{\tau^2}\sin\left(\frac{2\pi t}{\tau}\right) \tag{3.15}$$

and the position of the potential well, in the case of constant trap frequency, is

$$x_0(t) = x_{tot}\left\{\frac{t}{\tau} + \frac{4\pi^2 - \omega^2\tau^2}{2\pi\omega^2\tau^2}\sin\left(\frac{2\pi t}{\tau}\right)\right\}. \tag{3.16}$$

Once $x_0(t)$ is available, it has to be turned into practical voltage sequences to control the ion trap electrodes. This can be done either by numerically simulating the ion trap's behaviour (as illustrated in the previous chapter), or by experimentally mapping control voltages onto trapping positions and frequencies. Figure 3.2 shows a voltage control sequence to shuttle an ion from the centre of the Liverpool trap through one electrode distance (0.7525 mm), corresponding to the potential well control of Figure 3.1. Voltages on only two electrodes are shown; the other 5 electrodes are kept at a constant voltage.

It is important to estimate the effect of control parameter imperfections on the outcome

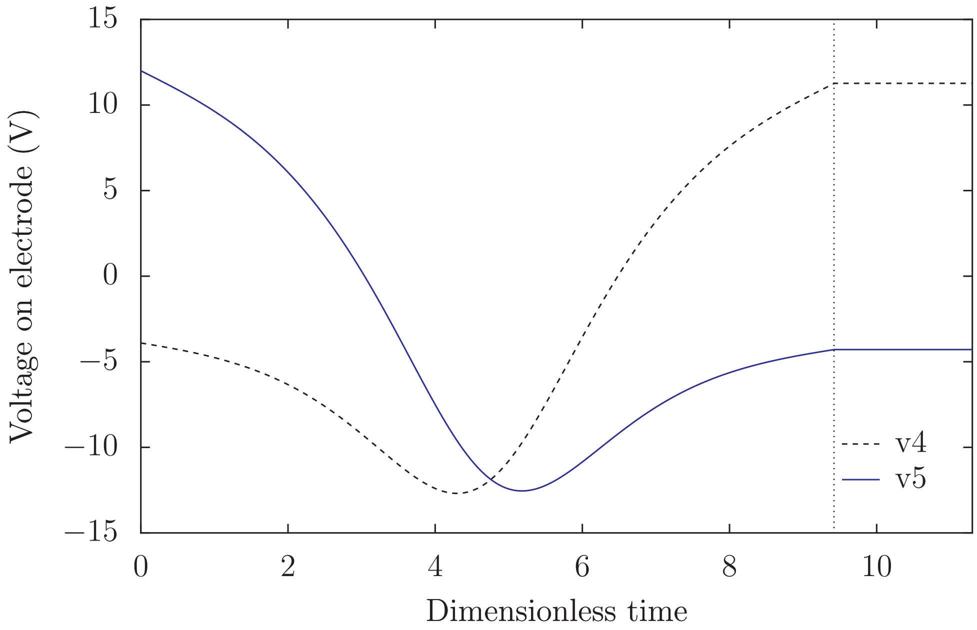

Figure 3.2: Example shuttle voltage sequence in the Liverpool trap. The ion is moved by one electrode distance (0.755 mm) from in front of electrode #4 to #5, using the shuttle sequence shown in Figure 3.1. Voltages on electrode #4 and #5 are shown, while all other electrodes are kept at 12 V. The trap frequency is kept at $\omega/2\pi = 1\,\text{MHz}$. A vertical line denotes the end of the shuttle sequence.

of the shuttle. There are a large number of error models and testing for all of them would not be practical. We present a calculation in case of a simple error model that can arise in experimental situations: imperfect setting of control voltages. In our calculation we assumed that compared to the voltages presented in Figure 3.2, the voltage of the centre electrode (v4) is changed by a fixed multiplier. Multipliers of $\{0.90, 0.95, 0.99\}$ are used. The change in trap frequency was 2.6%-0.1% along the shuttle path in case of the 0.9 multiplier, and smaller for the other multipliers.

Figure 3.3 shows the ion's excess motional energy, as a function of shuttle time. The results show that even when the control voltage is 10% different from the expected voltage, the ion can be shuttled by one electrode separation distance (752.5 μm) in $t = 12/(\omega/2\pi) = 12\,\mu$s while gaining only a single motional quantum.

From an experimental point of view, however, fast changes in the voltages might pose challenges to the control electronics. The shuttling DC control voltages such as the one in Figure 3.2 have complicated time dependence and must be generated with good timing and precision. Also, in most of the ion trap designs the voltage supply lines of the DC

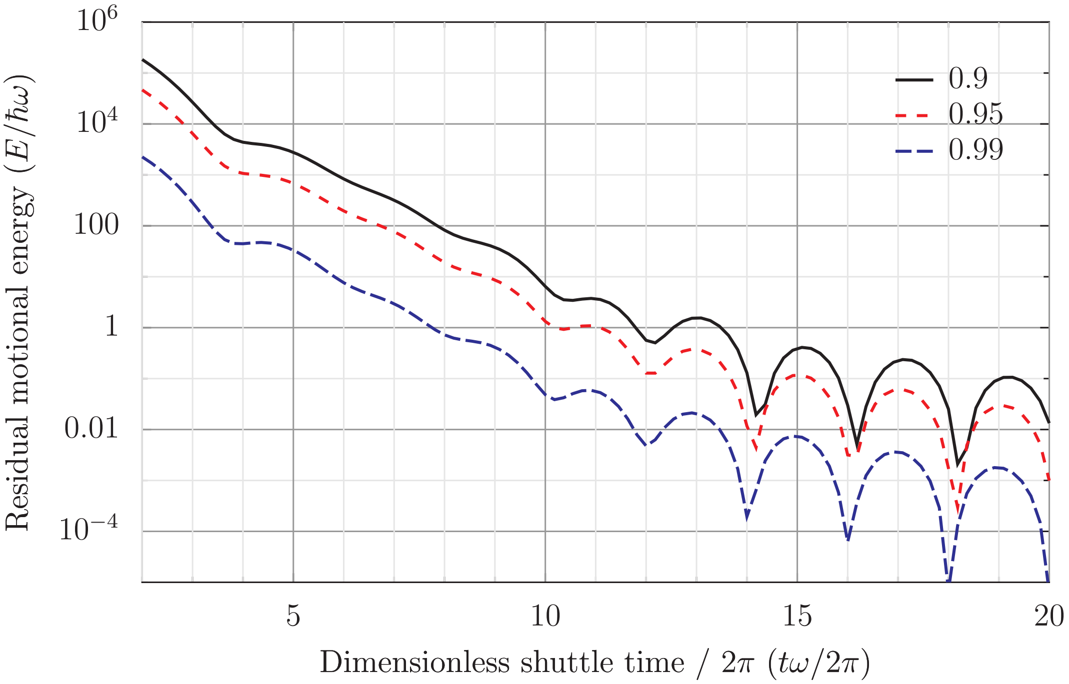

Figure 3.3: Excess heating as a function of total shuttle time, for different changes in control voltages compared to the expected voltages. Multipliers $\{0.90, 0.95, 0.99\}$ mean $\{10\%, 5\%, 1\%\}$ lower voltages than expected control voltage (see text). The ion is shuttled to one electrode distance, that is $x/\sqrt{\hbar/mw} = 4.7 \times 10^4$ in dimensionless units.

electrodes have low-pass filters installed to reduce noise and heating of the ion. These filters will change the waveforms, and introduce Johnson noise heating into the ion transport. In this situation one should analyse the effect of the filters on the waveforms and change the input voltage control sequence to achieve the desired output after the filters. If this is not possible, then one has to perform slower ion shuttling. The filters may also be advantageous in case of using Digital-to-Analog converters to create the control voltages: the digitization effects can be blurred out by the filters, resulting in a better voltage sequence on the electrodes.

This method is also applicable to separating and joining ions. In the calculations the Coulomb interaction of the ions can be taken into account as a short distance perturbation of the trapping potential. Figure 3.4 shows a voltage sequence and two ion trajectories in the case of separating two ions. To join them together requires simply the time-reversal of the applied voltages.

Extending this approach to 2D movements, such as around a corner at a junction (as

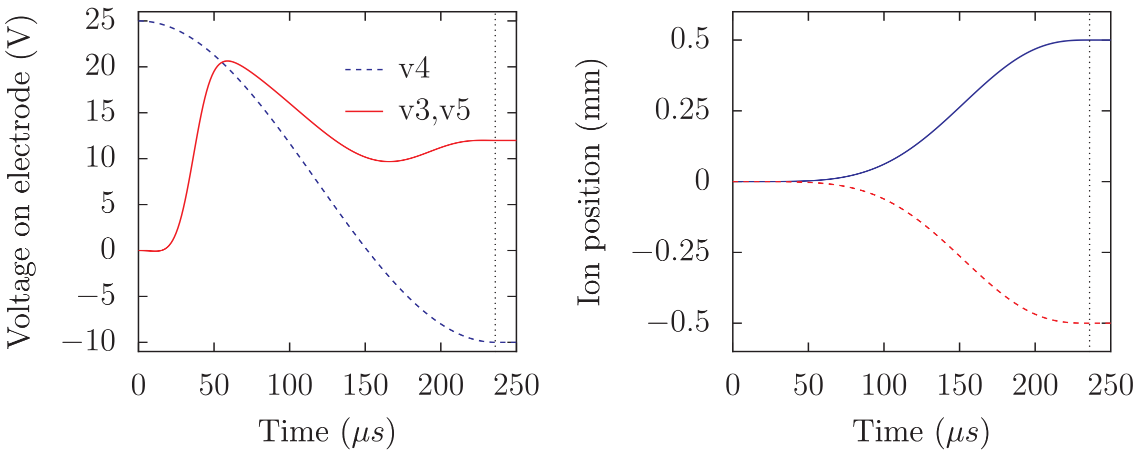

Figure 3.4: (Left) Voltage sequence to perform ion separation. The voltage on electrode #4 and those on #3,#5 (the same) are shown, all other electrodes are at 25 V. (Right) simulated ion trajectories during separation. The vertical dotted line marks the end of the shuttling sequence. The time scale is longer than on the previous plots, to provide a voltage control sequence that may be be experimentally produced (due to the limit on the rate of change of DC control voltage). The calculation can be carried out in a similar manner for faster separation. The maximum separation was 1 mm. The electrode-electrode distance is 0.7525 mm.

in [37]), and the analysis of imperfections of timing and trap frequency require additional theoretical work and will be the subject of a later study.

3.2 Ion loading simulation in Sandia trap

After observing neutral Ca fluorescence in the Sandia trap, trapping of ions was attempted. However, for a period of time, this was not successful. While exploring different experimental control parameters (photoionisation laser powers, Doppler-cooling laser powers and detunings, Ca oven currents, etc.), the electrical parameters of the trap could not of course be measured directly. Before trapping ions, one has only limited means of evaluating what voltages are actually on the electrodes. In the case of the DC electrodes the uncertainty was mainly whether the applied voltage reaches the electrode, or there is an electrical break along the way. In the case of the RF electrodes the situation is more subtle. The drive voltage was amplified by a helical resonator (see Section 4.6.3). The amplification (Q-value) was estimated, but losses could occur on the electrical connections bridging the outer and inner side of the vacuum can. Thus we had an upper estimate of voltages ($\sim 100\,\mathrm{V}$), and the actual RF amplitude could have taken any value up to this.

To evaluate the effect of different RF amplitudes on the ion loading rate, a numerical study was conducted. The electric field was modelled in the Sandia trap, as described in the previous chapter. The resulting potentials were then used to generate an oscillating electric field. An ion was randomly placed in the area near the the trap centre, where the photoionisation and Doppler-cooling laser beams were focused (with radii $\sim 20\,\mu\mathrm{m}$). The random placement represented the ionization happening at that particular position, and the ion suddenly starting to interact with the RF field. The subsequent behaviour of the ion was found by solving the classical equation of motion. Table 3.1 lists the initial parameters. The ion's movement was followed for a number of RF cycles, to evaluate whether it had a trapped orbit or leaves the trap. Doppler cooling was not included in the simulation, since it is too slow to affect the results. If the RF field on its own would not trap the ion, the cooling would not in general prevent it from escaping.

Parameter	**Values**
Starting position	Random in area, $r < 20\,\mu\mathrm{m}$
Starting velocity	Random, 0-700 K(100 Ksteps)
Direction of velocity	Set, 45°to trap electrode plane
RF phase	Random
RF amplitude V_{rf}	25,40,50,60,75,100 V

Table 3.1: Ion loading simulation parameters

Figure 3.5 shows two sample ion trajectories. The trap electrodes lie in the X-Z plane and the RF electrodes are at $x = \pm 100\,\mu\mathrm{m}$. The direction of the initial velocity of the ion was set by the respective positions of the Ca oven and the trap (see Figure 5.6), that is, at 45°, from the bottom-left to the top-right in Figure 3.5.

Figure 3.6 summarizes the overall capture probabilities as a function of ion temperatures (starting velocities), for different RF amplitudes. For RF amplitudes $V_{\mathrm{rf}} < 50\,\mathrm{V}$ the capture probability of high temperature ions is significantly reduced. Since the Ca oven was expected to operate at temperatures $\sim 600\,\mathrm{K}$, a large fraction of the ions is expected to have even larger velocities than those considered in the simulation. Thus the requirement for successful trapping in the Sandia trap appears to be $V_{\mathrm{rf}} > 50\,\mathrm{V}$.

Figure 3.7 shows an additional detail of the simulated ion loading. The capture probabilities are plotted as functions of distance from the trap centre for different ion temperatures. That is $P(r) =$ the proportion of ions created withing a disc of radius r that are captured. The RF amplitude was set to $V_{\mathrm{rf}} = 50\,\mathrm{V}$, the lower limit of practical trapping. It appears that lower temperature ions are more likely to be captured in the inner regions of the trapping area, while the high temperature ions are captured in the outer regions. Figure 3.8 shows the initial positions of successfully trapped ions for $V_{\mathrm{rf}} = 50\,\mathrm{V}$ and $T = 500\,\mathrm{K}$. It appears that there is virtually no capture of ions which cross the trap centre. On the two sides of this central band ions are captured when the phase of the RF field is such that it deflects the ions towards the trap centre, and eventually they end up in a stable orbit. Correspondingly, the initial RF phase for the ions captured in the two areas are opposite to each other.

Once ion loading was successful in the Sandia trap, and experiments were carried out to test the trap frequencies (see in Section 6.4), it was possible to relate the RF input voltages to the RF amplitude on the electrodes. It was found that the trap operation was in the $63\,\mathrm{V} < V_{\mathrm{rf}} < 105\,\mathrm{V}$ region. This suggests that the difficulty of ion loading was due to other factors, while the electrical properties of the Sandia trap were adequate (see Section 6.1).

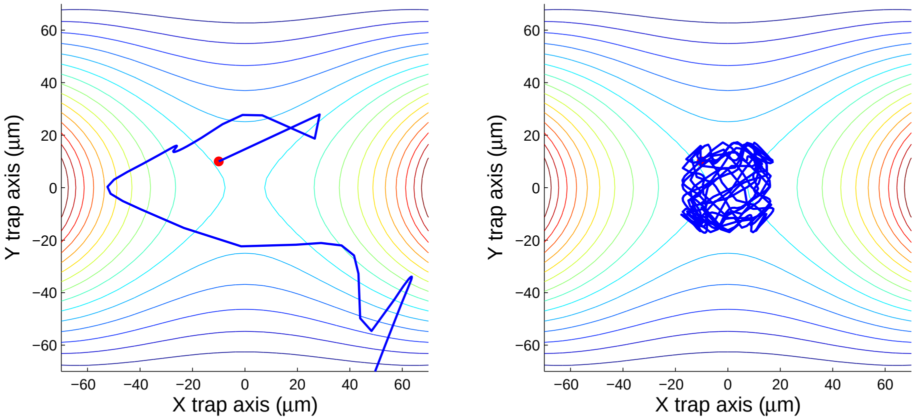

Figure 3.5: Examples of simulated ion motion inside the trap. The trap electrodes lie in the X-Z plane; the static field lines are plotted for reference. The ion's initial position is indicated by a dot at the beginning of the trace, with velocity in the top-right direction. Both traces start at the same position and velocity, but at different points in the RF cycle (they have $\pi/2$ different phase). $V_{\mathrm{rf}} = 100\,\mathrm{V}$, $T_{ion} = 700\,\mathrm{K}$. The equation of the motion was solved with a variable step size Runge-Kutta method.

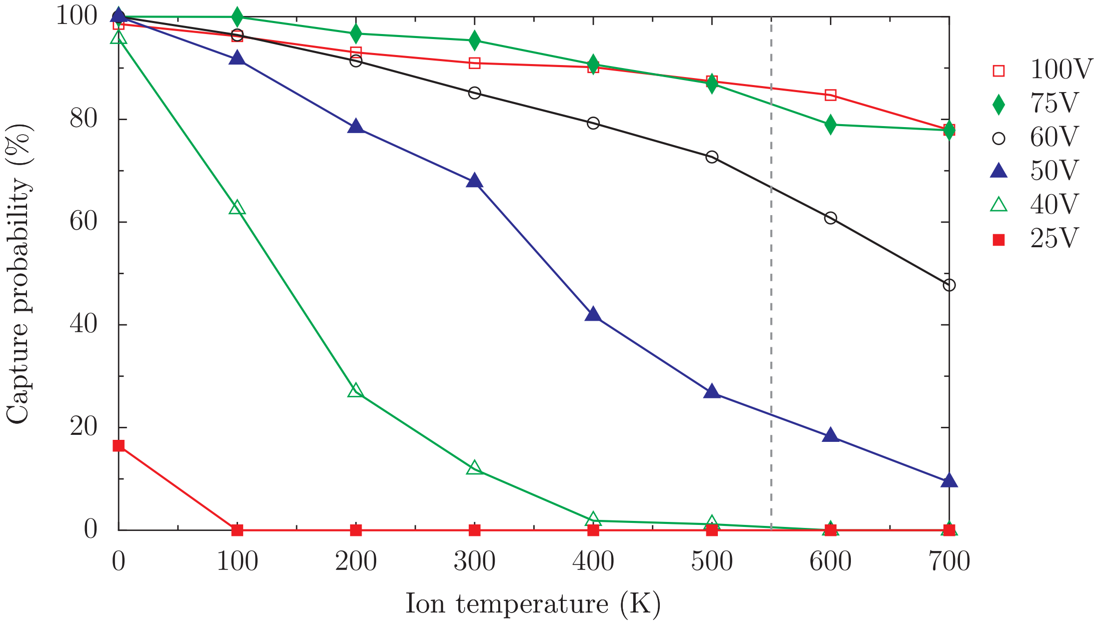

Figure 3.6: Summary of the simulated overall capture probabilities within a 20 μm radius of the trap centre, as a function of ion temperature and RF amplitudes. Each point represents a single value of the initial ion speed v and 'ion temperature' is mv^2/k_{B}. The dashed line shows the nominal Ca oven temperature. Each data point is based on 700-3000 simulated ionisation events.

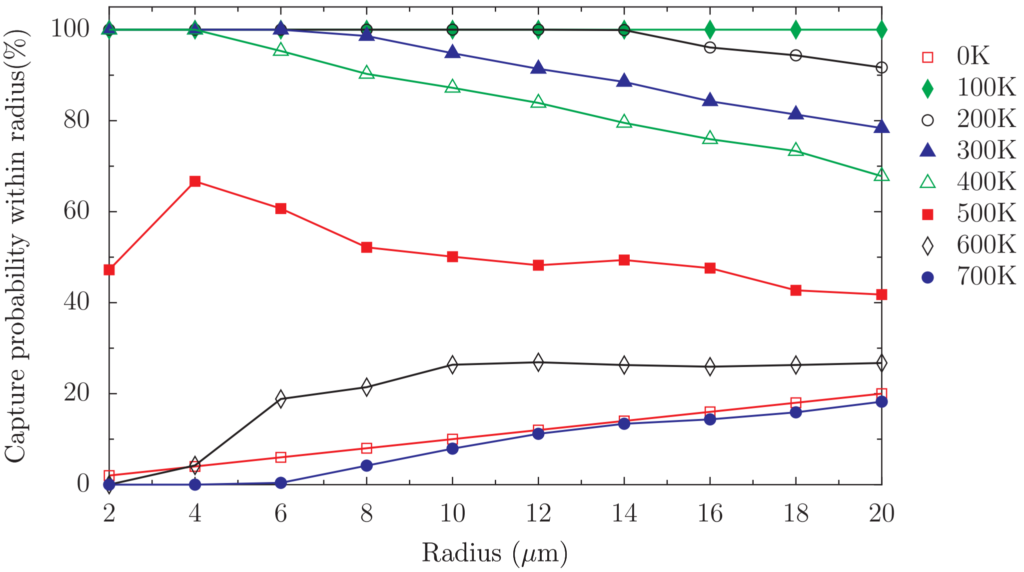

Figure 3.7: Proportion of ions P(r), captured with ionisation position within radius r from the trap centre, for a number of ion temperatures. The RF amplitude is set to $V_{\mathrm{rf}} = 50\,\mathrm{V}$. Cold ions are more likely to be captured in the trap centre, while hot ions are more likely to be captured in the outer regions. The average density of simulated ionisation positions was 2.5 ion/ μm^2 within the maximum 20 μm radius.

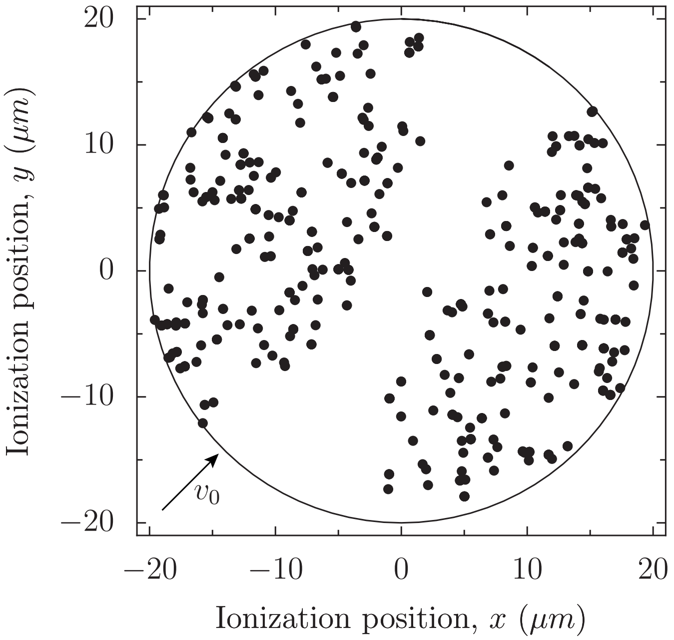

Figure 3.8: A number of simulated ionization positions of successfully captured ions in the case of $V_{\mathrm{rf}} = 50\,\mathrm{V}$ and $T_{ion} = 500\,\mathrm{K}$. The ions' initial positions are randomly distributed in area within the 20 μm radius shown. The direction of the ions' initial velocities is indicated by an arrow. The captured ions in the top left and the bottom right quadrant require opposite initial RF phase to be captured.

Chapter 4

Apparatus

This chapter introduces the experimental setup. First the vacuum system will be described, then the laser system, optical setup, the detection system and the experimental and control electronics.

The complete apparatus was built from scratch. It was designed to address requirements different from those of our research group's previous ion trap experiments. The new apparatus was intended to test a number of different ion trap designs, which involves the replacement of the ion trap (or the whole vacuum system) more frequently. To make this replacement easier, a modular design philosophy was adopted.

Single-mode optical fibres were used to transport light from the lasers to the optics in the immediate vicinity of the trap. This decouples the optical alignment at the input and output side of the fibre. Changes in the alignment that occur in these optical setups, such as creeping with changing temperature or accidental movement of optical elements, cannot propagate through the whole system. If there is a change in alignment on the fibre input side, it results in loss of power on the output side, not misalignment. This provides greater stability and easier maintenance.

The vacuum system was standardised. The same type of vacuum chamber was used with two new ion traps. This makes the preparation of the system easier, and several devices in the apparatus (most importantly the whole optical detection system) are reusable for a range of different ion traps in the future.

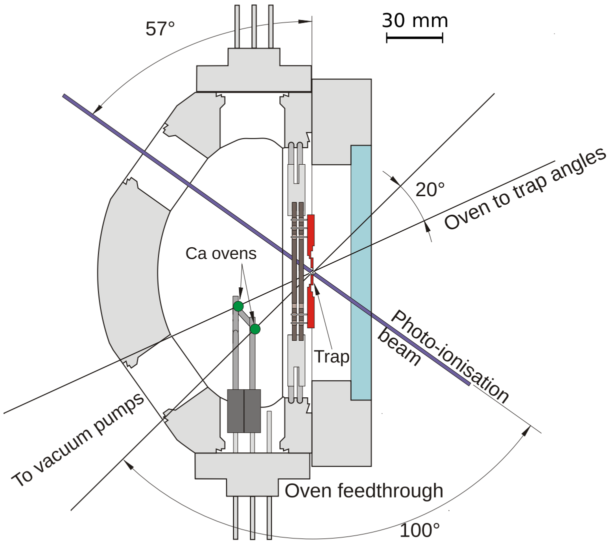

Figure 4.1: Vacuum chamber cross section, showing the position of the trap, main detection window, Ca ovens and direction of the photoionisation beam. (Colour in electronic version)

4.1 Vacuum system

4.1.1 Vacuum chamber

A hemispherical vacuum chamber, manufactured by Kimball Physics, was adopted (see Figure 4.1). Its small size makes it easier to lift it out of the optical system and place it in a bake-out oven. It has good optical access through a number of viewports. The main viewport has 4.5 inch (114 mm) diameter. There are two additional viewports of 2.5 inch (64 mm) on the side of the chamber and a 1.33 inch (34 mm) viewport on the top. Another 1.33 inch opening on the bottom of the chamber was used for attaching vacuum pumps and a gauge, as well as for routing some of the electrical wiring.

4.1.2 Sandia trap

The experiments described in subsequent chapters were conducted using a DTO Module 4 ion trap (referred to in the following as the "Sandia trap") provided by Sandia National Laboratories in Albuquerque, New Mexico, USA. It has a planar electrode arrangement on a chip carrier (Figure 4.2). 14 DC control electrodes are arranged around a $2000\,\mu\text{m} \times 400\,\mu\text{m}$ slot cut into the carrier. Along the slot, there are 2 RF rails, approx. $10\,\mu\text{m}$ wide and $200\,\mu\text{m}$ apart. The trapping axis is along the slot, in between the RF rails.

The trapping region is centred on a 8 mm × 8 mm high resistivity silicon (HRS) substrate, which has a 1 μm thick top layer of silicon-oxy-nitrate ($\mathrm{SiO}_x\mathrm{N}_y$). Both the DC and the RF electrodes are made of tungsten with a complex ring structure, to withstand stress from high electrostatic forces. The DC electrodes have a 0.5 μm thick aluminium covering layer, but this layer does not extend right to the edge nearest the trapping region, stopping 10 μm short. The RF rails are connected to their bonding pads via an air bridge, suspended over the substrate. The chip is mounted on a Kryocera pin grid array package. The bottom of the package has a counter-sunk slot for better optical access to the trapping region. The open substrate surface close to the trap and the bottom of the electrodes are gold coated. The coating on the substrate surface reduces charge build-up, which would lead to stray electric fields. On the front face the electrodes have an aluminium coating, while the substrate is bare silica. Newer versions of the same trap design, used by other research groups, have gold coating on the front face of the substrate as well.

In the original design of the Sandia trap the RF rails were driven from both ends, to minimise the variation of the RF field along the trap axis. In early testing, however, it was discovered that this arrangement was problematic. When driven from both ends, a small difference in the RF phase at the two ends is hard to avoid. It results in currents flowing in the RF electrodes, and thus ohmic heating. The NIST Ion Trap Group observed heating resulting in a visible white glow of the RF rails, and their subsequent mechanical failure, when driven from both ends.

To eliminate such heating in our trap, the air bridge connection was removed on one side, so that the RF rails are driven from a single voltage source. The air bridge was severed as close to the trap as possible. This is to reduce the excess capacitance between the remains of the removed RF supply line and the front face of the chip (see Figure 4.2).

Due to the planar arrangement of the Sandia trap, one has less control over the electric field perpendicular to the trap plane, compared to the in-plane field. An extra electrode wire was therefore attached to the bottom of the chip carrier (a "compensation electrode"). The electrode is a segment of 0.25mm diameter gold wire connecting two pins on the back of the chip socket. In the middle, the wire was twisted into a spike pointing towards the trapping region. It is connected to the unused pin and the common ground of the Ca oven

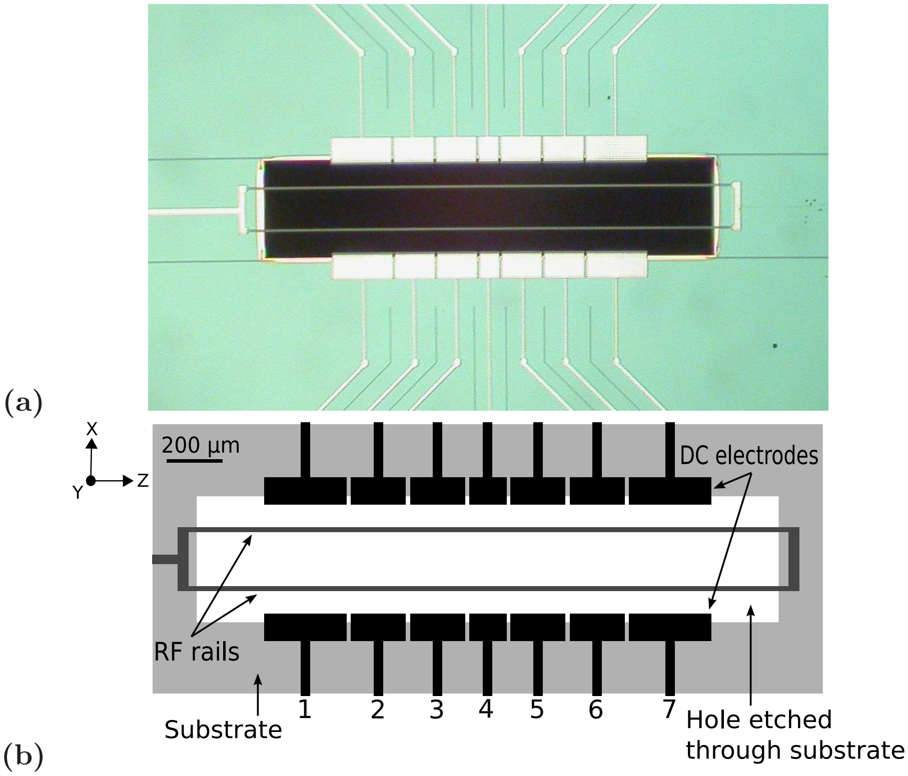

Figure 4.2: a) Photo of the Sandia trap, after removal of the air bridge on the right side, taken with a digital camera through the eyepiece of an optical microscope. b) Schematics of the trap, with the numbering of the electrode pairs (one upper and one lower electrode) for reference. The trapping region is along a line following the middle of the trap, in between the RF rails.

feedthrough (see Figure 4.3). The details of the air bridge removal and the compensation electrode are given in [45].

Commercially available chip sockets were incompatible with our UHV requirements. They had high outgassing rates and could not withstand the 200°C temperature that was used in the bake-out of the vacuum system. Custom chip sockets were made, based on a design by the University of Michigan, to mount the Sandia trap, using Vespel, a high performance plastic suitable for UHV operation.

4.1.3 Calcium oven

For a source of calcium, two calcium ovens were installed in the vacuum chamber. Each oven is a thin-walled stainless steel tube with 14 mm length and 3 mm diameter. Calcium was placed in the tubes by cutting narrow strips from a calcium foil using a clean steel

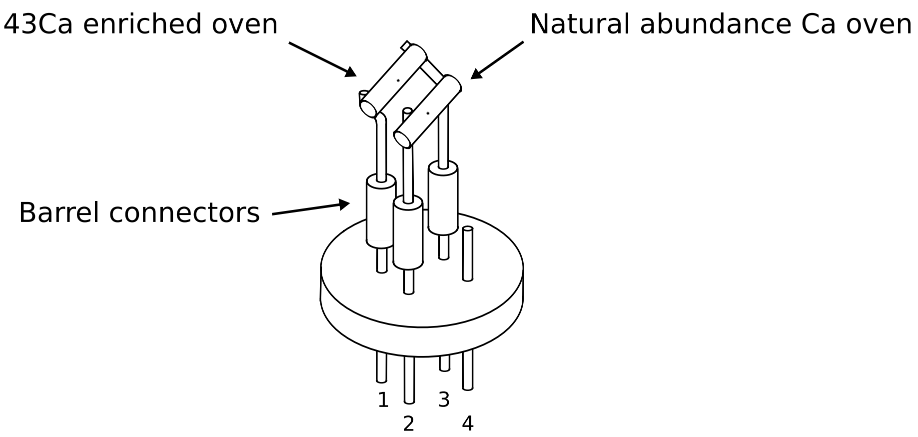

Figure 4.3: Schematic view of the feedthrough connected to the Ca ovens. Of the four numbered pins of the feedthrough, (1) is connected to the ^{43}Ca enriched oven, (2) is connected to the natural abundance Ca oven, (3) is the common return and (4) is connected to the manually added compensation electrode (see Section 4.1.2, connection not shown on the figure). Figure based on CAD design of M. Curtis.

knife, and dropping them into the tubes. One oven contained calcium with its natural isotopic abundance and the other contained a sample enriched in ^{43}Ca. The ends of the tubes were closed by crimping. The oven orifice is a small hole of area 0.3 mm^2 drilled in the middle of the tube. The ovens were spot-welded on stainless steel rods (see Figure 4.3) such that they have one rod each as current input connection and a third rod is their common return. Resistive heating was used to operate the ovens, by passing current (up to 7 A) through them. The feedthroughs and thick steel rods have negligible resistance compared to the thin-walled ovens. See Section 5.1 for further information about the ovens.

4.1.4 Vacuum pumps

For continuous ultra-high vacuum (UHV) operation of the trap, there are two vacuum pumps attached to the chamber.

The main pump is a Varian VacIon Plus 20 ion pump, which is aided by a SAES SORB-AC GP50 chemical getter pump. The chemical getter pump's role is similar to a titanium sublimation pump: it has higher efficiency in pumping hydrogen, which supplements the capabilities of the ion pump. The chemical getter does not require an external power supply once it has been activated. It is advantageous in vacuum systems which are opened up to air very rarely since its sponge-like structure absorbs gases very quickly and it can be outgassed only very slowly, and in systems where having a hot filament (as in the titanium sublimation pump) is not feasible. In our system, however, the pump is well separated from the main vacuum chamber, so having a hot filament is not a problem, and opening up the vacuum to carry out repairs and changes of equipment is not uncommon. In future the chemical getter pump is therefore likely to be replaced with a titanium sublimation pump.

The pressure is measured on a Varian UHV-24 ion gauge, with reliable pressure measurements down to 5×10^{-11} Torr and reduced performance down to 5×10^{-12} Torr.

4.2 Optical setup

To trap and cool ions, four laser frequencies are needed. These are: 423 nm and 389 nm light for neutral atom excitation and photoionisation respectively, 397 nm and 866 nm light for Doppler cooling and repumping (see Figure 1.1). Additionally a 854 nm laser was set up later in the experiment, to prevent shelving in the 3d $^2D_{5/2}$ level.

The two photoionisation lasers were shared between different experiments. Beams were brought to the trap via an optical fibre from another laboratory room. The optical setup at the fibre input end is described in section 4.3.1.

The other three lasers were placed on a separate optical table from the vacuum system. Their layout was designed to fit the available space. A modular approach was adopted, meaning that the basic layout is common for all the systems, while it still allows for differences arising from the different requirements posed on the lasers. This makes possible relatively quick deployment of an additional laser system if needed.

In the common part of the design the laser beam goes through an optical isolator and is reflected from a diffraction grating. The grating's role is to create three separate beams (using orders -1, 0 and +1), and act as a coarse filter to clean up the spectrum. Order -1 is used for the "experimental beam", eventually coupling into a fibre which is connected to the trap optical setup. This order is arranged to have the highest power. Orders 0 and +1 respectively are used to lock the laser frequency to an external cavity and for frequency diagnostics.

Our lasers are of the Toptica DL100 series, with various laser diodes. Inside the laser's casing, the system is arranged in Littrow configuration, in which a grating provides optical feedback to the laser diode. This results in stable single-mode operation and narrower linewidth.

The following sections provide details of the individual laser systems.

4.2.1 866nm repumping laser setup

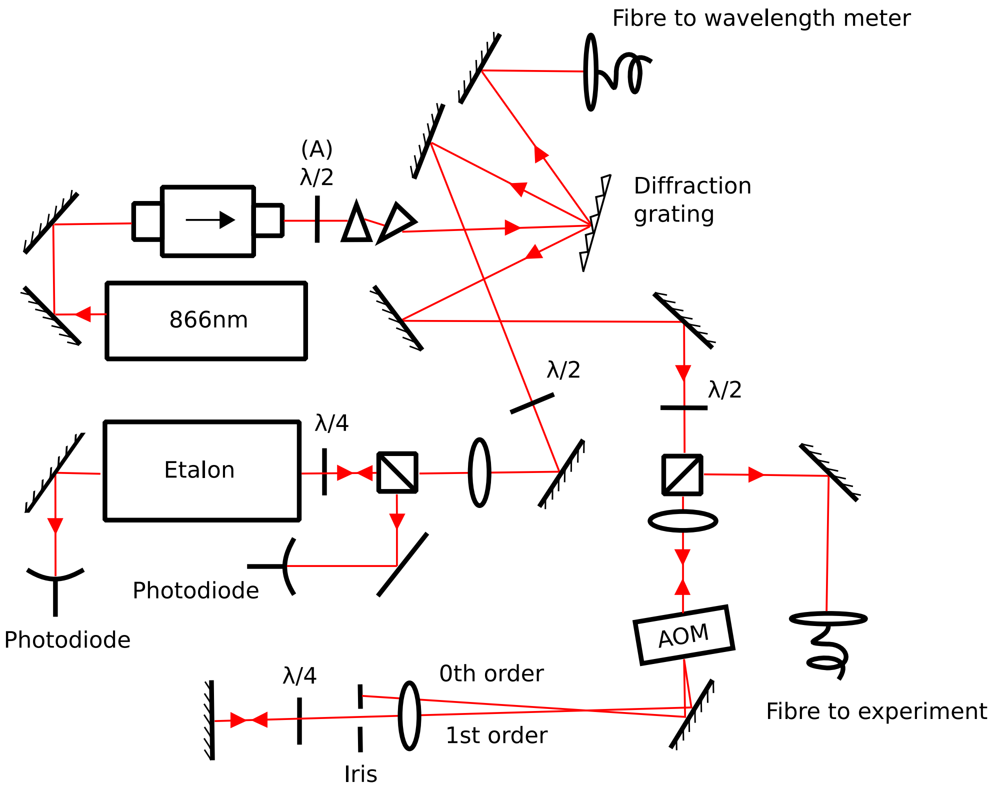

Figure 4.4: Layout of the 866nm laser system. Details in the text. Arrows on the beam-paths show the direction of beam propagation. (Colour in electronic version)

The main requirement of the 866 nm laser is high output power, at least of the order of 1 mW at the ion. The optical layout is shown in Figure 4.4.

The output of the laser box is guided through an optical isolator to reduce optical feedback. A $\lambda/2$ waveplate (A) sets the optimal polarisation for an anamorphic prism pair, which is used for beam shaping. Beam shaping is necessary to create a more circular beam as the diode laser output is generally highly elliptical (see Figure 4.5). The prism

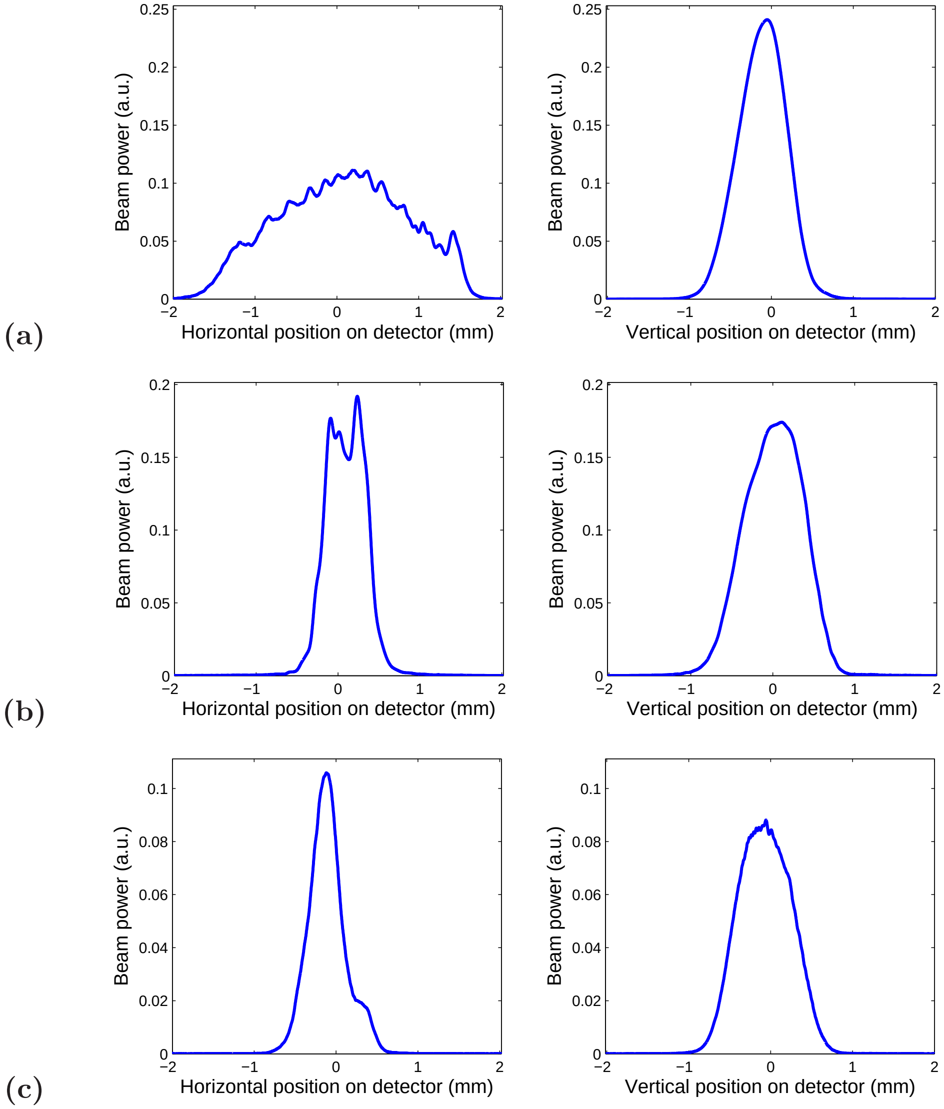

Figure 4.5: Beam profiles of the 866nm laser, at different points in the optical path (obtained with Thorlabs BP104-UV beam profiler). a) the laser output, b) after an anamorphic prism pair, c) the "experimental beam" before its fibre input. Laser intensities are in arbitrary units. The laser output is elongated horizontally, a disparity which is reduced by the prism pair. The "wiggles" visible on the top left and middle left profiles are generally caused by Fresnel diffraction, because of optical cut off at the focusing lens on the laser diode.

pair greatly improves the performance of the later optical elements, especially the coupling efficiency into fibres.

It is also possible to rotate the $\lambda/2$ waveplate (A), in order to change the proportions of laser power of the beams after the diffraction grating. Thus, if needed, more power can be diverted into the locking circuit and to the wavelength measurement, at the expense of power going to the experiment.

A Newport 53-004ZD02-035R diffraction grating (gold coating, 830 grooves/mm, blaze wavelength of 900nm) was used to divide the beam into three beam paths as explained above. Order +1 (the topmost reflected beam in Figure 4.4) is coupled into a multimode fibre, which leads to the wavemeter for frequency measurements. This grating performs a significant “cleaning up” role on the spectral composition of the experimental beam, eliminating wide wings (up to several nm) associated with amplified spontaneous emission in the laser diode.

Frequency stabilisation of the 866nm laser

Order 0 is used for frequency stabilisation with an external cavity. In the beampath a $\lambda/2$ waveplate sets the polarisation to maximise the transmission of a polarising beam splitter (PBS) cube, and a 250mm focal length lens focuses the beam to the centre of the NPL reference cavity. At this point of the layout, given the available equipment, we had two possibilities for stabilising the laser frequency: side-of-fringe lock or Pound-Drever-Hall (PDH) locking.

The former is much simpler to implement. One uses a photodiode to monitor the cavity transmission and locks to the side slope of the transmission profile. With the PDH method one monitors the cavity reflection with a high speed photodiode when the laser frequency is modulated. The photodiode output is demodulated and provide the error signal. This arrangement gives better frequency stability than side of fringe locking, with improved capture range (twice the modulation frequency of the laser). A detailed description is given in Chapter 5 of the PhD thesis of B. Keitch [46] and in [47].

Because of these advantages over the side-of-fringe lock, the PDH arrangement was first implemented. The laser frequency was modulated by modulating the current of the laser diode. This was done by the KILL control module built by B. Keitch, which supplies the appropriate RF frequency, and also demodulates this frequency from the detection photodiode signal. The demodulated signal is then used by the Toptica locking module to stabilise the laser frequency. The modulation frequency in our case was 170 MHz. This results in sidebands appearing next to the carrier optical frequency, with separation equal to the modulation frequency. The sidebands, however, introduced difficulties in conducting and interpreting the experiments, as it makes the frequency spectrum more complicated, with the appearance of many peaks and dark resonances. This effect can be eliminated by modulating the laser frequency not with the diode current directly, but using an electro-optical modulator (EOM) in the locking beam path, which introduces sidebands for that beam only. That is the approach that we adopted in the case of the 397nm laser (see next section). Alternatively, one can use a different locking mechanism. Because of the ease of setup of the side-of-fringe lock and the already good stability of the 866nm laser (even unlocked) we opted to use side-of-fringe lock for most of our experiments.

The frequency tuning of the laser is done by changing the length of the locking cavity by applying a voltage to the piezo crystal that holds one of the mirrors of the cavity. The voltage on the piezo crystal was set by a DC piezo driver, and this voltage was fine-adjusted by the experimental control computer. The frequency calibration as a function of this control voltage was experimentally determined. The calibration depends on the base voltage of the piezo driver, and it is non-linear over long ranges.

The control voltage produced by the experimental control computer was adjusted along its whole range [-2.5 V, +2. V], and the frequency was read off from the wavelength meter. The explored frequency region was small enough that the calibration can be approximated with a linear function. The recorded calibration data is plotted in Figure 4.6 and the fitted voltage dependence of the laser frequency is shown in Table 4.1 on page 43. The base voltage of the piezo driver is also shown, since the calibration is valid only using similar base voltages, due to the non-linear response of the piezo crystal.

Laser	Piezo base (V)	Calibration (MHz/ mV)	Resolved freq. steps (MHz)
397 nm	41	0.211(6)	0.52
866 nm	54.3	1.77(6)	4.3

Table 4.1: Calibration information of the Doppler-cooling and repumping lasers (as of 16.7.2007). The resolved frequency steps are due to the 12-bit resolution of the controlling DAC.

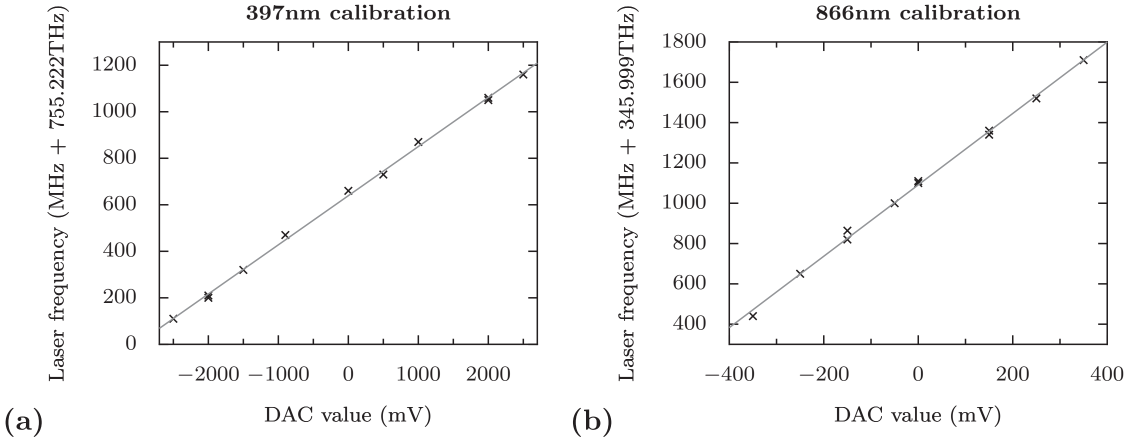

Figure 4.6: Frequency scan calibration of the 397 nm and 866 nm lasers. The experimental control computer's DAC output controlled a piezo driver to scan the locking cavity of the lasers. The laser frequencies as measured by a HighFinesse WS/7 Wavelength Meter are shown as a function of the DAC control voltage. The solid lines are linear fits to the data, the fitted calibration is given in Table 4.1.

Experimental beam of the 866nm laser

Order -1 is used for the experimental beam. To be able to electronically switch the beam on and off, it is guided through a double pass AOM (IntraAction ATM-851A2). The arrangement has approx. 60% double pass maximum efficiency (output power compared to input power when the AOM is on), and extinction of the order of 10^{-6} (residual intensity when the AOM is turned off).

The output beam is picked off with a PBS cube, and coupled into a single-mode, polarisation maintaining (PM) fibre (Nufern PM780-HP) with a Schäfter and Kirchhoff 60SMS coupler. The fibre has angle-polished faces (APC) to reduce back reflection and an angled fibre arrangement inside the coupler to increase coupling efficiency. The maximum achieved coupling efficiency is approx. 78%, which is close to specification.

The good quality output coupler and fibre improve the beam quality significantly, compared to early tests using other simpler couplers and fibres. Overall, the optical setup provides a frequency stabilised laser beam with good enough polarisation properties and power up to 5 mW. The polarisation and intensity stability at the fibre output are discussed in section 4.4.

4.2.2 397nm Doppler cooling laser setup

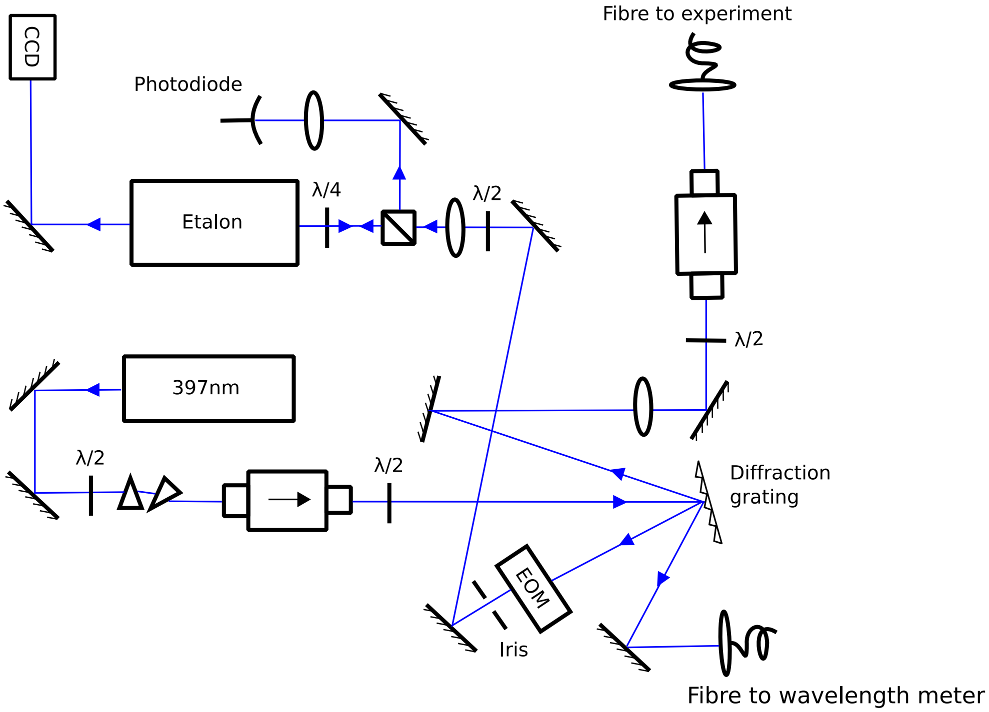

Figure 4.7: Layout of the 397nm laser system. Details in the text. Arrows on the beampaths show the direction of beam propagation. (Colour in electronic version)

The optical layout of the 397nm laser system is shown in Figure 4.7. The spatial profile of the output beam of this laser is highly non-Gaussian, see figure 4.8. The horizontal extent of the beam is quite large, and it has a "halo" area, that extends well beyond the detection area of the beam profiler used (the sensor area has 2 mm radius). An anamorphic prism pair makes the beam more circular, though with limited success.

A Toptica optical isolator is used to reduce the back-reflection into the laser diode. The Thorlabs GR13-1204 diffraction grating (1200 grooves/ mm, blaze-wavelength of 400 nm) divides the beam into three beampaths. Order +1 is coupled into a multimode-mode fibre which leads to the wavemeter system, 0 is used for frequency stabilization and -1 provides the experimental beam.

Frequency stabilisation of the 397nm laser

Order 0 goes through a Leysop PM type EOM which modulates the beam at 85 MHz for the frequency locking system. The modulation voltage is supplied by the KILL module

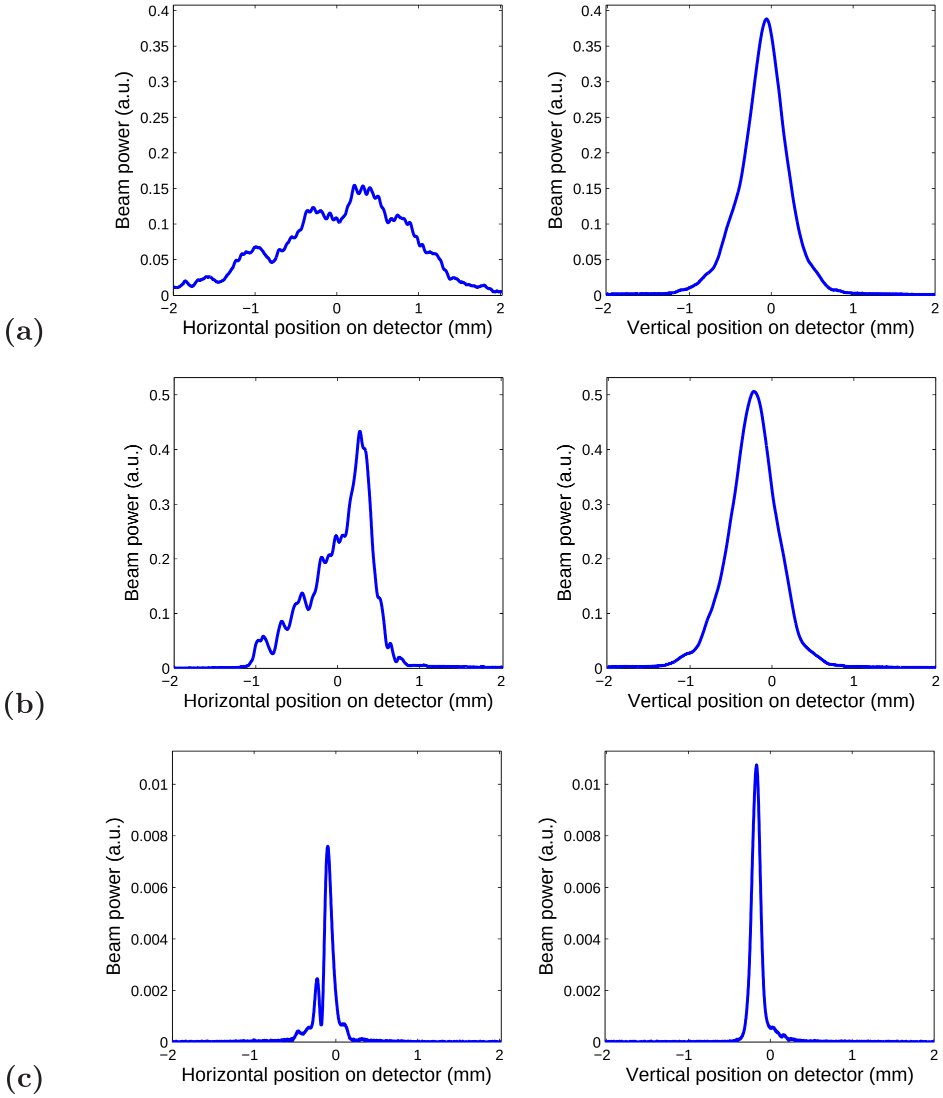

Figure 4.8: Beam profiles of the 397nm laser, at different points in the optical path. a) the laser output, b) after an anamorphic prism pair, c) the "experimental beam" before its fibre input. Measurements were taken with a Thorlabs BP104-UV beam profiler. Laser intensities are in arbitrary units. The laser output has a large horizontal extension, which is reduced with the prism pair. The fibre input beam is small in order to maximise the fibre coupling.

in the laser control box and is amplified by a Minicircuits RF amplifier. The beam then passes through an iris to clean the profile, a $\lambda/2$ plate to set the polarisation, and a 25 mm focusing lens. The transmitted beam after the NPL reference cavity is monitored by a CCD camera for diagnostic purposes. The reflected beam is picked off by the PBS cube (after twice passing through the $\lambda/4$ plate to rotate the polarisation by a total of

90°) and directed onto a Hamamatsu C5331 avalanche photodiode. The photodiode signal is demodulated by the KILL module, and the output goes to the locking module of the Toptica laser control box.

It has to be noted that, while usually the TEM00 mode of the reference cavity is the most suitable for locking, in this case the TEM10 mode appeared to have better properties (larger capture range and better stability) so it was used instead. This is possibly due to the non-Gaussian spatial profile of the beam.

The control of the 397 nm laser frequency was similar to that for the 866 nm beam. One difference between the two is, however, that the control voltage to the 397 nm cavity's piezo controller was reduced with an 11:1 voltage divider, to allow finer control of the laser frequency, at the expense of scanning range. The calibration of the frequency adjustment, together with the used piezo driver base voltage, is shown in Table 4.1

Experimental beam of the 397nm laser

The experimental beam originally had only a focusing lens before coupling into the single-mode fibre which does not maintain polarisation (non-PM). However, because the fibre had a flat polished face, there was enough reflected power to deteriorate the laser diode performance, even with the optical isolator in place. To eliminate this effect and improve stability, a second optical isolator was installed. The feedback effects stopped, but the optical isolator reduced the available laser power at the fibre output. Without the second optical isolator the maximum output power was approx. 200 μW; with the second optical isolator is in place this drops to 40 μW. Most of the experiments described in this thesis needed laser powers only $\sim$10-20 μW, but in the longer term several improvements are planned for the experimental beam. Using angle-polished fibres would eliminate the need for the second isolator since they reduce back-reflection and thus the optical feedback to the laser diode. A double-pass AOM would make possible fast switching of the beam, and also laser power stabilisation via an electronic feedback loop.

4.2.3 854nm repumping laser setup

Early in the experiments to load an ion into the trap, the fluorescence signal had behaviour reminiscent of "quantum jumps" if the oven and photoionisation lasers were left turned on after capturing an ion (see Section 6.1). The fluorescence signal disappeared and reappeared in a timescale of a few seconds.

The effect was due to shelving by the 389nm laser beam. It off-resonantly excites the ion into the $P_{3/2}$ state, from where the ion can decay into the $D_{5/2}$ metastable state. While the ion is in the $D_{5/2}$ state, the Doppler cooling lasers cannot interact with it, which results in loss of fluorescence. During the time the ion is shelved and not cooled, it can also be heated up enough to leave the trap.

There are two ways to eliminate this effect. The photoionisation lasers can be blocked immediately after ion capture. This method is used when loading a single ion. When blocking the photoionisation lasers is not possible (for example when trying to load multiple ions into the trap), a 854nm beam is used to repump from the $D_{5/2}$ to the $P_{3/2}$ state, deshelving the ion.

The requirements for this beam are not very stringent in our experiment. The frequency stability necessary is much less than for the 866 nm and 397 nm beams. High power in the beam relaxes this requirement, as the power broadening makes it possible to interact off-resonantly with the ion even with significant ($\sim 100\,\mathrm{MHz}$) detuning.

The 854 nm laser is also a Toptica DL100 diode grating stabilised in Littrow configuration. The layout of the system is shown in Figure 4.9. A Newport 53-004ZD02-035R diffraction grating splits the laser output into two beams, one for frequency diagnostics, one for the experiment. A double pass AOM is used for turning the beam on and off. A single-mode non-PM fibre is used to bring the experimental beam to the trap optical system. The current coupling efficiency is $\sim 20\%$ and the setup provides $\sim 1\,\mathrm{mW}$ of power at the fibre output end. This power proved to be sufficient, though it might be possible to achieve higher output power by improving the coupling with an additional focusing lens before the fibre coupler.

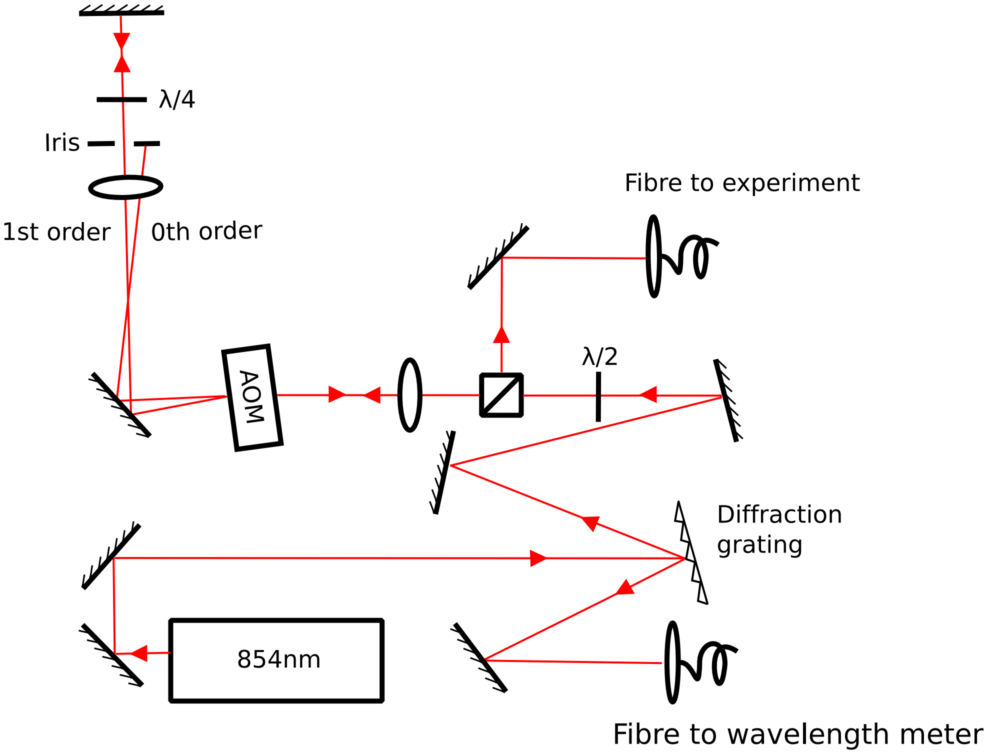

Figure 4.9: Layout of the 854nm laser system. Details in the text. Arrows on the beampaths show the direction of beam propagation. (Colour in electronic version)

4.2.4 Laser diagnostics

For coarse diagnostic of laser frequencies, a HighFinesse WS/7 wavelength meter was used. It is connected to a 8-to-1 fibre switcher, which allows us to monitor 8 different lasers at the same time.

A small portion of the laser light (10-100 μW) in each optical setup is coupled into a multimode fibre, and connected to one of the channels of the fibre switcher. The 8 channels of the switcher are sampled periodically, and the wavelength meter's control software displays measurement results.

The wavelength meter has a precision of 50 MHz in determining the laser frequencies. However, we observed a periodic fluctuation in the wavelength reading, see Figure 4.10. The fluctuation has amplitude approximately 40 MHz and period approximately 20 minutes. The long term stability is good. As discussed in section 4.7, this periodic change is probably due to the effect of the air conditioning system. The wavelength meter is located beneath one of the air ducts of this system, and probably the changing airflow in-

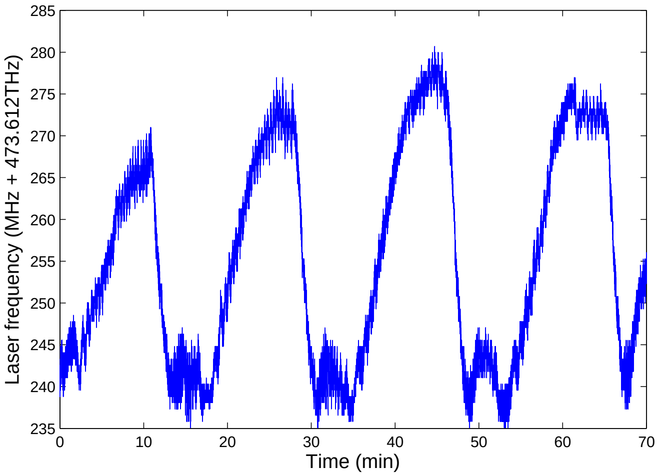

Figure 4.10: Frequency reading of a frequency stabilised HeNe laser (SIOS SL02/1) on the HighFinesse WS/7 wavelength meter. A section of a 6h logging period is shown. The laser has specified maximum excursion of ±25 MHz. A similar effect has been observed with the cavity-locked 866nm and 397nm lasers.

terferes with the precision measurements. Moving the wavelength meter to a more suitable position is currently under way.

Because of this periodic change and the inadequate precision, we use the wavemeter reading for coarse adjustments and to monitor whether the laser locking mechanism is operating correctly or an unlocked laser is drifting too far from the set point.

There are plans to implement a more thorough laser diagnostics system, a version of which is already in use with the previous generation of our ion traps. The new system includes two spectrum analysers (one for the IR and one for the UV lasers) and more sophisticated software. The improved software allows us to monitor simultaneously the properties of up to 8 different lasers: wavelength, spectrum and locking signal on the same display. This new system was created by D. Allcock [48] and a copy of it will be built for the optical setup described here in the near future.

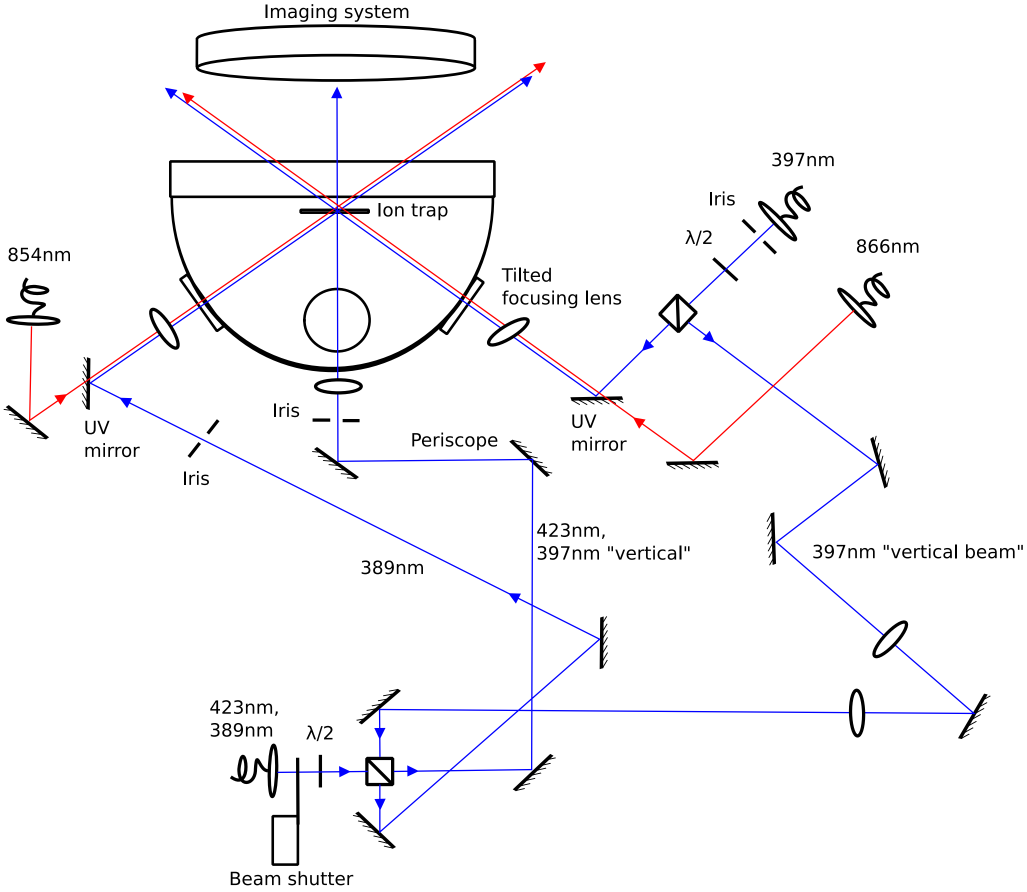

Figure 4.11: Optical setup at the trap, with beam directions. The "periscope" denotes the part of the optical setup where the joint 423nm and 397nm vertical beams leave the plane of the other beams, and are guided through the viewport on the upper part of the vacuum chamber. Thus the beam which appears to be directed towards the imaging actually system passes beneath the main imaging lens. (Colour in electronic version)

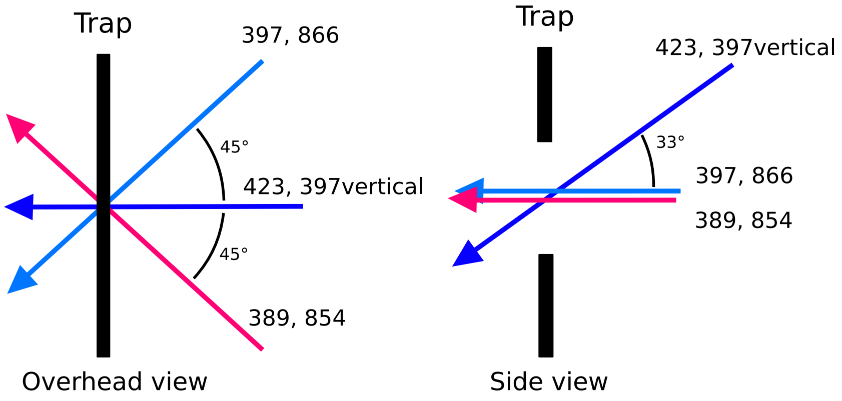

Figure 4.12: Schematic of the beam directions at the ion trap. The beam wavelengths are noted, together with the angles between the beams. (Colour in electronic version.)

4.3 Trap optical setup

4.3.1 Photoionising lasers

The photoionising lasers (423nm and 389nm) are shared between the experiments in two labs. The laser sources are physically in another lab, the beams are superimposed on a PBS cube and coupled into a Nufern S405 single-mode fibre. At the fibre output originally both wavelengths were focused into the trap by the same lens. However, because of chromatic aberration, the two beams have a focal length difference of about 3 mm, which is comparable to the Rayleigh ranges of the beams.

For better focusing, the beams were separated into two beam paths. This could be done using a $\lambda/2$ waveplate and a PBS cube after the fibre output since the beams have orthogonal polarisation due to the way they are combined before the fibre. Better than 97% of each beam power was in the right beam path. The 423 nm beam enters the vacuum chamber from a viewport on the top, the 389 nm beam through a side window. This allowed good focusing for both beams, which reduced scattered light, and smaller beam powers were sufficient to achieve the same loading rate.

Ideally, the 423 nm laser beam should be perpendicular to the atomic beam coming from the Ca oven, to minimise Doppler broadening. This would allow us to perform isotope-selective photoionisation, since the atomic excitation frequencies are different for the different Ca isotopes. In our case, however, the placement of the Ca oven and the input ports put constraints on the angle between the atomic beam and the laser beam. In practice, this angle for the natural abundance Ca oven is $\sim 70°$. Because of its position, the angle between the oven containing ^{43}Ca enriched sample and the laser beam is even smaller, $\sim 50°$ (see Figure 4.1 and 4.3). The effect of these angles is discussed in Section 5.3, describing the experiments observing neutral atom fluorescence in our trap.

4.3.2 Doppler cooling lasers

Fibres were used for both the 397nm and 866nm laser beams to bring them to the trap. Originally there was a single 397nm beampath, which was focused down to the trap by a short focal length (100mm) lens. This lens was tilted with an angle of approx 14°

such that it creates an elongated instead of a tight circular focus. The beam has waist $w_{0,horiz} = 87\mu$m in the horizontal direction and $w_{0,vert} = 25\mu$m in the vertical direction. The advantage of this arrangement is that while avoiding scattered light if the beam hits the RF electrodes in the vertical direction, there is still significant power in the beam along the trap axis in the horizontal direction. This allows us to move the ion a significant distance (approximately $\pm\ 50\mu$m) along the trap axis, and still be able to cool it and observe a good photon scattering rate. The 866nm beam is superimposed on the 397nm light with a near-UV mirror, which reflects the 397nm beam and transmits infrared wavelengths.

Early in the building of the optical setup a need for careful control of the beam polarisation was observed. The background scattered light had a significant polarisation dependence. Originally a $\lambda/2$ waveplate was used to minimise the background scatter by rotating the polarisation to be horizontal. This arrangement needed constant checking and tweaking. Subsequently, better performance was achieved by inserting a PBS cube into the beampath.

The transmitted beam of the PBS cube was used as the main experimental beam, the reflected beam was redirected and continued with the 423nm beam on the PBS cube already used to separate the two photoionisation beams. By use of appropriate lenses, it is possible to focus this secondary 397nm beam (or "vertical" beam) onto the same place in the trap as the 423nm beam.

While the horizontal beam has the whole 100 μm spacing between the RF rails to propagate through, the vertical beam has a reduced available cross-section, due to the angle at which it arrives at the trap. Also, due to the direction of the vertical beam, scattered light is more likely to get into the imaging system than in the case of the horizontal beam. We observed more than one order of magnitude higher background scatter counts on the PMT from the vertical beam than from the horizontal beam. Because of this problem, the vertical beam is only used in experiments when it cannot be avoided. Normally, only the horizontal 397 nm beam is present.

4.4 Polarisation and power stability

Many experiments with trapped ions require good polarisation and power stability. The stability of the 397nm and 866nm beams were measured at their respective fibre outputs. For each beam, two photodiodes were positioned so to measure the transmitted and reflected beams of a PBS cube after the fibre output.

The transmitted and reflected powers (I_T and I_R, respectively) were recorded for several hours. The polarisation angle is calculated from:

$$\theta = \arccos\left(\sqrt{\frac{I_T}{I_T + I_R}}\right) \tag{4.1}$$

Figure 4.13 shows the total beam intensity ($I = I_T + I_R$) and the calculated polarisation angle θ, as a function of time. It can be seen that both the powers and the polarisation, for both beams, have periodic structure, with an approx. 21 minutes period. This periodicity is correlated with the air conditioning system (see Section 4.7).

The 866 nm beam has better defined polarisation on the short timescale (seconds), while the 397 nm beam has a short term variation of ±0.25°. On the several minutes timescale, the polarisation variation of the 866 nm is approximately ±0.75°, while the 397 nm beam has variations in the order of ±0.5°.

One major difference between the two fibres is their stability against mechanical disturbances. The PM fibre of the 866nm beam keeps its polarisation if it is set up correctly, while the output polarisation of the non-PM fibre of the 397nm beam changes completely if it is touched. In the test experiment care was taken not to disturb the fibre, to be able to observe the additional (not "accidental") effects on polarisation.

The polarization stability of the non-PM fibre is somewhat improved by introducing a low level of stress to the fibre, by e.g. bending a section of it with a few cm radius. This arrangement makes the fibre birefringent which improves the polarisation stability along the fast axis. It also creates large bending losses if the bending radius is small. In our experiments the radius was large enough (~5-10 mm) not to introduce significant bending loss. Fortunately, the experiments described in this thesis are of a pilot nature and variations of polarisation of the order of a degree or so are of no significance.

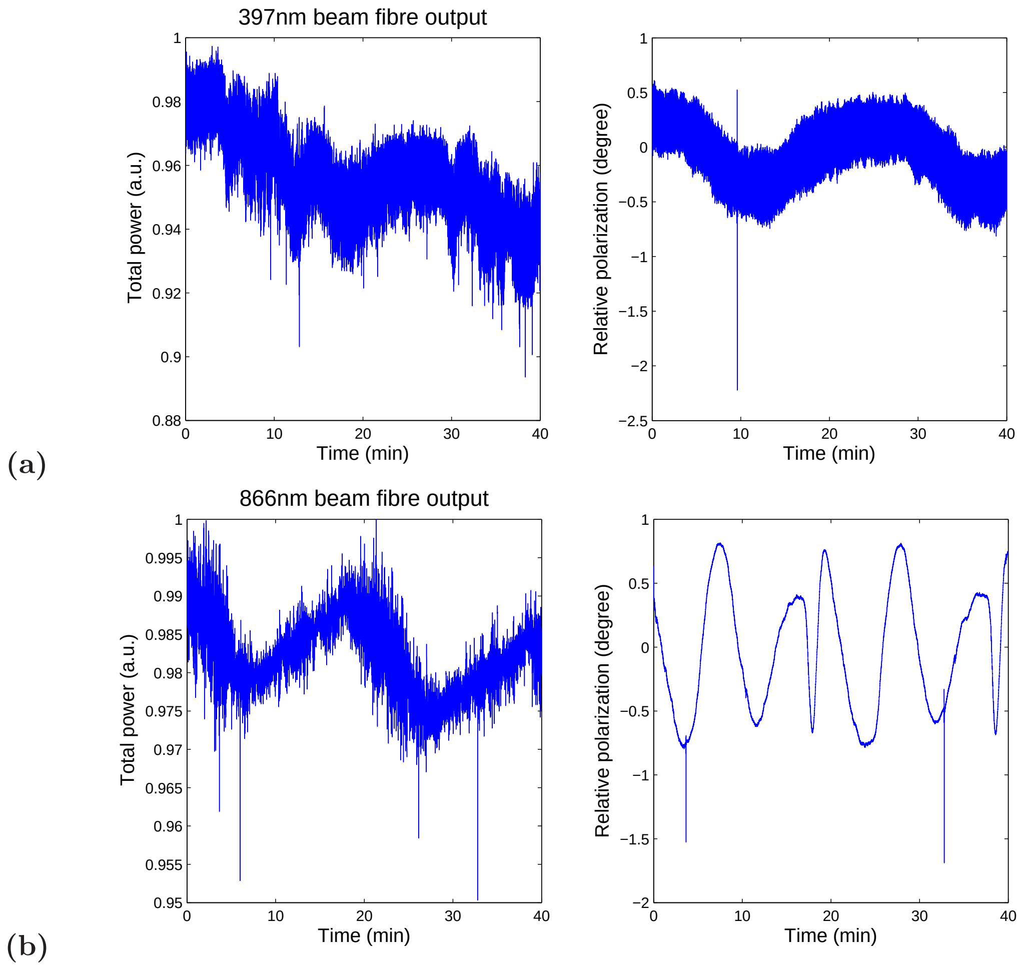

Figure 4.13: Fibre output polarisation and intensity for a) 397nm beam (non-PM fibre), b) 866nm beam (PM fibre). The PM fibre has better defined polarisation on seconds to minute timescales. Both fibres exhibit an approx. 20 minutes periodicity in polarisation (more obvious on longer recorded sequences, not shown here). The 866nm beam also shows periodicity in intensity, while in the 397nm beam it is hidden by the intensity drift. The “dropouts” are due to measuring photodiodes.

Similarly, the periodic change of the fibre output power may also pose problems to more sophisticated experiments, in our case, however, this change was not significant. If needed, improved power stability can be achieved by a feedback loop with an AOM on the fibre input side.

4.5 Imaging system

An outline of the imaging system is shown in Figure 4.14. The vacuum chamber's largest viewport was chosen to be the detection route for the ion fluorescence signal. Its design allows a large imaging lens to be brought close to the viewport, thus increasing the solid angle in which the signal can be collected.

A Nikon ED PLAN 1.5X wide aperture composite lens collects the light from the ion, with numerical aperture of $\sin\Theta \approx 0.29$, which corresponds to a collection efficiency of 0.021. The Nikon lens images the ion with a magnification of 8 onto a pinhole of 1 mm diameter. The pinhole is used to exclude light scatter from the trap electrodes. The light is re-imaged onto a photo-multiplier tube (PMT) and an image-intensified CCD camera (EEV Super Photon ICAM2-07-06E) using two lenses (Comar 50DQ25, $f = 50\,\mathrm{mm}$). A beam-splitter is used to divide the light into two beam paths for the PMT and the CCD. When visual information about the ion is not needed, the beam-splitter can be moved out of the beam path, to maximise the fluorescence signal on the PMT.

A pair of interference filters are placed in front of the PMT to transmit only around 397 nm. They are mostly aimed at reducing background light from the photoinisation beams at 389 nm and 423 nm.

A second, smaller pinhole of $350\,\mu\mathrm{m}$ diameter is placed in front of the PMT, further reducing the background scattered light, while transmitting the fluorescence from the ion. The PMT is connected to the measurement control computer, which processes its output.

Table 4.2 contains the calculation of the estimated detection efficiency, based on the parameters of the optical elements, which gives $\eta = 0.16(3)\%$. The error is calculated assuming a 10% error on the collection efficiency and 5% error on all other parameters. For the neutral atom fluorescence experiments (see Chapter 5) the interference filters were removed, thus the estimated detection efficiency was $\eta = 0.19(3)\%$.

More details of the imaging system are given in Appendix C of [49].

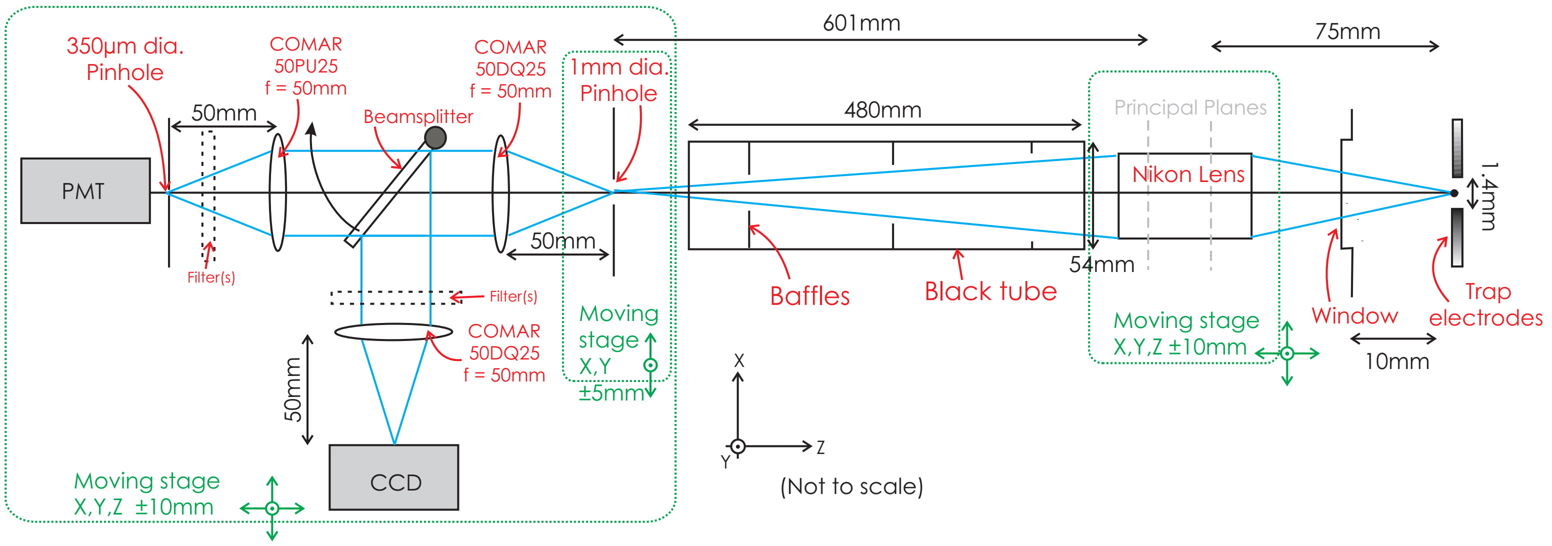

Figure 4.14: Schematic layout of the imaging system, from A. Myerson [49]

Collection efficiency	0.021
Output window T	0.92
Nikon lens T	0.73
$2\times$ Comar lens T	0.85
Interference filters T	0.86
PMT quantum efficiency at 397 nm	0.16
Overall detection efficiency	0.16(3)%

Table 4.2: Summary of the calculation of the expected detection efficiency of the photon collection system.

4.6 Electronics

4.6.1 Control computer

The experimental apparatus is controlled by a central computer. Two digital-analog input/output cards (DAC) (PCI DAS-1200 and PCL-727 models) are used to interface the various items of equipment (see Figure 4.15).

The experimental control program running on this computer uses a time-to-amplitude converter (TAC) to read photon counts from the photomultiplier tube (PMT). The sync signal of the RF voltage source is also connected to the TAC, to provide information about correlation between the RF-phase and photon arrival times. This correlation information was used for ion motion diagnostics, see Section 6.2.

The PCI DAS-1200 card is used for most of the experimental control. One of the DAC analog input channels records the ion gauge current for pressure measurement and another channel logs the photodiode current in some experiments to measure laser intensities.

A digital output channel triggers a shutter to block and unblock the photoionisation beams at their fibre output, and another digital channel controls the AOM driver of the 866nm laser setup. Analog output channels control the wavelength of the cavity-locked 397nm and 866nm by piezo-control of the cavity length. The calibration of these channels is shown in Table 4.1.

The PCL-727 card provided extra analog and digital outputs when needed.

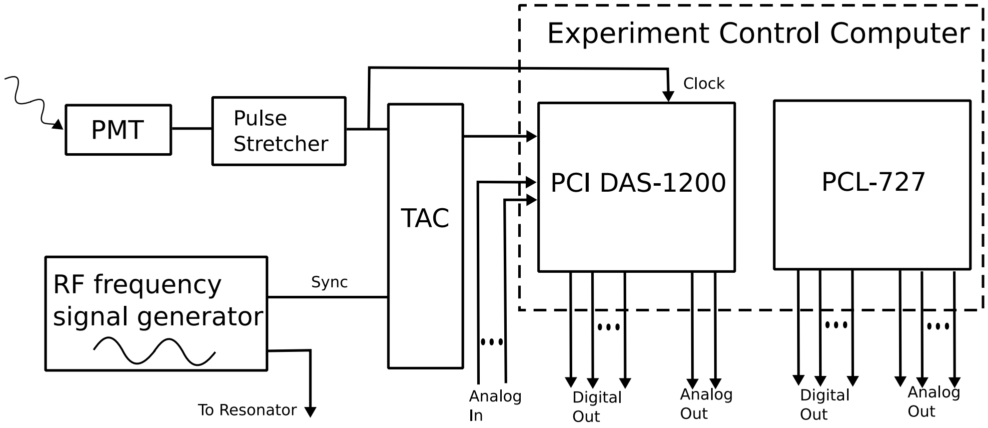

Figure 4.15: The connection layout of the experiment control computer. The wiring information of the PCI DAS-1200 and PCL-727 cards and the connected input and output channels are in the text.

4.6.2 DC electrodes and secondary control computer

In the early experiments the voltages for DC electrodes were provided by TTi stabilised power supplies. However, this only allowed restricted setting of the electrodes. Because of the limited number of power supplies, many of the DC electrodes had to be set to the same voltage. For the first attempt to trap ions this was sufficient. As soon as compensation of stray electric fields was necessary for more sophisticated experiments, the number of power supplies and their control became a limiting factor.

Ultimately the setup was changed such that the DC electrodes were controlled by computer via a Measurement Computing DAC6703 16-channel D/A converter card. 14 channels were used to set voltages in the ±10 V range separately for all 14 DC electrodes. This allows complete compensation of the electric field. The computer control is also capable of outputting voltage waveforms to the electrodes to move ions in the trap.

The outputs of the DAC card are distributed by a breakout box with BNC connectors. This is connected to a second, specially designed box to package voltages from different sources into a D-type cable, which delivers them to the vacuum feedthrough that is connected to the ion trap chip carrier inside the vacuum system. The BNC cables provide better shielding against electromagnetic noise than the D-type cable.

To reduce the electromagnetic noise, a filter box was inserted between the vacuum feedthrough and the D-type cable. The filter box contained a separate RC circuit as a low pass filter (R=1.8 kΩ, C=0.1 μF, time constant $\tau = 0.18\,\mu$s) for each voltage supply line to the DC electrodes, 14 filters altogether. A detailed investigation of the issue of electromagnetic noise and its effect on the ion is discussed in Section 7.2.2.

The control computer for the electrodes is separate from the measurement computer. The voltages were set by a Matlab graphical interface program developed for this task, running on Windows or Linux, depending on the experiment conducted, because of certain limitations of both systems. More about the specific control program will follow in the section describing the various experiments.

In addition to controlling the DC electrodes, this secondary control computer is also used to capture images of the ions, by connecting to the CCD camera of the imaging system.

4.6.3 Helical resonator

To amplify the radio-frequency voltages applied to the RF electrodes in the ion trap, we use a helical resonator [50]. It was built by J. P. Home [51]. The resonance frequency was measured to be 27.25MHz, and the Q-factor of the resonator was determined to be approximately 20. This, however, can be only checked before connecting the resonator to the electrodes, which means the actual Q-factor (and hence the exact voltages applied to the RF electrodes) is unknown. The Q-factor can later be deduced by comparing observed radial trap frequencies with calculation from the electrode geometry. The experiment is described in Section 6.4 and the results are consistent with the predictions.

The output of the helical resonator is connected to the RF rails through a vacuum feedthrough on the top of the vacuum chamber (see Figure 4.1). The connections had to be carefully made to minimise the losses and deliver as much power as possible to the RF rails.

4.7 Air conditioning

Air conditioning is a new feature of the refurbished labs. It provides greater temperature stability, which is very helpful for the optical setup. However it is not perfect. To check how efficiently the air conditioning system stabilises the temperature, a long term (25 days) temperature logging was conducted in the lab, with two temperature sensors (see Figure 4.16). The lack of a reheating module in the air conditioning system means there is a 0.5° temperature swing, on the time scale of approximately 20 minutes. Beside the short time scale temperature change, there is also a daily variation.

The effect of this temperature change is clearly visible on the precision elements of the optical setup, as already noted. The laser fibres are the most affected; the polarisation and intensity of the output beams change with similar periodicity to the temperature. There are various possibilities for the cause of this correlation. The way the fibres are routed close to the ceiling between the optical and experimental table brings them close to the air outputs of the air conditioning system. Changes of airflow during the air conditioning cycle or the temperature change may cause mechanical stress in the fibres. This might be reduced by using thicker protective tubing for the fibres, but this is yet to be tested.

The effect of the air conditioning on the wavemeter is harder to eliminate. Fortunately most of the time precision wavemeter readings are not essential for the experiment. The wavemeter serves as a crude and quick diagnostic for laser frequency jumps or drifts. Precision frequency measurements are done using the atomic transitions and fluorescence.

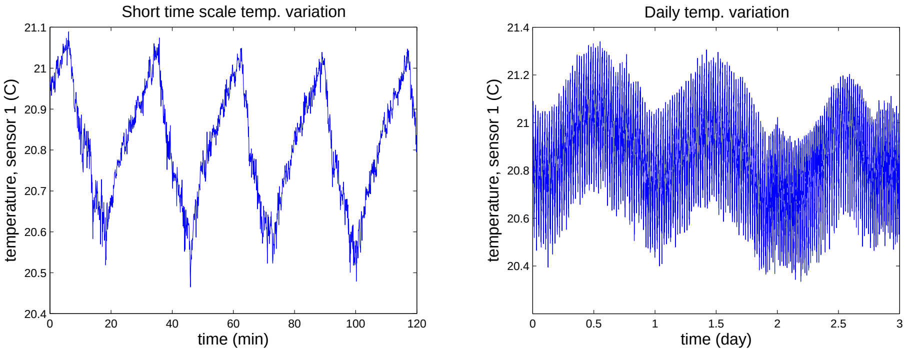

Figure 4.16: Temperature variations of the lab measured by a thermocouple placed on the shelf containing the wavelength measurement hardware. The periodicity is in step with the the air conditioning system's on/off cycles. Both short time scale and daily variations are present.

Chapter 5

First observations

This chapter describes the preparation of the Sandia trap for operation. Preliminary tests of the Ca oven were conducted. Assembly and bake-out of the vacuum system took place. The Ca oven was tested in experimental conditions by observing neutral atom fluorescence, to characterise the oven and the neutral excitation 423 nm laser beam, as a necessary step towards attempts to produce and trap ions.

5.1 Preliminary Ca oven experiment

In the course of preparing the Ca oven for the experiment, suitable electric current parameters had to be estimated. Too high a current would cause Ca deposits on the ion trap chip, while too low a current would not provide an observable flux of Ca.

David J. Szwer conducted a series of experiments to determine the temperature of a Ca oven as a function of the driving current [52]. This calibration can be compared to the records of running other Ca ovens in previous ion traps in our lab.

DJS prepared an oven as described in Section 4.1.3 (page 37). It was filled with granules of calcium metal under dry nitrogen to reduce oxidisation. The oven was mounted on stainless steel rods inside a simple vacuum chamber, with thermocouples attached to its surface.

As current was passed through the oven, the thermocouples measured its temperature. It was found that the thermocouples appeared to underestimate the temperature of the

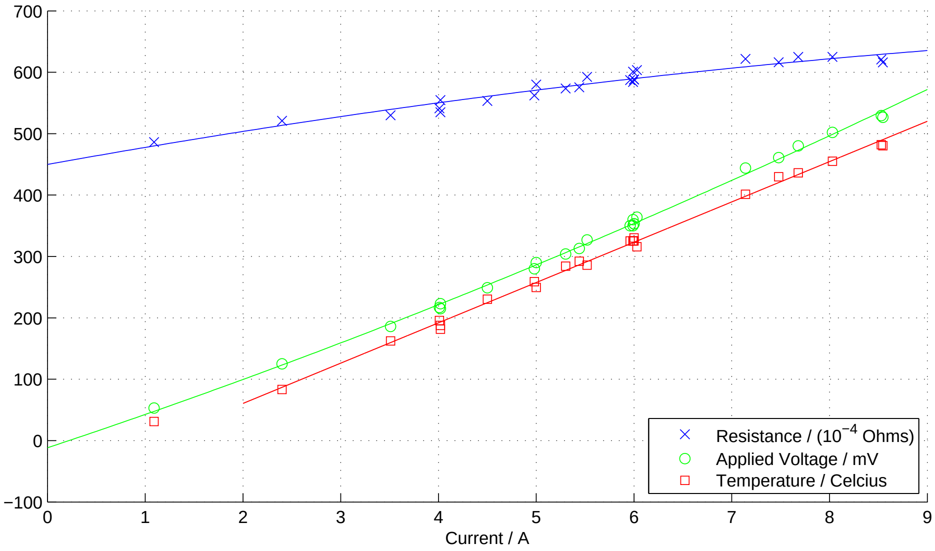

Figure 5.1: Results of Ca oven test experiment. Temperature, voltage drop and resistance of a Ca oven are shown as functions of applied drive current. The data are combined from two experimental runs. Temperatures are measured by thermocouples and have been corrected with reference to an optical pyrometer, see text. The solid lines are polynomial fits to the data. (Colour in electronic version.)

oven. To calibrate the thermocouples, an optical pyrometer (made locally) was used to estimate the temperature of the oven. This operated in the temperature region where the glow of the oven was visible, and it was assumed afterwards that the calibration can be extended from the high temperatures down to room temperature.

Measurements were made up to 9A drive current. The results for oven temperature and oven resistance as functions of driving current are presented in Figure 5.1. Earlier ovens were operated at ∼300°C [41], which corresponds to 5.5A drive current for the oven described above.

5.2 Bake-out of the vacuum system

The assembly and bake-out of the vacuum system took place in several steps. Some experimentation with the bake-out oven was needed to set up the hardware (electronics, heating elements, thermal insulation) and diagnostics logging system. The elements of the vacuum system had different maximum temperature limits. At different stages of

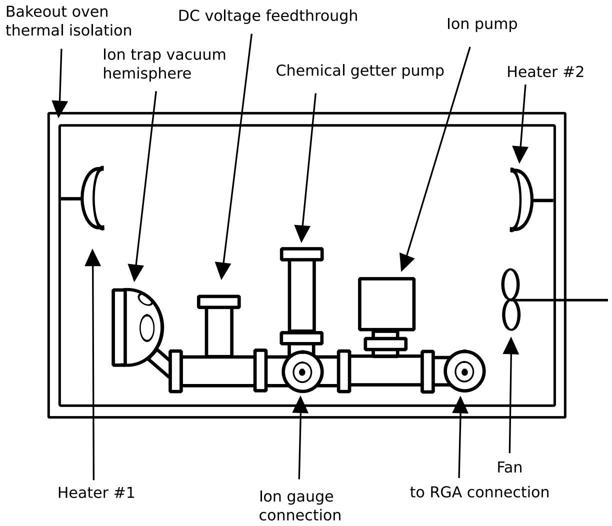

Figure 5.2: Schematics of the bake-out oven, with the vacuum system.

the preparation, as the more temperature-sensitive parts were assembled, the system was baked out at reduced temperatures. Also, the Sandia ion trap needed structural changes to its RF electrodes, as described in Section 4.1.2, which delayed its installation.

During the bake-out, 8 thermocouples were attached to different parts of the vacuum system, monitoring the temperature to ensure that no part overheated. The temperature measurement was also used to monitor the performance of the heater units, each consisting of 2 1000 W RS 196-6464 ceramic heating elements. The voltages supplied to the heater units were limited by variable AC transformers, to reduce the possibility of destructive electronic failures (accidental overheating). The air inside the oven was circulated by a fan, to provide a more uniform temperature.

Bake-out

The first bake-out took place starting on 11 May 2006. The system consisted of the vacuum chamber and the tubes for connecting the chamber to the ion gauge, the ion pump and the chemical getter pump. The electrical wiring inside the vacuum can, the Ca oven and the ion trap were not installed.

This “hard bake” of the vacuum can took 6 days: one day warm up to the maximum 300°C temperature, 4 days at that temperature, and one day to cool down. For the second bake-out, the ion gauge, the ion pump and the chemical getter pump were installed. This

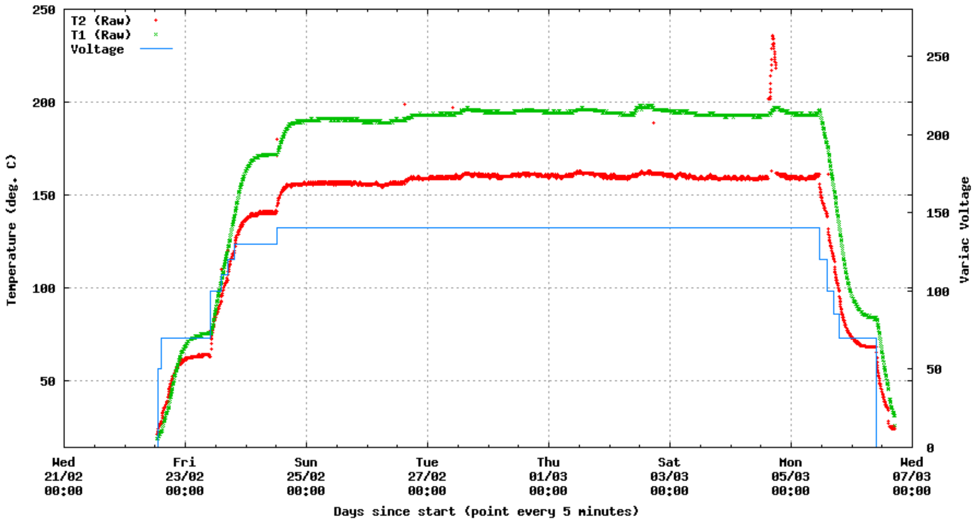

Figure 5.3: Temperature vs. time, and heater voltage vs time, during the final bake-out run. T1 and T2 are the temperatures measured by thermocouples taped to the hemisphere, and close to the top of the oven, respectively. Voltage is the drive voltage of the heater units. (Colour in electronic version)

bake-out started on 2 Jun 2006. It took 3 days to achieve the maximum temperature of 280°C. This was maintained for 6 days, after which the system took a further day to cool down. After the bake-out, the magnets of the ion pump were assembled, and the pump's operation was tested.

For the final bake-out, the Ca ovens were installed, the ion trap was mounted in its place inside the vacuum chamber and the ribbon cable connecting a voltage feedthrough and the ion trap DC electrodes was put in place.

In this bake-out, the maximum temperature was limited by the Kapton insulation of the ribbon cable. Kapton is a polyimide, widely used in industry, and has the advantageous property of very low outgassing rate. However, it is created chemically in temperatures of 200-300 °C. Because of this manufacturing process, during the bake-out the maximum temperature was limited to $\sim$ 200°C. Higher temperatures could lead to short circuiting and electrical failure of the DC electrodes, which are difficult to repair after the bake-out. The bake-out took 14 days starting on 22 Feb 2007, with a maximum temperature of 200°C.

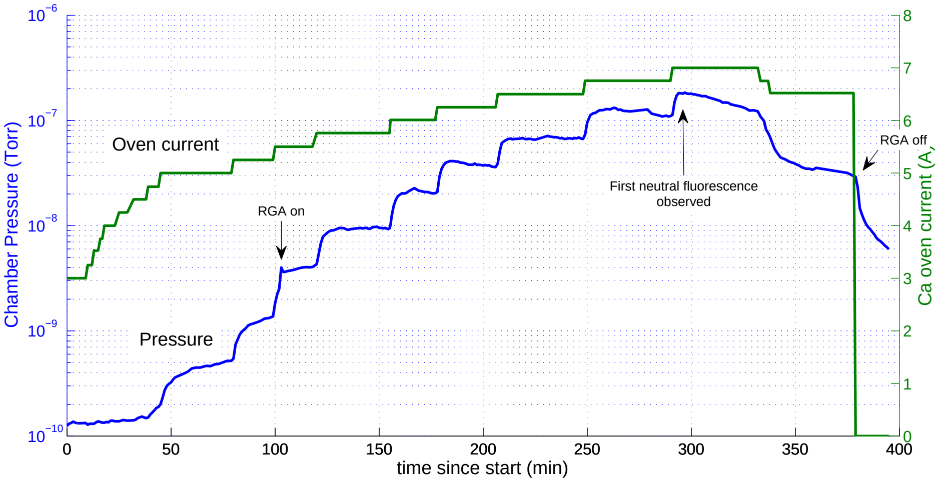

Figure 5.4: Pressure during the Ca oven degassing. The first observed neutral fluorescence is noted on the plot, at 7A oven current. Turning on the Residual Gas Analyser (RGA) temporarily increased the pressure. Each increase of the oven current resulted in increased pressure. The current was kept at the same level until the pressure approached equilibrium.

5.3 Neutral atom fluorescence

In the primary bake-out the calcium ovens were degassed only to the same extent as the rest of the vacuum system. The ovens were not heated up to their nominal operating temperature of 300-450°C by driving current through them. Thus inside the metal tube of the oven, absorbed in the calcium, was a supply of gases and a possible oxide layer on the surface of the calcium that had to be cleared out before the oven could operate.

To carry out a controlled degassing of the oven, the vacuum system was moved to its place in the experimental setup. A 423 nm laser beam was focused to the trap centre through the top viewport of the vacuum chamber. During the degassing, scattered light levels from the interaction region were recorded by a PMT while scanning the 423 nm laser frequency, checking for neutral Ca fluorescence. In another lab, the same 423 nm light was used in a known ion trap,from which the neutral fluorescence was monitored, providing information about the location of the atomic resonance in our frequency scan range. Also, a Residual Gas Analyser (RGA) monitored the gases leaving the oven. Pressures inside the vacuum chamber were recorded.

The current driving the calcium oven was increased from a starting value of 3 A in

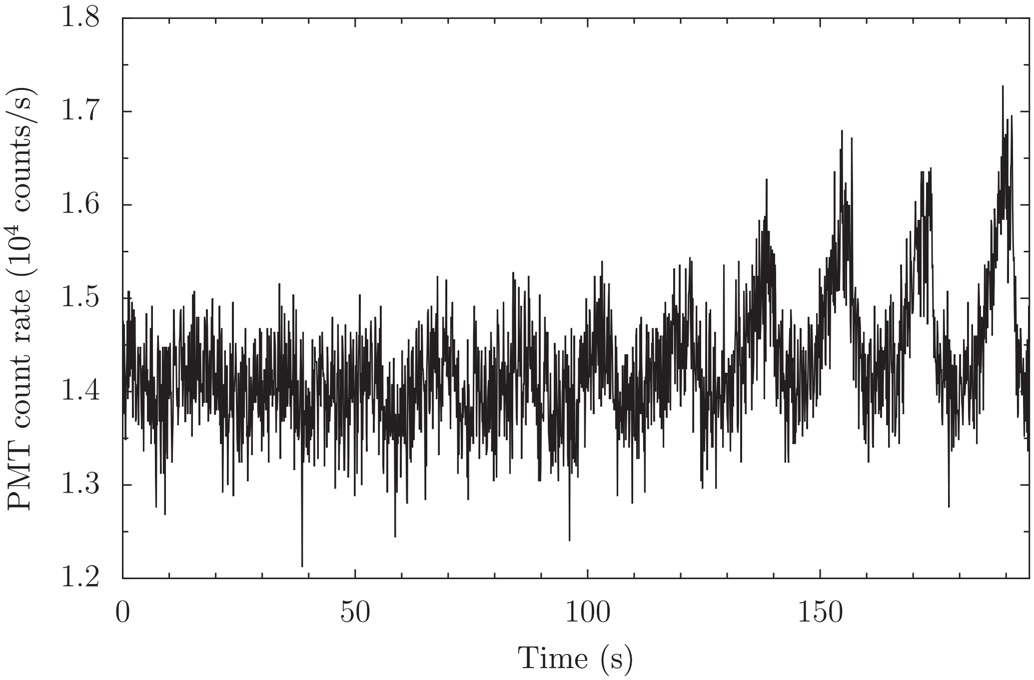

Figure 5.5: First observation of neutral fluorescence in the Sandia trap. PMT count rate is shown as function of time, where the frequency of the 423 nm laser was repeatedly scanned, with a rate of 18 s/scan. The oven current was increased shortly before the above scan was taken (see Figure 5.4). The resulting increase in oven temperature is causing the growth in the fluorescence signal across the plot.

0.25 A steps, and kept constant until the pressure inside the vacuum chamber was clearly stabilizing. The time-record of the vacuum chamber pressure and oven current is shown in Figure 5.4. The first observation of neutral fluorescence was recorded shortly after increasing the oven current to 7 A (see Figure 5.5).

After the first degassing, a pair of experiments were conducted to characterise the 423 nm laser beam and the Ca oven. In the first experiment the oven current was held constant, and the intensity of the 423 nm beam was varied. In the second experiment the laser intensity was held constant and the oven current was varied. In both experiments, the 423 nm frequency was scanned over the atomic resonance and the recorded fluorescence spectrum was fitted with a theoretical profile, which is described in the next section.

5.3.1 Doppler-broadened neutral fluorescence spectra

In the fitting procedure, the detected fluorescence signal with known detection efficiency is used to estimate the number N_e of excited atoms in the detection region and thus the

Variable	**Symbol**	**Initial estimate**	**Best fit**
Length of interaction region	d	$2.30 \times 10^{-4}\,\mathrm{m}$	-
Oven to trap distance	l	$2.2 \times 10^{-2}\,\mathrm{m}$	-
Angle of orifice normal to atomic beam	γ	$10°$	-
Angle between atomic and laser beam	θ	$80°$	$76.5(1.5)°$
Polarisation angle to detection system	φ	$57°$	-
Gaussian beam waist	w	$21.8\,\mu\mathrm{m}$	$22(4)\,\mu\mathrm{m}$
Oven temperature (at $I_{\mathrm{oven}} = 5.25\,\mathrm{A}$)	T	600K	640(10) K
Detection efficiency	η	1.9×10^{-3}	-
Oven orifice area	σ	$3 \times 10^{-7}\,\mathrm{m}^2$	-

Table 5.1: Summary of measured parameters used in the calculation. Initial estimates are listed, as well as the best fitted values of those that were allowed to float. Fitted values are shown for the experiment described in Section 5.3.2.

number density n of atoms in the detection region. This number density is related to the number density n_o inside the Ca oven, which can be translated into oven temperature T using the vapour pressure formula for Ca. The fluorescence profiles are thus used to characterise the Ca oven, the beam size of the 423 nm laser beam and the geometry of the atomic and laser beams. Table 5.1 summarises the parameters used, and their initial estimates. For parameters estimated from the fluorescence, the best fitted values are listed.

Consider a neutral ^{40}Ca atom subject to 423 nm radiation of intensity I. The probability of excitation to the $4s4p^1P_1$ state is

$$p(I,\Delta) = \frac{IA^2/4}{(2\pi\Delta)^2 + (A/2)^2 + IA^2/2} \tag{5.1}$$

where A is the Einstein coefficient for the transition, Δ is the detuning and the intensity I is expressed in units of the saturation intensity I_S, defined by

$$I_S = \frac{4\pi^2\hbar c A}{3\lambda^3}. \tag{5.2}$$

In Equation 5.1 the effect of the laser line width is not included. The laser line width is of the order of 4 MHz [41], which is small compared to the Doppler-spread of the spectrum (several hundreds of MHz). Also, the uncertainties in a number of variables have a larger effect on the fit than the laser line width.

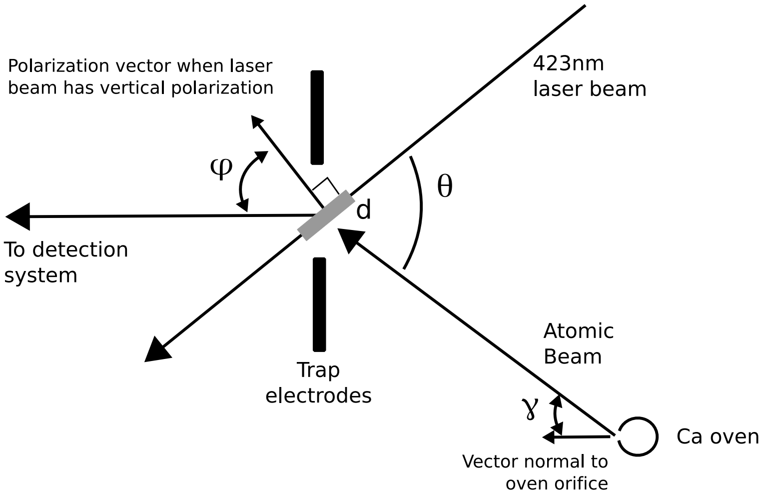

Figure 5.6: The angles used in the text for the calculation of the expected fluorescence signal.

In the case of moving atoms, the detuning is:

$$\Delta = \Delta_L + \Delta_D \tag{5.3}$$

where Δ_L is the detuning of the illuminating laser from the line-centre of a stationary atom, and Δ_D is the Doppler shift:

$$\Delta_D = -\frac{v}{\lambda} \cos\theta \tag{5.4}$$

where θ is the angle between the laser beam and the direction of propagation of the atomic beam (see Figure 5.6), and v is the atom's velocity.

The probability distribution of Δ_D is derived from the longitudinal velocity distribution in a volume for an atomic beam:

$$f(\Delta_D)\mathrm{d}\Delta_D = 4\sqrt{\frac{\beta^3}{\pi}}\Delta_D^2 \exp\left(-\beta\Delta_D^2\right) \mathrm{d}\Delta_D \tag{5.5}$$

where

$$\beta = \frac{M\lambda^2}{2k_\mathrm{B} T \cos^2\theta} \tag{5.6}$$

where M is the atomic mass, k_B is the Boltzmann factor, and T is the temperature of the oven. In Equation 5.5 $f(\Delta_D)$ is normalised assuming that $\Delta_D < 0$, which is the case in our trap, because θ is less than 90°.

The intensity of the laser beam is assumed to follow a Gaussian profile:

$$I(r) = I_0 \exp(-2r^2/w^2) \tag{5.7}$$

where r is the distance from the axis of the light beam and w is the spot size in the interaction region.

Consider the number of excited atoms (N_e) along a length d, lying between r and $r + dr$, with velocity defined by Δ_D:

$$\mathrm{d}N_e(r, I(r), \Delta) = 2\pi r \,\mathrm{d}r\, d\, n\, p(I(r), \Delta)\, f(\Delta_D)\mathrm{d}\Delta_D \tag{5.8}$$

where n is the total number density of atoms in the interaction region.

To calculate the number of excited atoms in the interaction region, we have to integrate Equation 5.8 over r and Δ_D. To simplify the integral over r we write

$$\alpha(\Delta_D) = \frac{(2\pi\Delta)^2 + A^2/4}{I_0 A^2/2} \tag{5.9}$$

and

$$x = 2r^2/w^2. \tag{5.10}$$

Then

$$N_e = \frac{\pi n d w^2}{4} \int\int \frac{1}{\alpha(\Delta_D)\exp(x) + 1} dx f(\Delta_D)\mathrm{d}\Delta_D = \frac{\pi n d w^2}{4} C \tag{5.11}$$

where

$$C = \int \ln\left\{1 + \frac{I_0 A^2/2}{(2\pi\Delta)^2 + (A/2)^2}\right\} f(\Delta_D)\mathrm{d}\Delta_D. \tag{5.12}$$

We note that in the case of laser intensity well below saturation ($I_0 \ll 1$), this expression can be simplified using $\ln(1 + x) \approx x$ when $x \ll 1$:

$$N_e = \frac{\pi n d w^2 I_0}{4} \int \frac{A^2/2}{\Delta^2 + (A/2)^2} f(\Delta_D)\mathrm{d}\Delta_D \tag{5.13}$$

We obtain the observed count rate S of the fluorescence from the number of excited atoms in the interaction region as

$$S = \eta N_e A \rho \tag{5.14}$$

where η is the efficiency of the detection system for isotropically radiated light, and ρ is a factor to take into account polarisation effects in the detection system and the angular distribution of the scattered light. Following a calculation of ρ in [53], if the polarisation of the incident light is at angle φ to the axis of the imaging system:

$$\rho = \frac{3}{2} \sin^2 \varphi \tag{5.15}$$

Now we need to relate the number density n_0 in the Ca oven to S. We can obtain the number of excited ^{40}Ca atoms in the interaction region as

$$N_e = \frac{2S}{3\eta A \sin^2 \varphi} = \frac{1}{4} \pi n d w^2 C \tag{5.16}$$

using equation 5.11. Hence the number density in the interaction region is

$$n = \frac{8S}{3\pi d w^2 \eta A C \sin^2 \varphi} \tag{5.17}$$

This is related to n_0 as

$$n = \frac{n_0 \sigma \cos \gamma}{4\pi l^2} \tag{5.18}$$

where σ is the area of the oven aperture, l is the distance from the oven to the interaction region, and γ is the angle between the normal to the aperture and the atomic beam. Thus

$$n_0 = \frac{32 l^2 S}{3 d \sigma w^2 \eta A C \cos \gamma \sin^2 \varphi} \tag{5.19}$$

The oven contains other isotopes besides ^{40}Ca, so we have to include the relative abundance of ^{40}Ca in the expression. In the oven used, this is the natural abundance $a_{40} = 0.969$.

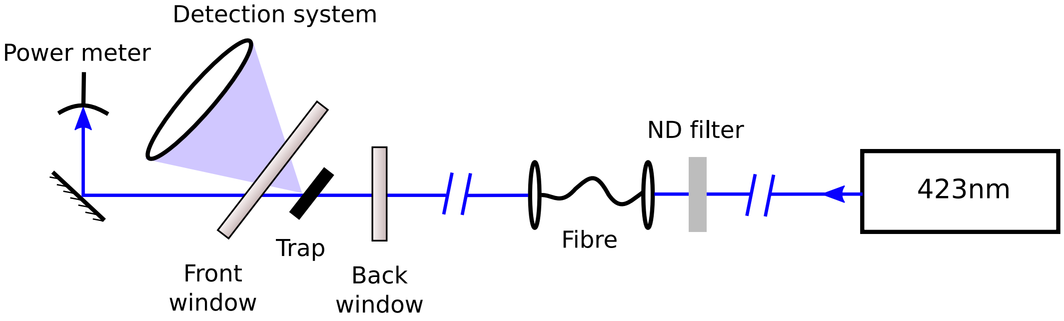

Figure 5.7: Layout of the experiment for varying 423 nm laser power. Vertical breaks in the laser line indicate additional optical elements for beam guiding.

The complete number density of Ca in the oven is thus

$$n_{0,Ca} = \frac{32l^2 S}{3a_{40} d\sigma w^2 \eta AC \cos\gamma \sin^2\varphi} \tag{5.20}$$

The number density inside the oven is related to the p vapour pressure of Ca as

$$n_{0,Ca} = \frac{p}{k_{\mathrm{B}} T} \tag{5.21}$$

The vapour pressure has an experimentally determined dependence on temperature. The empirical formula from the literature [54] is:

$$\log_{10} p[\,\mathrm{Torr}] = -52.23\frac{U}{T[\,\mathrm{K}]} + B \tag{5.22}$$

where p is in Torr, and T is in K. For our temperature region, the constants are $U = 195, B = 9.697$. By combining Equations 5.21 and 5.22 we can determine the oven temperature from the number density.

5.3.2 Saturation effects

In the first experiment with neutral Ca atoms the 423 nm laser power was varied while the oven current was kept constant. This allowed us to derive the laser beam size and incidence angle, as well as the number density of neutral atoms and oven temperature at the given oven drive current.

The optical setup is outlined in Figure 5.7. The laser beam is coupled into an optical fibre to transfer it to the trap, which ensures that the beam profile stays the same at the output end, regardless of the laser power. The laser power is adjusted by using different neutral density filters on the fibre input end, and measured after the vacuum chamber with a power meter. The laser power and the peak intensity are connected by

$$I_0 = \frac{2}{\pi w_H w_V} P \tag{5.23}$$

where w_H and w_V are the Gaussian beam spot size in two orthogonal directions (in this case, horizontal and vertical, respectively). When measuring the beam profile, w_H and w_V can be observed separately, while from fitting the data, only the geometric average beam size $w' = \sqrt{w_H w_V}$ can be deduced. The beam parameters were measured with a CCD camera as $w_H = 19\,\mu\text{m}$ and $w_V = 25\,\mu\text{m}$ ($w' = 21.8\,\mu\text{m}$), before aligning the beam into the trap.

The observed fluorescence is recorded as a function of the laser frequency, scanning over the Doppler-broadened transition. The signal is fitted as

$$S = K_1 C(\Delta, X) + B \frac{I_0(\Delta)}{I_0(0)} \tag{5.24}$$

where B is a fitted parameter associated with the background scatter,

$$K_1 = \frac{\pi \eta A \rho n d w^2}{4} \tag{5.25}$$

and

$$C(\Delta, X) = \int \ln \left\{ 1 + \frac{I_0(\Delta) A^2/2}{\Delta^2 + (A/2)^2} \right\} f(\Delta_D, X) \mathrm{d}\Delta_D \tag{5.26}$$

and because the oven temperature and the laser incidence angle influence the spectra the same way, they are fitted as a single parameter:

$$X = T \cos^2 \theta \tag{5.27}$$

Equation 5.24 includes the possibility that the laser intensity varies with the laser fre-

Parameter	**Fitting type**
K_1	(global) / individual
K_2	individual
X	global
B	individual
Δ_{offset}	individual
w	global

Table 5.2: The list of fitted parameters of the experiment in Section 5.3.2. Parameters with "individual" fitting had separate value for each scan, while global parameters had a single value for the complete experiment.

quency, expressed as

$$I_0(\Delta) = \frac{2}{\pi w^2}(P + K_2\Delta) \tag{5.28}$$

where P is the measured laser power at zero detuning and K_2 is a fitted slope parameter. All detunings are expressed as the measured laser frequency and an offset (that has to be fitted):

$$\Delta = \Delta_{\text{measured}} + \Delta_{\text{offset}} \tag{5.29}$$

One also has to compensate for the fact that the measured laser power is less than the power experienced by the atoms, due to losses on the exit window and the mirror before the power meter. Because the window does not have an anti-reflection coating for the 423 nm wavelength, based on previous experience we assumed a 10% loss. Thus all measured P laser powers are scaled up by 10% in the subsequent analysis.

Table 5.2 summarizes the fitted parameters. Due to the setup of the experiment, certain parameters should be the same for all scans: the laser incidence angle θ, the laser beam size parameter w and the number density n of Ca atoms in the interaction region. The incidence angle should be stable because the beam is not moved, the laser beam size because the fibre keeps the beam shape regardles of the input laser power, and the number density because the oven drive current (and thus temperature) is not changed throughout the experiment. However, early in the data analysis it was discovered that it is not possible to reconcile these three global parameters completely because the quality of the scans was insufficient. With such high background, laser intensity variations turned out to be the limiting factor.

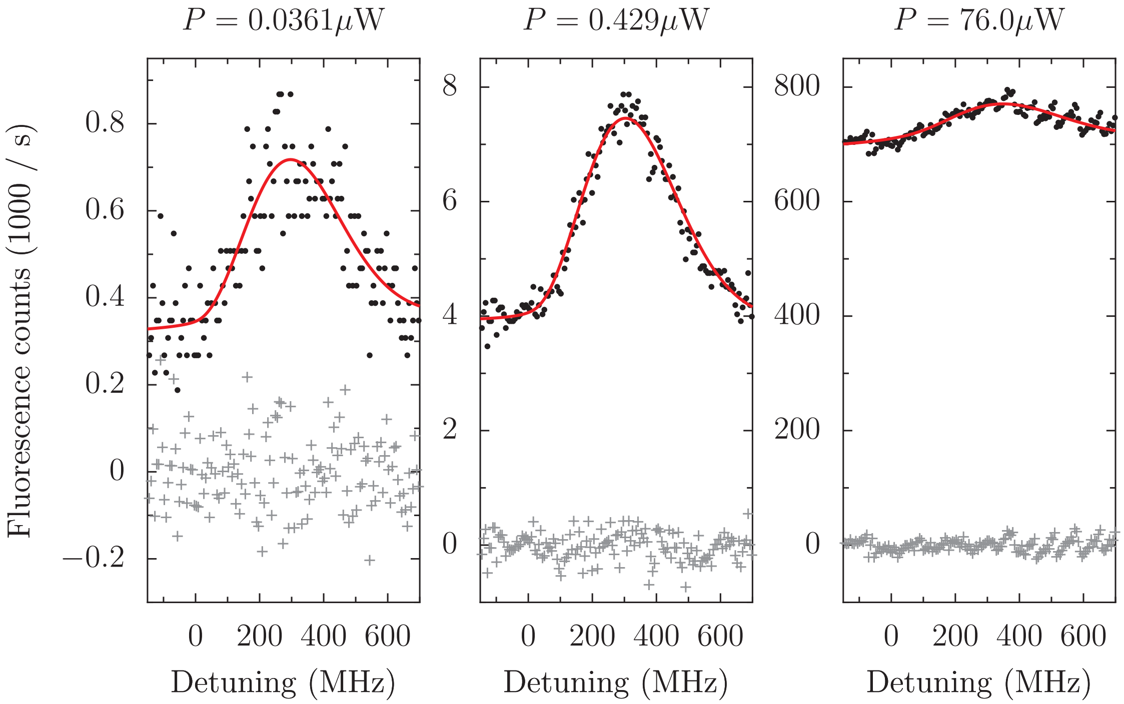

Figure 5.8: Examples of recorded neutral fluorescence as a function of 423 nm laser detuning, at different laser intensities (11 scans were taken in total). The theoretical fit and the residuals are shown. Note the transition in the residuals from statistical variations in a small signal at low power to systematic behaviour due to intensity variations at high power (see text).

In the low intensity scans the residuals were mostly statistical in nature, while the high intensity scans had low signal-to-noise ratio due to high background scatter levels, and the residuals appeared to have a systematic structure, comparable in size to the fluorescence signal (see Figure 5.8). This made the fits of the high intensity scans less reliable. In general these high frequency intensity variations do not necessarily alter the outcome of the fit, but we note that a slow variation is also present, as shown by the fit parameter K_2. There are likely to be also medium frequency variations, that would indeed change the fitted signal height and cannot be factored out.

The high frequency variations are thought to be due to unwanted optical feedback from the fibre input coupler to the laser. The fibre input had a flat-polished face, which does not prevent back reflection. As the laser intensity was adjusted before the fibre coupler, the reflected light had to go through the neutral density filters twice. At low intensities this must have reduced the reflected light to a level which did not affect the

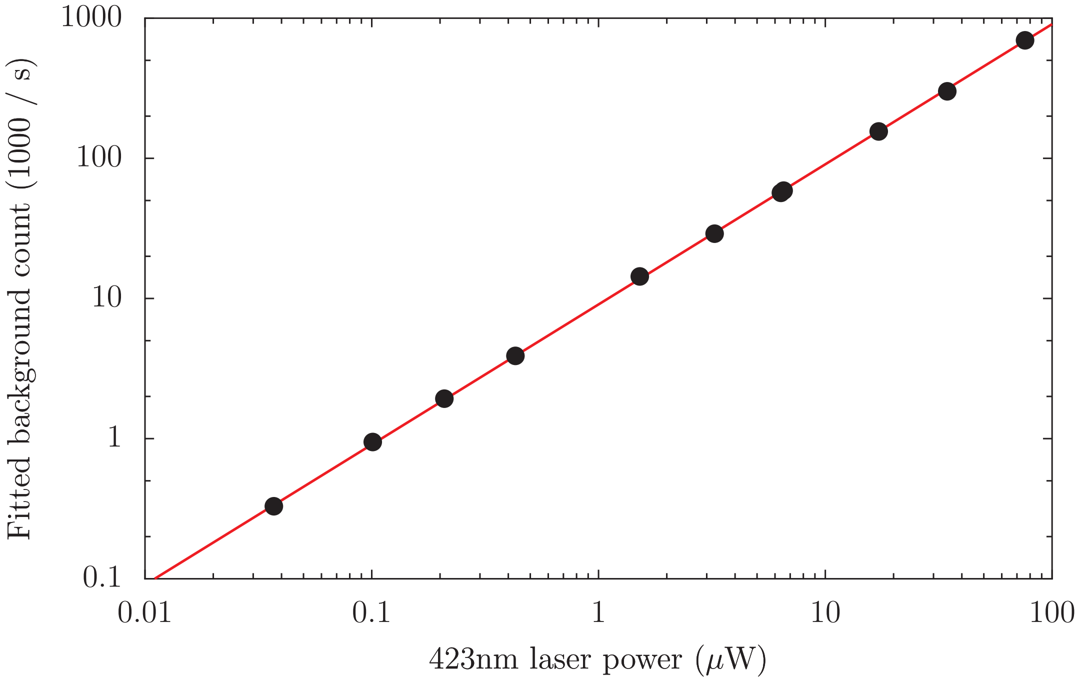

Figure 5.9: Fitted background counts are shown as a function of measured 423 nm laser power. The solid line is a linear fit with zero intercept, with slope of $9.05(6) \times 10^3$counts/ s/ μW.

laser, but at high intensities it was enough to cause irregularities in the laser output. Using lower laser intensities, replacing the fibre with an angle-polished version, or installing an optical isolator in the beampath before the fibre coupler would provide more stable laser operation.

The presence of systematic errors due to laser intensity variations prevents a rigorous statistical analysis of the data, so we proceeded as follows. It was possible to fit the recorded spectra with the parameters w and X kept global, while the atomic number density (thus the parameter K_1) was floated for all scans. An average value of n could then be found. The best fit parameters under these conditions are

$$n = 8(1) \times 10^{11}\,\mathrm{m}^{-3} \Longrightarrow T = 640(5)\,\mathrm{K} \tag{5.30}$$

$$X = T\cos^2\theta = 35(3)\,\mathrm{K} \Longrightarrow \theta = 76.5(1.5)^\circ \tag{5.31}$$

$$w = 22(4)\,\mu\mathrm{m} \tag{5.32}$$

To assess the reliability of the power measurements, the fitted background scatter is

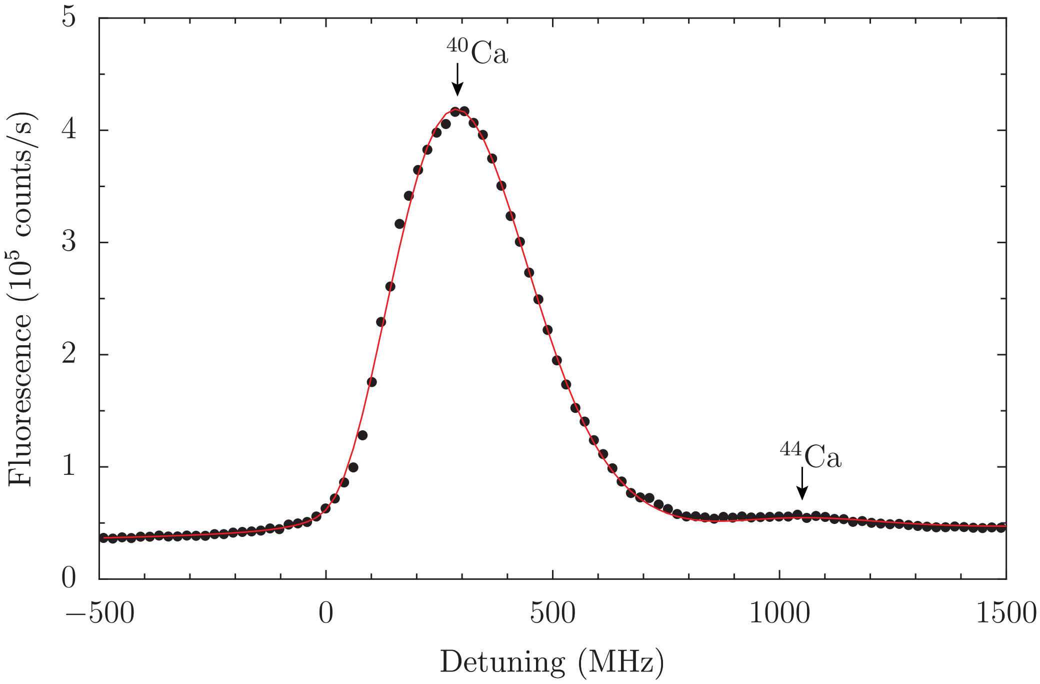

Figure 5.10: Fluorescence signal showing the presence of ^{44}Ca. The oven current was 7 A. The solid line is the fit to the recorded counts, using Equation 5.33.

plotted as a function of the measured laser power (see Figure 5.9). A linear function with zero intercept fits the data points well, and yields $9.05(6) \times 10^3$counts/ s/ μW as the measure of the background.

5.3.3 Oven temperature as a function of oven current

The second experiment is aimed at characterizing the Ca oven. The oven temperature was estimated as a function of the supplied oven drive current. The oven current was adjusted between 5.25 Aand 7 A. At a given oven current fluorescence spectra was monitored while scanning the 423 nm laser frequency. The laser input power was kept constant low value of $P \approx 1\,\mu$W to avoid optical feedback to the laser, as described previously. The fitted values of θ and w are used in the data analysis. The observed fluorescence is then a function of the number density and the temperature of the Ca oven.

One difference compared to the previous fitting procedure is that we observed hints of a fluorescence peak of the ^{44}Ca isotope in the recorded signal when the oven is supplied with high current $(6.5 - 7\,\text{A})$ (see Figure 5.10). Thus the neutral fluorescence spectra was

Parameter	**Fitting type**
K_1	individual
K_2	individual
X	fixed
B	individual
Δ_{offset}	individual
w	fixed

Table 5.3: The list of fitted parameters of the experiment determining the Ca oven temperature as a function of oven current.

fitted as a sum of two fluorescence curves, one for ^{40}Ca and one for ^{44}Ca, shifted by the isotope shift in the 423 nm transition, which is $\Delta_{i,44} = 774\,\text{MHz}$. The ratio of the peak heights was fixed at the natural abundance ratio. The abundances of ^{40}Ca and ^{44}Ca are $a_{40} = 0.969$ and $a_{44} = 0.0209$, respectively.

$$\begin{aligned} S \;=\; & \frac{\pi\eta A\rho n d w^2}{4}\int \ln\left\{1+\frac{I_0(\Delta)A^2/2}{(2\pi\Delta)^2+(A/2)^2}\right\} f(\Delta_D)\mathrm{d}\Delta_D \\ & +\frac{a_{44}}{a_{40}}\frac{\pi\eta A\rho n d w^2}{4}\int \ln\left\{1+\frac{I_0(\Delta)A^2/2}{(2\pi[\Delta-\Delta_{i,44}])^2+(A/2)^2}\right\} f(\Delta_D)\mathrm{d}\Delta_D \\ & +B\frac{I_0(\Delta)}{I_0(0)} \end{aligned} \tag{5.33}$$

where n is the number density of the ^{40}Ca isotope, and Δ is the detuning of the 423 nm laser from the transition in ^{40}Ca. To simplify the fitting procedure, a number of substitutions were made, as in the previous section:

$$K_1 = \frac{\pi\eta A\rho n d w^2}{4}, \tag{5.34}$$

$$I_0(\Delta) = \frac{2}{\pi w^2}(P + K_2\Delta). \tag{5.35}$$

Figure 5.11 shows the estimated oven temperature. It appears that the estimated temperature in the previous experiment is lower for the same oven current. Since the two experiments were about one month apart, and the first was conducted immediately after the first outgassing of the Ca oven, it is conceivable that chemical changes happened during that one month use (such as more complete breakdown of the oxide layer on the surface of Ca), that changed the vapour pressure inside the oven and thus the temperature estimate. Also, the oven temperature experiment can be considered more reliable than the one presented in the previous section. This is because of better signal properties due to higher number densities at high temperature (higher signal/background ratio) and the moderate laser intensity (no optical feedback to the laser).

Figure 5.12 shows the recorded pressure in the vacuum chamber as a function of oven current. At low oven currents when there was enough atomic flux to observe a neutral fluorescence signal, the pressure barely rises above the baseline. Based on the experience of other ion trap groups, ion loading in similar traps requires a pressure of less than 10^{-9} Torr, which is achievable in our system.

The experiments described in this chapter were sufficient to determine the required working parameters for the 423 nm laser and Ca oven, to attempt ion loading in the Sandia trap.

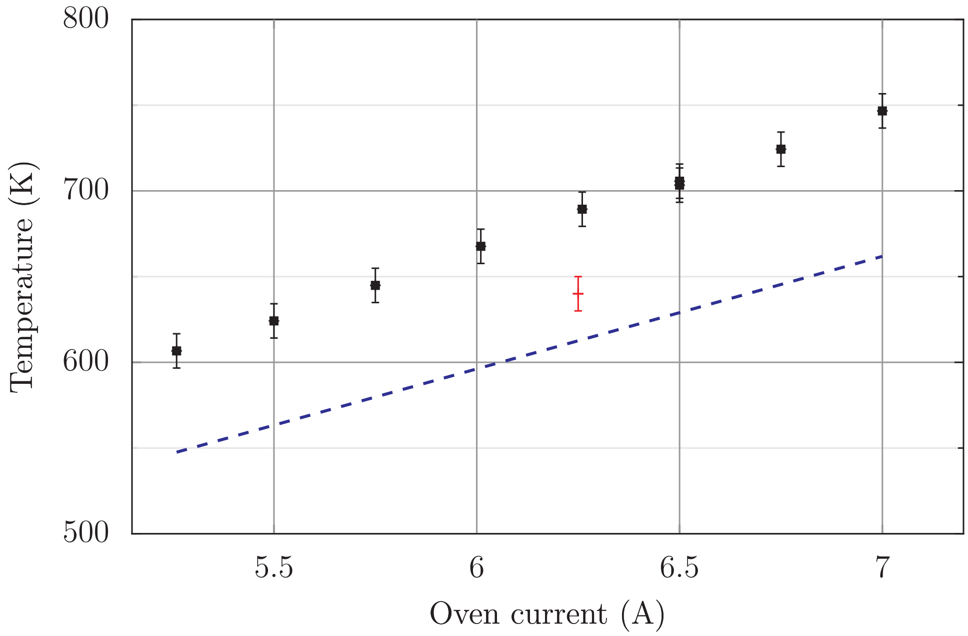

Figure 5.11: Estimated oven temperature as function of the oven current. The dashed line is the pyrometric temperature measurement data of a similarly prepared oven, described in Section 5.1 on page 62. A single point at 6.25 A oven current shows the estimate of the experiments described in Section 5.3.2. (Colour in electronic version)

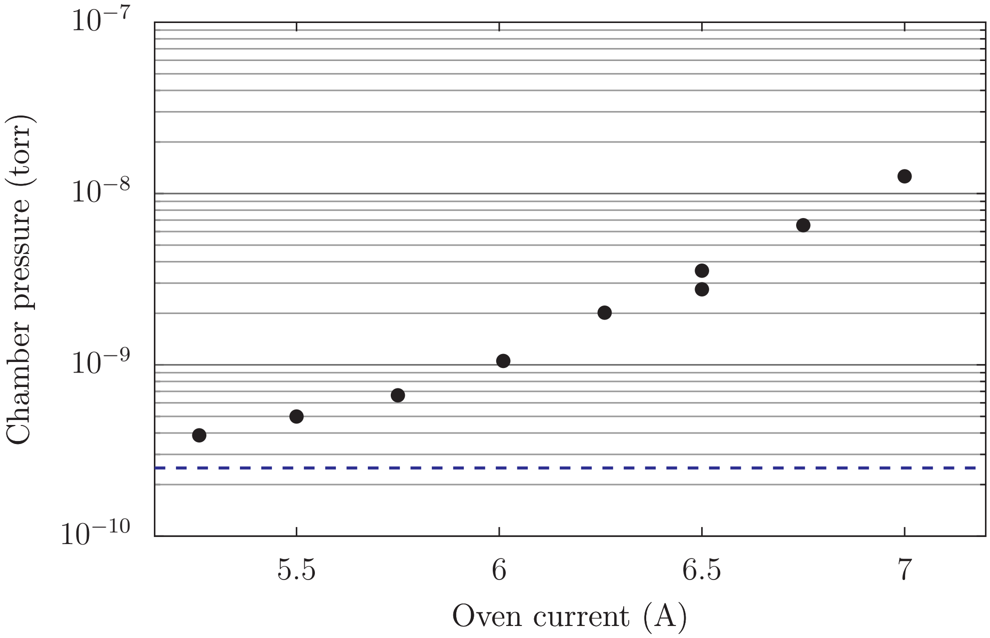

Figure 5.12: Recorded pressure inside the vacuum chamber as a function of the calcium oven current. The dashed line shows the baseline pressure when the Ca is turned off.

Chapter 6

Experiments with the Sandia trap

This chapter and the next summarise the results of experiments with trapped $^{40}\mathrm{Ca}^{+}$ ions in the Sandia trap. The current chapter first describes the photoionisation and trapping. This is followed by accounts of the experiments to measure the trap lifetime and the vibrational frequencies, and trapping of multiple ions. Measurement of the heating rate in the trap and shuttling single ions along the trap axis are presented in Chapter 7.

6.1 Ion loading

In our ion loading scheme, 4 different laser frequencies are used: a 423 nm beam excites the neutral Ca atoms. A 389 nm beam provides further excitation for photoionisation. A pair of beams (397 nm and 866 nm) are used for Doppler-cooling and detection of the ion (see the relevant energy level structure of Ca and Ca^{+} in Figure 1.1).

One difficulty was that before any ions had actually been captured, it was hard to check whether certain parts of the experimental equipment were functioning correctly. The applied DC and RF voltages can be measured only outside the vacuum chamber, so there is no direct method to check the true values of voltages on the electrodes. The laser beams need to be precisely guided through the trapping position of the electromagnetic field, but with no signal the correct position can only be estimated.

It was only with difficulty that the correct working procedure for the Sandia trap was discovered. There was initially a period of 2 months during which all attempts to load ions and detect fluorescence failed. During this period various aspects of the apparatus were honed and improved, but ultimately the failure to trap ions was caused mainly by one oversight. When looking for the possibly weak fluorescence signals associated with the first loading of ions, we adopted the standard practice of using a differential detection scheme, somewhat like 'phase-sensitive detection'. The 866 nm laser was pulsed on and off for periods of 50 ms, and the photomultiplier count signal for each "off" period was substracted from the signal for the neighbouring "on" period. This suppresses noise associated with background scatter and laser intensity fluctuations. However, the combination of collisional heating (from the background gas and the neutral atom beam) and intrinsic electric field noise in the trap meant that trapped ions could not survive in the trap with the Doppler cooling thus switched off for periods of 50 ms. This was exacerbated by a poor choice of DC electrode voltages, before the backplane electrode was accounted for in the numerical model (this poor choice did not make the trap completely unstable, but it reduced the trap depth). Once we optimised the voltages, reduced the atomic beam flux and, most importantly, went over to continuous Doppler cooling, ions were loaded satisfactorily. Then was it possible to adjust the DC voltages for good compensation and thus achieve the most stable trap.

The University of Michigan group experienced severe problems with a trap of the same design and, to our knowledge, either never or only briefly managed to trap ions in it. The NIST group loaded ions in a similar trap but found the trapped ions did not stay in one place, suggesting that the electric field environment was quite unstable owing to surface and materials issues. The University of Innsbruck, Austria group was unable to load ions in a trap of the same design. Their system was different from ours as the trap is mounted much closer to the observation window (dielectric surface) and the pressure in their container was some orders of magnitude higher.

Figure 6.1(a) shows a recorded fluorescence signal as a function of time, during the ion loading. The photoionisation and Doppler-cooling lasers were on. Due to the filters placed in front of the PMT, the recorded signal corresponds only to the observed 397 nm light. All other wavelengths were filtered out. The signal shows very short time intervals when the ion is fluorescing, before it drops to the background level. Initially we interpreted this as the ion escaping from the trap because of collisions with other neutral Ca atoms, or other Ca^+ ions in the trapping region. Collisions with Ca atoms were ruled out because the fluorescence signal became continuous (not dropping back to the background level), when the Ca oven was left on and the photoionisation lasers were blocked after trapping.

The correct mechanism for the observed fluorescence pattern was eventually recognised to be off-resonant excitation of the $S_{1/2}$-$P_{3/2}$ transition by the 389 nm photoionisation beam, which transfers the population to the metastable $D_{5/2}$ state, thus shelving the ion. To eliminate this effect, an 854 nm "deshelving" laser was used. This transfers the ion from the $D_{5/2}$ to the $P_{3/2}$ state, to eventually decay back to the ground state, and enable the Doppler cooling lasers to interact with the ion. The effect of this additional beam is shown in Figure 6.1(b). The Ca oven, the photoionisation and Doppler cooling lasers were used in the same manner as in Figure 6.1(a). With the "deshelving" beam the observed ion lifetimes were comparable to the lifetimes when the photoionisation beams are turned off after ion capture.

This shelving effect of the 389 nm beam is not an issue when loading only a single ion, since one can always block the photoionisation beams. It is very important, however, when loading multiple ions, as described in Section 6.5.

6.2 Micro-motion compensation

Once ion loading is reliable, one can attempt to compensate stray electric fields. Compensation is achieved by adjusting the DC electrode voltages, in order to make the DC potential minimum coincide with the RF potential minimum.

The compensation is usually done in two steps. Initially the fields are very badly compensated and the ion has a large amount of micro-motion. First a rough compensation is attempted and then it is fine-tuned by a correlation method.

In the case of a large amount of micro-motion, the fluorescence spectrum is observed while scanning the 397 nm laser frequency on the red side of the atomic resonance. The electrode voltages are adjusted so as to reduce the observed Doppler broadening [55]. Figure 6.2 shows a pair of scans as an example for a Doppler-broadened and a relatively

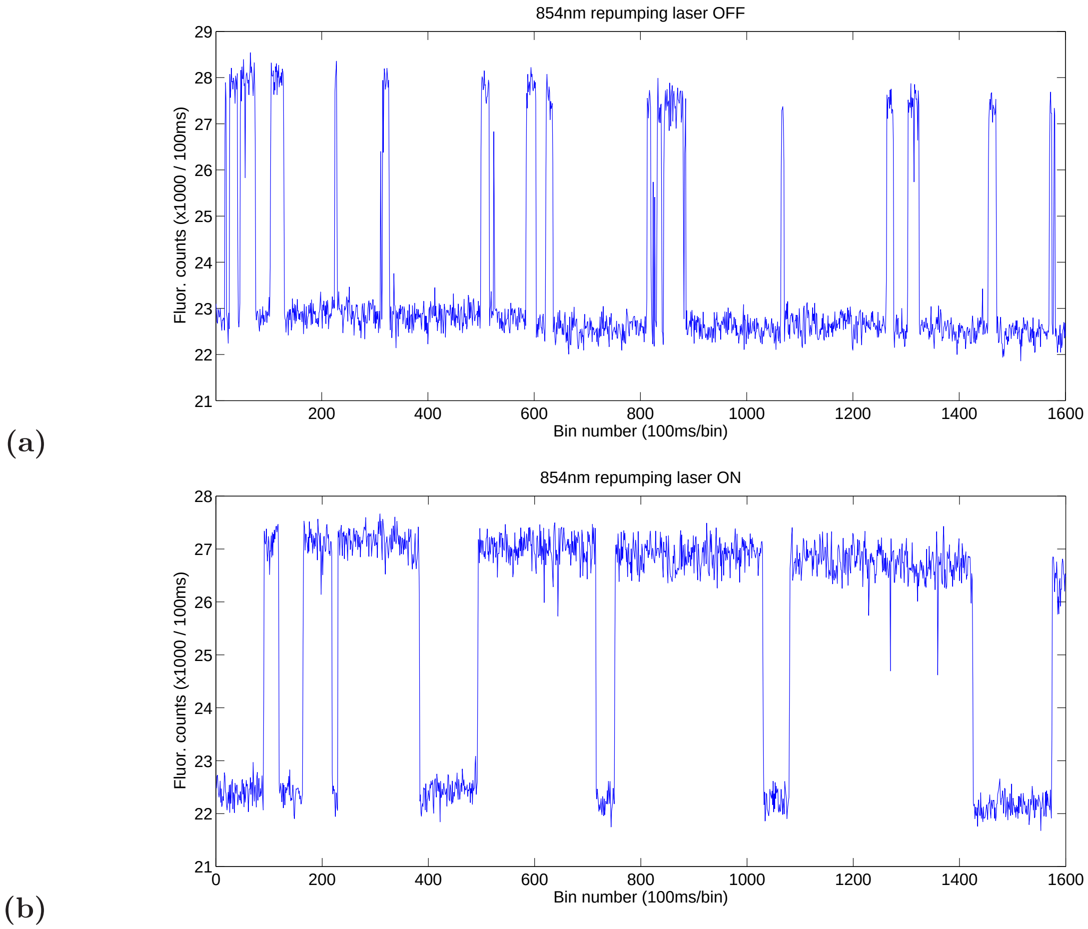

Figure 6.1: Trapped ion fluorescence signal during loading (a) without 854 nm beam b) with the 854 nm beam on. The recorded photon count is plotted as a function of recorded bin number (100 ms per bin). All photoionisation and Doppler-cooling lasers (389 nm, 423 nm, 397 nm, 866 nm) are on continuously on both plots. On (a) there are a large number of quantum jumps present, most of which are attributed to far off-resonant shelving by the 389 nm photoionisation beam (see text). On (b) the number of quantum jumps is reduced due to the deshelving effect of the 854 nm laser beam. The remaining jumps in fluorescence are likely to signal newly captured and then lost ions.

well compensated spectrum.

When trapping the ion in the geometric centre of the trap, most of the time the middle DC electrode pair and the pairs next to them were used (electrode pairs #3, #4 and #5, see Figure 4.2). The horizontal 397 nm Doppler-cooling beam provides information about the micro-motion along the trap axis and out of the plane of the DC electrodes (Z and Y directions, respectively). The compensation in the Z and Y directions is done by adjusting the DC voltage on the #3 and #5 DC electrode pairs relative to the #4 pair. This method

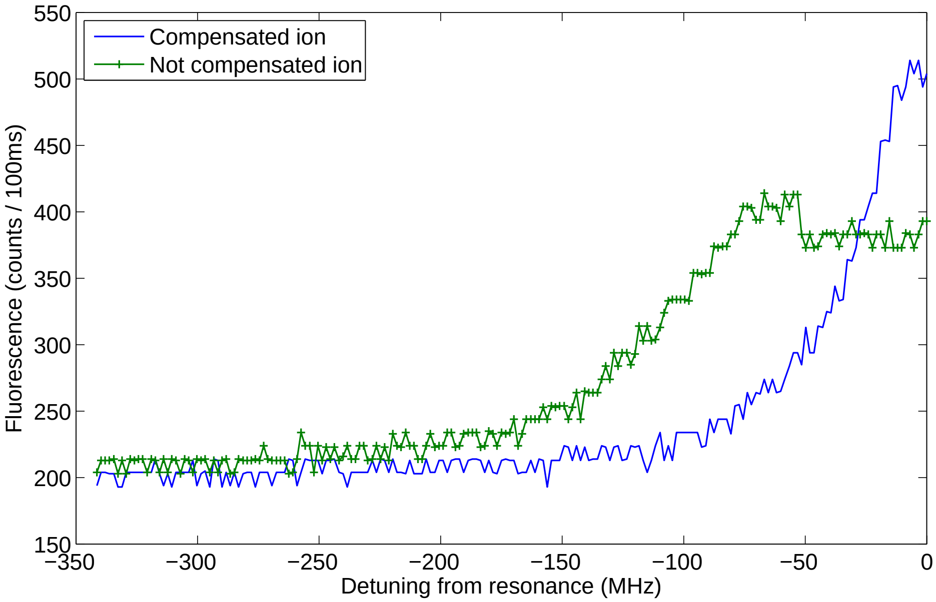

Figure 6.2: A pair of experimental fluorescence spectra showing the Doppler-broadened profile before field compensation and the narrower profile after the crude field compensation described in the text. The photon counts are shown as a function of laser detuning. The detuning is calculated from the calibration shown in Table 4.1. (Colour in electronic version)

will mainly adjust the Y compensation because of symmetry. However, the position of the RF pseudo-potential minimum needs to be matched mostly in the Y direction, because the RF field is much stronger in the Y than in the Z direction. Thus, generally good compensation is achieved by this symmetric adjustment of voltages.

Once the micro-motion is reduced, fine adjustment is achieved by RF-photon correlation [56]. The method is detailed in A. Myerson's first year report [49], and a brief outline is given here.

The 397 nm laser is tuned to the half-fluorescence point on the red side of the atomic transition. The number of fluorescence photons detected is recorded as a function of their arrival time with respect to the RF cycle. In the case of good micro-motion compensation, the photon arrival times are independent of the RF cycle. However, in the case of micro-motion, the photon arrivals have a timing profile following the RF potential's sinusoidal change. Figure 6.3 shows three example plots of under/over-compensated and well compensated photon arrival times. There are two cut-off thresholds on the time axis.

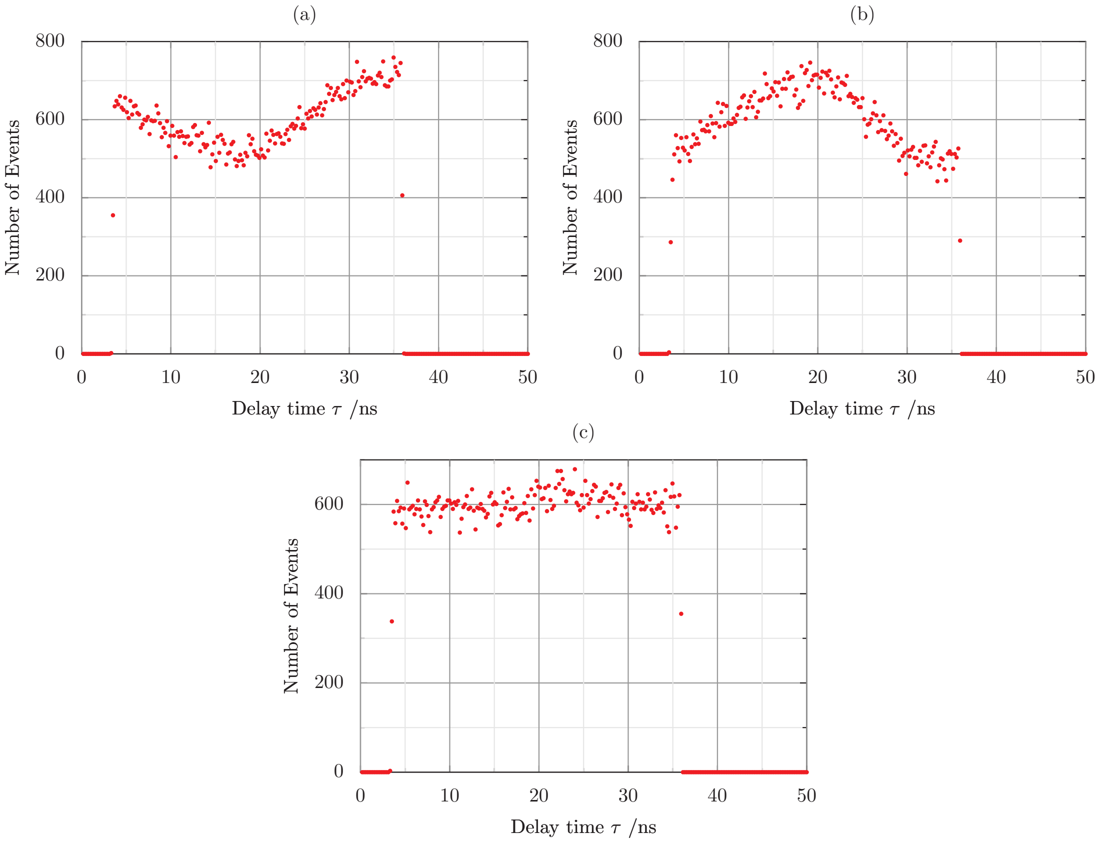

Figure 6.3: Recorded RF-photon compensation signals for different field compensations. The number of recorded photons is shown as a function of time since the beginning of an RF-cycle (delay time). In the case of good field compensation, the photon arrival times are independent of the RF cycle. (a) under-compensated, (b) over-compensated, (c) well compensated. The origin of the cut-off values are discussed in the text. Plot from A. Myerson's first year report [49].

The upper threshold is $\tau = 36.7\,\text{ns}$, which corresponds to one cycle of the RF voltage at $\Omega_{RF} = 2\pi \times 27.25\,\text{MHz}$. The origin of the lower threshold ($\tau = 3.5\,\text{ns}$) is not certain, but is possibly due to the reaction time of the electronics.

To compensate in the X direction (across the trap) a secondary, "vertical" 397 nm beam was used, with a component of its wave vector in the X direction. Thus, after compensating in the Z and Y directions with the horizontal beam, the vertical beam is turned on and the RF-photon correlation is used to check the X-compensation. The compensation is adjusted by putting a voltage difference between the lower and higher set of DC electrodes. This voltage difference was usually of the order of 0.9 V.

With the RF-correlation method, the Z-Y compensation can be set to within ±0.02 V of the optimal value. In the X direction, the compensation can achieve within ±0.05 V of the optimal value. Using the numerical model of the trap, these values correspond to electric field components ±5 V/m in the Y direction and ±20 V/m in the X direction, respectively. The lower sensitivity to micro-motion in the X direction is due to the higher background scatter level of the vertical 397 nm beam.

The field compensation generally changes over time, depending on the environment and the experiments conducted. While improving the field compensation, a number of factors affecting it were identified.

Figure 6.4 shows the effect of ambient light in the laboratory on the field compensation. Turning on the lighting in the laboratory changes the field compensation in an immediate and reversible manner.

A possible source of this effect is the exposed silicon on the face of the chip surface. The doped high resistivity silicon (below a thin $\mathrm{SiO}_x\mathrm{N}_y$ layer) is inherently sensitive to light in the visible range. In practice, it might act as an imperfect photodetector on the chip, where the created electron-hole pairs are not collected, just separated. These electrons and holes can, however, distort the field in the trapping region because of their proximity.

This theory, however, was not tested at the time, as the issue is easily circumvented by turning off the lights during the experiments. The next generation of the Sandia trap design features a gold-plated front face. Comparing the behaviour of the two designs will help our understanding of the effect of the exposed silicon surface on the trap operation.

Figure 6.5 shows the effect of repeated ion loading on the field compensation. After successive ion loads, larger and larger compensation fields were required. On the other hand, long-term ion storage did not change the compensation significantly. The observed behaviour can be explained by charge build-up during the ion loading. This could be due to the photoionisation lasers (especially the 389 nm beam, having the shortest wavelength), or the Ca oven. However, repeated tests failed to show any effects of the laser beams, even when directed onto the electrodes for extended periods. The operation of the Ca oven, on the other hand, noticeably changes the field compensation, even after after a few (3-5) minutes of operation.

The exact nature of the oven's effect has not been identified. One theory was charge

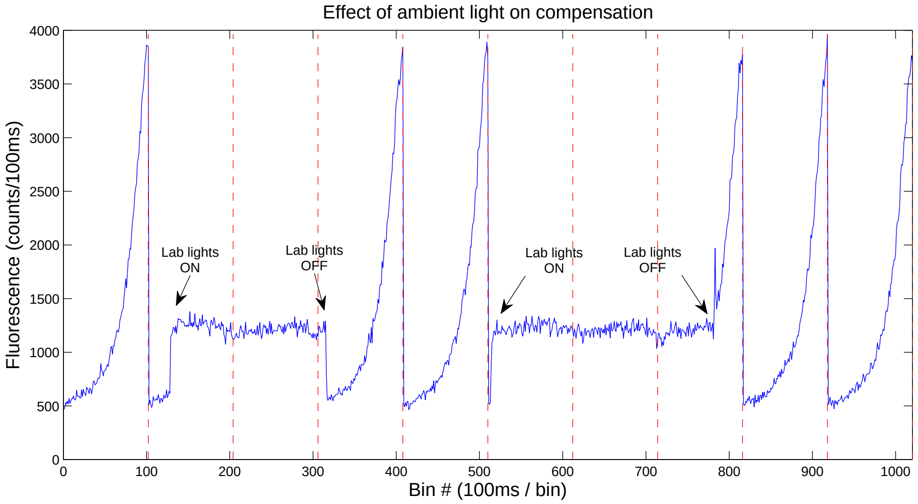

Figure 6.4: Recorded fluorescence signal during repeated scans of the 397nm laser from red detuned to close to resonance with a range of approximately 132 MHz. The ion motion is compensated beforehand. The dashed vertical lines separate the scans. The laboratory ambient lighting was turned on and off during the sequence, as shown on the plot. The signal during those periods has a highly Doppler-broadened profile, and is effectively flat in the scanned frequency region.

building up on the trap due to thermal electron emission of the Ca oven. To eliminate this effect, the oven was biased with a large positive voltage (larger than any voltages on the DC electrodes, of the order of 30 V) with respect to the common ground of the rest of the system. The positive voltage should act as a sink for the thermal electrons, reducing the charge build up, and thus the change in field compensation. This method, however, failed to achieve any observable reduction of stray electric fields, and was abandoned after a trial period of a few weeks.

6.3 Lifetime

In the initial experiments the ion lifetime in the trap was very short, only of the order of tens of seconds even with the cooling lasers on. This was long enough to observe the ions and do basic micro-motion compensation, but unsatisfactory for any more complex experiments. To improve the situation, experiments were conducted to check the effect of different ion loading methods on the ion lifetime.

As qualitative tests failed show any change in the micro-motion compensation caused

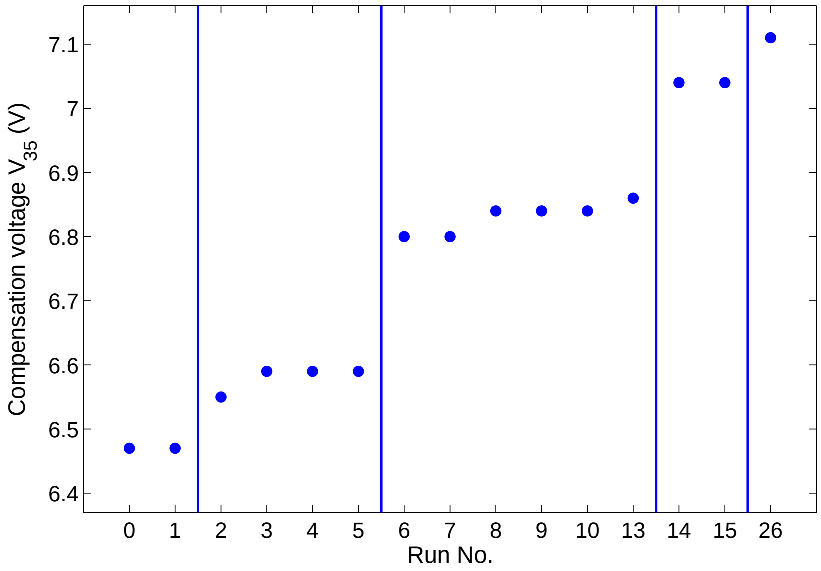

Figure 6.5: Figure showing the changing compensation when reloading. The voltage on the electrode pair #3 and #5 is plotted as a function experiment number. The compensation is checked before every experiment and adjusted if necessary. The vertical lines represent lost ion and reloaded trap. Thus, all experiments between two vertical lines are done with the same ion. The approximate time scale is 3-4 minutes for a compensation check and experimental run, 4-5 minute for loading an ion. It is clear that large changes happen in the compensation when reloading.

by the applied laser beams, the lasers were not considered to be the immediate cause of the short lifetime. The Ca oven, however, had a significant effect on the field compensation (as was shown in the previous section), and it could be a more significant factor in causing instabilities in the trap, leading to the loss of trapped ions.

The results of the experiment are analyzed in terms of an estimated survival function. The survival function is the probability of the ion staying in the trap longer than t:

$$S(t) = P(\tau \geq t) \tag{6.1}$$

where the ion lifetime is τ.

The survival function was estimated using the non-parametric Kaplan-Meier (or product limit) estimator [57]:

$$\hat{S}(t) = \prod_{t_i < t} \frac{n_i - d_i}{n_i} \tag{6.2}$$

where t_i is the ith recorded distinct ion lifetime, n_i is the number of ions with lifetime longer than t_i, and d_i is the number of ions with lifetime equal to t_i. The variance of the Kaplan-Meier estimate of the survival function is calculated as

$$\mathrm{Var}(\hat{S}(t)) = \hat{S}(t)^2 \sum_{t_i<t} \frac{d_i}{n_i(n_i - d_i)} \tag{6.3}$$

which is used to calculate the confidence interval of the estimated half-probability lifetime (the time up to which half the ions survive).

Two sets of tests were conducted, changing different aspects of the ion loading procedure. In the first experiment, the effect of different oven drive currents were tested. Three different currents (5.25 A, 5.5 A, 5.75 A) were used. During the experiment, one of the currents was set, and, when the oven temperature stabilised, ion loading was attempted. Temperature stability was assumed when the electric resistance of the Ca oven stopped changing. Once an ion had been loaded into the trap, the photoionisation beams were blocked, and the fluorescence signal was recorded until the ion was lost. The observation was repeated with a large number of ions. After a certain time (10-15 minutes) a different oven current was set, and the observations repeated. The oven current was changed a large number of times, and the complete data set for each of the oven currents comes from multiple observation sequences. The field compensation was checked at the beginning of the experiment, and was not changed during the observations. The measured ion lifetimes were extracted from the recorded fluorescence signal.

The results of the first experiment are plotted in Figure 6.6 and listed in Table 6.1 (series #1-3). The ions had a longer lifetime in the trap when the Ca oven was operated at a lower temperature (lower drive current). The half-probability lifetime was in the order of 300 s for the low current loading (5.25 A), while it was <100 s for the higher current (5.5 A, 5.75 A) cases. Thus, a lower Ca oven current at the loading improves the ion lifetime.

During these experiments, the photoionisation beams were blocked once an ion was loaded, to stop excess ion creation in the trapping area, but the Ca oven was on during the whole experiment, emitting neutral Ca atoms.

Experimental series	**No. of ions**	**Half-probability lifetime (s)**
#1: $I_{\text{oven}} = 5.25\,\text{A}$	40	362 [225...466]
#2: $I_{\text{oven}} = 5.5\,\text{A}$	53	74 [49...92]
#3: $I_{\text{oven}} = 5.75\,\text{A}$	72	29 [23...56]
#4: $I_{\text{oven}} = 5.25\,\text{A}$	48	289 [190...453]
#5: $I_{\text{oven}} = 5.25\,\text{A}$ - turned down	28	581 [399...905]

Table 6.1: Experimental lifetimes of ions, for different Ca oven currents. The numbers in the square brackets show the 95% confidence interval of the ion lifetime. The different experiments are described in the text.

We now turn to our second experiment, in which we compared two different ion loading methods. The first method maintained the operating oven temperature after an ion had been trapped (as in the previous experiment). In the second method after an ion was trapped, the Ca oven drive current was lowered from 5.25 A to 2 A to stop the emission of Ca vapour. The 2 A current was considered low enough to stop Ca emission, while maintaining an oven temperature that can be raised quickly to the operating temperature.

During the experimental sequence 10-15 minutes long sessions of the two different ion loading methods were alternated. The recorded lifetimes of a given loading method are then combined into a single data set.

In the sessions when the oven is turned down after loading, there was a delay of about 1-2 minutes before loading an ion, because the oven had to heat up. This results in a smaller number of observations (28 ion lifetimes) compared to the "always-on" setting (48 ion lifetimes).

Figure 6.7 shows and Table 6.1 (series #4-5) lists the result for the experiment of turning down/leaving on the Ca oven after trapping an ion. The survival probability is slightly higher in the case when the oven is turned down, though the difference in the lifetimes is smaller than that caused by higher oven currents.

After these experiments we observed even longer average ion lifetimes in the trap than shown in the results above. This can partly be attributed to gaining more experience in operating the trap and performing the field compensation. After a few weeks of operating the trap, we regularly observed ion lifetimes of tens of minutes. The longest observed lifetime is over 2 hours, even while performing different experiments, e.g. probing trap frequencies as described in the following section.

A tentative explanation of all these results is as follows. The lifetimes of order 1 minute observed at oven current 5.5 A is consistent with loss by collisions with atoms and molecules in the background gas, according to the following argument. The studies in Chapter 5 permit us to estimate the oven temperature T = 625 K when the current is 5.5 A (see Figure 5.11). Equations 5.18, 5.21 and 5.22 give the number density of Ca atoms in the atomic beam near the trap region as

$$n_{\rm beam} = 1.9 \times 10^{11}\ {\rm m}^{-3}$$

Meanwhile figure 5.12 shows the pressure at the ion gauge was then approximately 5×10^{-10} Torr. Other studies suggested the ratio between pressure at the trap and pressure at the ion gauge is about 3, so the pressure at the trap could be of order 10^{-9} Torr (the ion gauge is imprecise at measuring Ca pressure). Assuming this gas is at room temperature, it has a number density

$$n_{\rm gas} = \frac{p}{k_B T} \simeq 3.3 \times 10^{13}\,{\rm m}^{-3}$$

The fluorescence scans would show a Gaussian profile if the Ca at the trap were predominantly in the form of a Maxwellian gas rather than a beam, which suggests the background gas is not predominantly Ca, but whatever it is, it can lead to collisional loss.

Collisions between Ca^+ ions and neutral Ca atoms involve various effects, including charge exchange and glancing elastic collisions via the comparatively long-range induced-dipole potential. Preliminary calculations [58] show, for example, that for the $1/r^4$ Ca–Ca^+ interaction potential the Langevin distance is $b_L = 1.6\,\mathrm{nm}$ and $1.3\,\mathrm{nm}$ for incident atoms at 293 K and 625 K respectively. Collisions at an impact parameter below b_L can be expected to eject an ion from the trap. Thus the collisional loss cross section is about 100 times larger than would be implied by a simple hard-sphere model. Values around 1 nm are obtained for N_2 molecules and H_2O molecules. Using this number, the loss rate is estimated as $\pi b_L^2 n \bar{v} = 0.04$, i.e. one per 26 seconds. This is of the order of the observed value.

In later work the background pressure in the trap was substantially lower, and this could be the explanation for the substantially longer lifetimes observed.

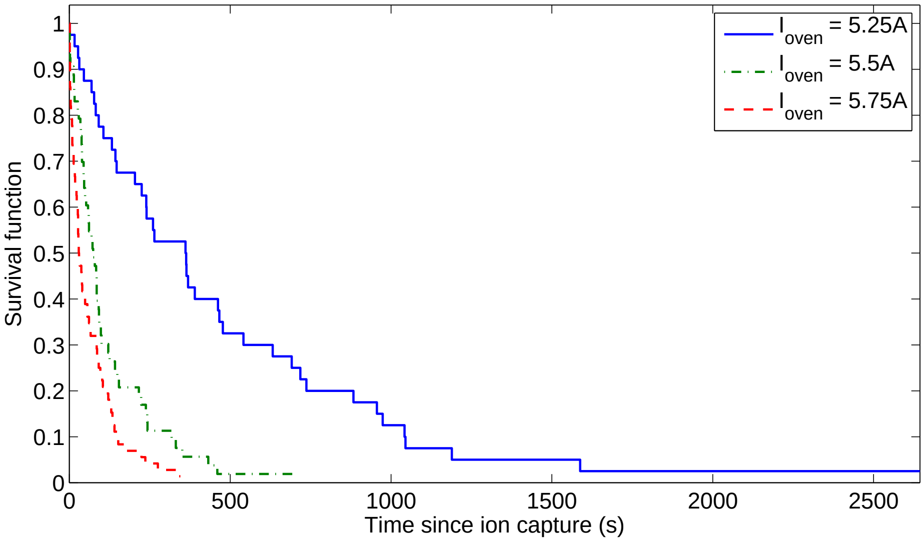

Figure 6.6: The experimental survival function of the ions in the trap, for different oven temperatures while loading. The photoionisation beams were blocked after ion capture, the fluorescence was observed until the ion was lost. High oven drive current (high oven temperature) shortens the ion lifetime. (Colour in electronic version)

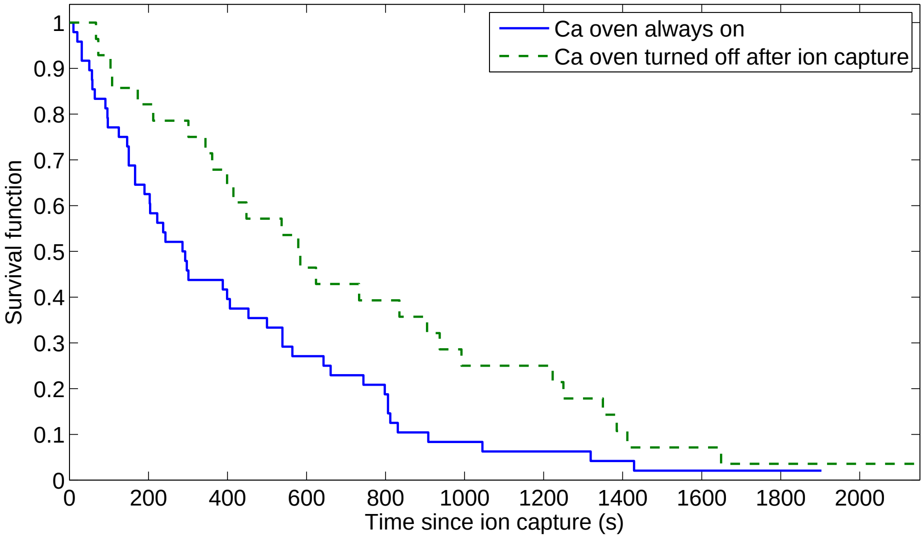

Figure 6.7: The effect of reducing Ca oven drive current after ion capture on the ion lifetime. The survival function is plotted for the two different loading methods. The Ca oven generally cools down in a matter of seconds, and stops emitting Ca vapour, as was verified by pressure measurements. (Colour in electronic version)

6.4 Vibrational frequency measurements

The axial and radial trap frequencies are important parameters, crucial for many experiments with single and multiple ions. Computer simulation of the fields in the ion trap can provide estimates, but our models of the trap have to be validated, by comparing predictions to experimentally observed frequencies.

One uncertainty in the computer models is the trap geometry, since the actual manufacturing process might have deviated from the initial plans. Also, there can be conducting materials in the assembled setup, not accounted for in the plans, and their position is not known with good accuracy. Examples of these are gold-plated surfaces on the back side of the Sandia trap, or the out-of-plane compensation electrode added to the system during the system assembly.

Another uncertainty is the exact value of the applied RF voltage. The RF voltage depends on the Q-value of the helical resonator, which cannot be accurately measured outside the vacuum can. By experimentally determining the radial trap frequencies, the comparison with computer models yields the effective voltage on the RF electrodes. Then the Q-value can be determined since the applied input voltage of the helical resonator is known.

To probe the trap frequencies, an AC “tickle” voltage oscillating at a frequency close to the expected ion vibrational frequencies was applied to some of the DC electrodes. The frequency was scanned, and the fluorescence signal was recorded. When the tickle frequency was in resonance with any of the trap frequencies, the ion’s motion was excited and the fluorescence signal changed.

When the 397 nm laser is tuned close to the atomic transition (for example, to the half-fluorescence point on the red side of the transition), an increase in the ion’s motion will cause a dip in the fluorescence. This dip, however, is quite small compared to the original fluorescence level, because there has to be very large Doppler-broadening of the profile to have a significant drop in fluorescence at such small detuning. Better results are achieved when the 397 nm laser is detuned further from the atomic fluorescence. When stray fields are properly compensated and the laser is tuned to -200 MHz (red detuning), the observed fluorescence is almost at the background scatter level (see Figure 6.2). At such detuning, an increase due to the Doppler-broadening of the spectra will result in a large increase of the fluorescence. Figure 6.8 shows an example of such a tickle scan, when exciting the ion's radial frequencies.

First the axial trap frequencies were probed. The RF voltage is applied to the electrode pair #2, grounded in most of the other experiments. A Tenma Jupiter 2010 2 MHz function generator was used to provide 8 Vpp on its 50 Ω output, to excite the ion's axial motion. The frequency of the function generator was controlled by the experimental control computer via the function generator's DC input. The frequency was scanned linearly, with good repeatability.

Results of the scans, showing the axial trap frequency as a function of applied DC electrode voltages, are plotted in Figure 6.9. Trap frequency predictions from computer simulations are also shown. The predicted frequencies have a similar DC electrode voltage dependence to the experimental values, but they are about 10% lower. This discrepancy is probably due to the imperfection of the computer model of the trap, as discussed in Section 2.4.

To measure the radial trap frequencies a new signal generator was needed, as the frequencies were expected to be higher than the 2 MHz limit of the Tenma Jupiter 2010. An Agilent 33220A 20 MHz arbitrary waveform generator (AWG) was used, and the output of the function generator was connected to the extra compensation electrode (see hardware description in Section 4.1.2). The applied RF voltage was a sine wave function, with 250 mVpeak-to-peak. The frequency scan was pre-programmed in the AWG, and the scanning was triggered by the experimental computer. Then the timing (bin number) of the recorded fluorescence contains the relevant frequency information.

When using the "horizontal" 397 nm laser beam, the motion is observed only in the Y direction; while using both the "horizontal" and the "vertical" beams, both peaks corresponding to the X and the Y radial frequencies are present in the scans. Scans using only the "horizontal" beam have better signal-to-noise ratio due to the smaller amount of background scatter. Thus the first scans to roughly locate the radial frequencies were done using the "horizontal" beam only. Once the correct region had been found, both beams were turned on to measure the two radial frequencies in a single run.

Figure 6.10 shows the combined results of the tickle scans of the radial frequencies, as a function of the RF drive voltage. The best fitting simulation results are also plotted. The fitting is done adjusting a single parameter, the Q-value of the helical resonator, to get the amplitude of the RF voltage on the RF rails from the drive voltage. The fit gives Q-value of 21, which is very close to the expected Q-value of 20 (by measuring the voltage just outside the vacuum chamber after the resonator).

The radial frequency in the X direction can be fitted much better than that in the Y direction. The discrepancy between the measured and simulated values is probably due to the incomplete knowledge of the shape of slot's sides, whose gold coating provides a large grounded DC electrode. Nevertheless, as in the case of the axial trap frequency, the predicted and measured frequencies are largely consistent.

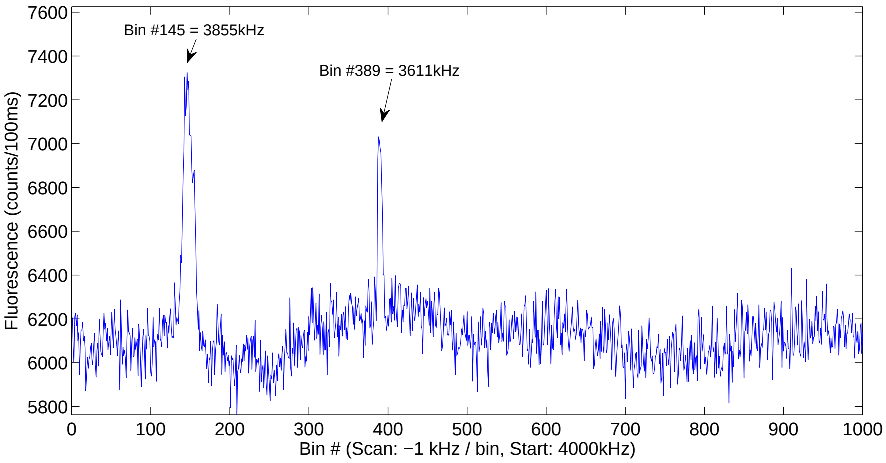

Figure 6.8: Example of scan in the tickle experiment to determine the radial trapping frequencies. The fluorescence is recorded as a function of the tickle frequency. The experiment was done having both "horizontal" and "vertical" 397 nm beams on. When the "vertical" beam was turned off, only a single peak was observed (at the higher frequency of the two), determining which peak corresponds to the X and Y direction, since the "horizontal" beam alone is only sensitive to the ion's motion in the Y radial direction. The peak's position is determined with precision ±15 kHz. ($V_{RF} = 8$Vpp)

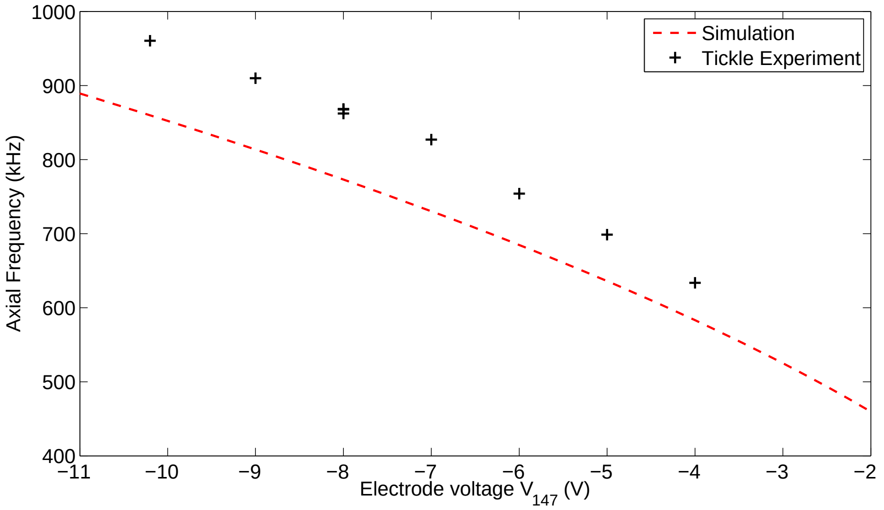

Figure 6.9: Measured axial frequency as a function of voltage on DC electrode pairs #1,#4 and #7, while the other DC electrode voltages and the RF amplitude were kept constant. The measured frequencies are compared to simulation results. The simulation reproduces the correct shape of voltage dependence, but not the correct values. The discrepancy is probably mostly due to uncertainty in the exact geometry, particularly the placement of the electrodes and the gold-plated back plane.

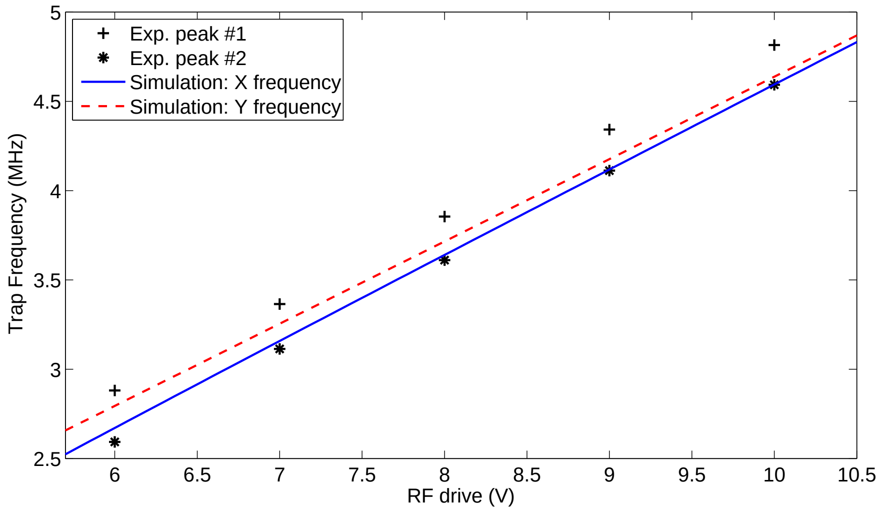

Figure 6.10: Measured radial trap frequencies as a function of RF drive voltages, compared to simulated values. The simulated trap frequencies are fitted to the measurements to infer the Q-value of the helical resonator (the conversion factor between the RF drive voltage and the peak-to-peak RF amplitude on the electrodes). According to the fit, the Q-value is 21, which is close to the expected value of 20. The discrepancy between the fitted and measured trap frequencies is probably mostly due to uncertainty in the exact geometry of the trap.

6.5 Loading multiple ions

In practice one wants to be able to store multiple ions in the same trapping region, so that they can interact with each other. In most quantum computing schemes it is sufficient to store a pair of ions in a single trapping region, as all quantum algorithms can be implemented using single-qubit and two-qubit quantum gates.

We experimented with multiple ion loading in the Sandia trap with partial success. During normal single ion loading as described earlier in this chapter, when the 854 nm deshelving beam was used, multiple ions were loaded into the trap occasionally, but their occurrence was unpredictable and had a very short lifetime. A recorded fluorescence signal of such multiple loading is shown in Figure 6.11.

In controlled multiple ion loading experiments some changes were made to the trapping fields that were believed to improve the loading success rate and/or multiple ion lifetime. The RF supply voltage was lowered from the usual 8 Vpp ($\sim$ 84 V amplitude on the RF electrodes) to 6 Vpp ($\sim$ 63 V amplitude on the RF electrodes) or lower. This corresponds to radial trapping frequencies of 3 MHz or lower. The DC voltages were also changed to provide a lower axial trapping frequency (from the usual 800-900 kHz to 300-500 kHz). The lowest trap frequencies were used when we attempted to optically resolve the multiple ions. The measurement of the ions' separation as a function of the electrode voltages can further validate the simulation model of the trap.

Using lower trap frequencies, pairs of ions were loaded repeatedly, with reasonable reproducibility. The loading rate was of the order of a pair every 3-4 minutes. However, the pair lifetime was very short. While by this time in our experiments single ions were kept for more than 2 hours, the longest observed pair lifetime was $\sim$2 minutes.

This short lifetime was sufficient, however, to take a series of pictures of the ions with a CCD camera and calculate their separation, see Figure 6.12. The results are in reasonable agreement with the expected values from the simulation of the trap.

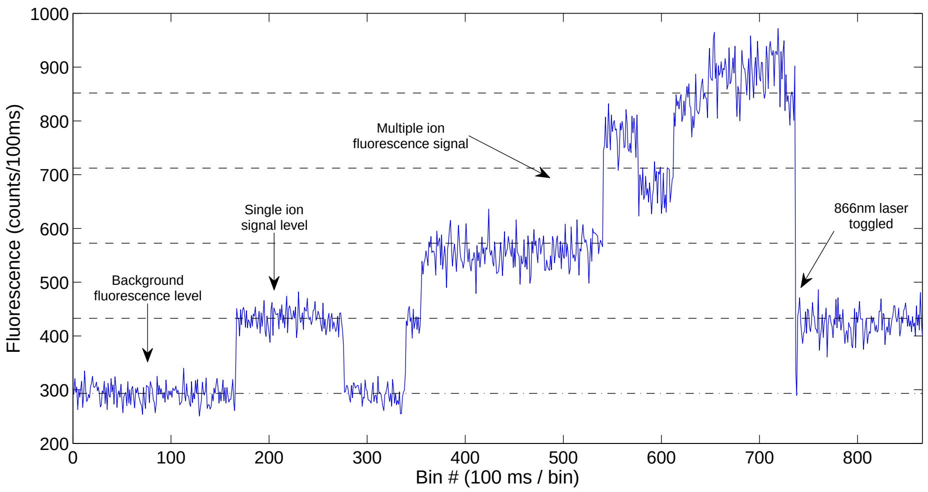

Figure 6.11: Fluorescence signal during ion loading. First a single ion is loaded. The Ca oven, photoionisation lasers and 854nm re-pumping laser were left on. The signal shows a quantum jump-like behaviour, suggesting that multiple ions were trapped. Then the 866nm laser was toggled on/off quickly, which turns off the Doppler cooling of the ions for a short period of time. On the plot the *dash-dotted* line represents the approximate background count level, while the *dashed* lines show the approximate 1,2,3,4 ion signal levels, based on the single ion signal.

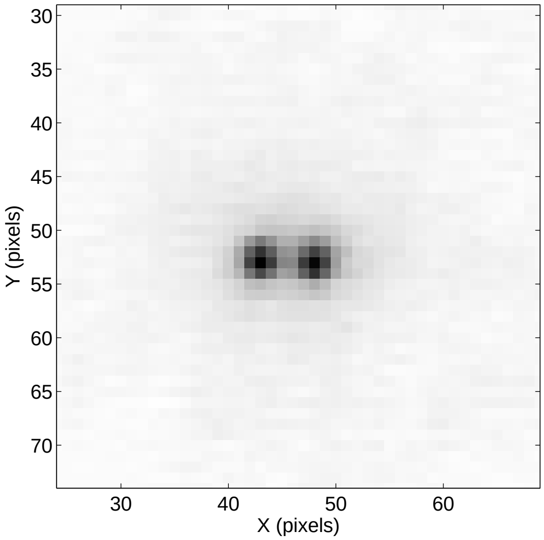

Figure 6.12: Picture of a pair of ions in the trap. Averaged over 12 pictures, taken with the EEV intensified CCD camera. Axial trap frequency $\sim 317\,\mathrm{kHz}$, Radial frequency $\sim 2.7\,\mathrm{MHz}$ ($V_{RF} = 6\,\mathrm{V}$ peak-to-peak), length-scale of pictures: $15.3\,\mu\mathrm{m}/$ pixel. With the imaging system's 8x magnification taken into account, the ions have a separation of $\sim 9.6\,\mu\mathrm{m}$.

Chapter 7

Heating rate and ion shuttle

This chapter describes two studies. The first is to characterize the optical system at the trap, leading to experiments measuring the heating rate of the Sandia trap. The second involves experiments of shuttling the ion along the trap axis, to prepare the ground for multiple ion manipulation.

7.1 Optical system characterization

To interpret the heating rate experiments presented in the next section, a number of parameters of the experimental setup had to be measured. These parameters characterize the laser beams (laser intensity calibration, polarization angle and linewidth for both 397 nm and 866 nm laser beams), the imaging system (optical detection efficiency, PMT dark counts), and magnetic field coil (magnetic field). In this section the measurements of these parameters are discussed.

We are able to measure beam power with the use of a photodiode or powermeter, and for laser intensity calibration we have to know the spotsize of the laser beam at the position of the ion. If the Gaussian beam spot sizes are measured (w_H and w_V for the horizontal and vertical direction, respectively), the laser intensity at the beam centre is

$$I = \frac{\pi}{2 w_H w_V} P \tag{7.1}$$

where P is the power. To estimate the laser intensity at the ion, an optical set-up similar to that illuminating the ion was used, but with a CCD camera at the ion's position. This allowed the beam profile to be measured directly. Our aim was to maximize the available 397 nm beam intensity. The measured spotsize for the 397 nm beam at its focal point (the ion's expected position) in our optical setup was

$$w_H w_V = 87\,\mu\text{m} \times 25\,\mu\text{m} = 2175\,\mu\text{m}^2. \tag{7.2}$$

The 866 nm beam was not measured this way.

The laser linewidth is considered to be of the order of 1 MHz for both beams, based on knowledge of the same types of laser used in another experiment. The polarization angle to the magnetic field is set by a PBS cube and a $\lambda/2$ plate in each beam's path.

The calculation of the estimated optical detection efficiency is shown in Table 4.2 on page 58, and has the result of $\eta = 0.16(3)\%$. The PMT dark count rate was measured to be of the order of 25 Hz[49]. The magnetic field generated by the field coil as a function of drive current was measured using a hand-held gauss-meter to be approximately 10 G/ A.

All of the aforementioned parameters can also be deduced from fitting theoretical curves calculated using Bloch equations to experimentally recorded fluorescence spectra. Checking the numbers in this way is particularly important because in practice all our experiments are of this type and we must be satisfied that we can interpret the data reliably.

The experiment was conducted as follows. A single ion was loaded into the trap. Micromotion compensation was performed using the RF-photon correlation as described earlier. Using the Doppler-cooling beams (397 nm and 866 nm), the 397 nm laser detuning was then scanned from red to blue detuning over the resonance of the transition and the fluorescence was recorded (see Figure 7.2). When the 397nm laser is blue detuned, the ion is heated instead of cooled, and quickly gains enough energy to leave the trap. Thus the fluorescence on the blue side of the transition drops to the background level and the ion is lost. This background level is also recorded for the given laser power. A new ion is loaded, and the whole procedure repeated at a different laser power. During this experiment the 866 nm laser power and detuning, the magnetic field and the polarization angle of the laser beams were nominally kept at a constant value.

The recorded spectra were fitted with theoretical fluorescence profiles calculated using Bloch-equations including the effect of micromotion. Table 7.1 lists the fitted experimental parameters. Certain parameters had fixed values for all the scans (denoted as "Constant" in Table 7.1) such as the laser beam polarization angle and the laser linewidth. The background count was measured for every scan and thus been fixed for the fit.

To reduce the number of variables, some of the parameters were used as a single variable for all different laser powers (denoted as "Joint fit"). These included 866 nm laser power, the magnetic field, the optical detection efficiency. Before every scan, the micromotion was compensated, thus the micromotion maximum velocity (as a parameter describing the residual micromotion after the compensation) can be assumed to be the same in every scan. The inclusion of micromotion had the largest effect on the fits of the lowest laser intensities, but appeared to improve the fits in general.

The 397 nm laser intensity is also listed as one of the "Joint fit" parameters. To explain this, Figure 7.1 shows the measured background counts as a function of laser power. The background scatter is proportional to the laser intensity in the area of the ion and it shows very good proportionality to the measured powers. It is then justifiable to fix the intensities of the different scans in relation to each other using their measured background scatter (above the dark counts of zero laser power). We then have a single scaling factor describing the laser powers for all the scans, given their background counts. Thus the unit of fitted laser intensity is $I_S/bg =$ "397 nm saturation intensity / background count above dark counts in 100 ms measurement", where the saturation intensity is defined as in Equation 5.2. The 397 nm resonance position and 866 nm laser detuning were floated as they were noticed to change on a time scale of order minutes in previous experiments.

This arrangement resulted in 37 fitting parameters for the 16 recorded scans. An example of a fitted fluorescence profile is shown in Figure 7.2. The part of the recorded fluorescence used to determine the background counts is truncated in the figure. The background was averaged over ≈300 points (100 ms/point) in each scan. The residuals from the best fit are also plotted.

In Figure 7.3 the maximum fluorescence points are plotted as a function of measured

Parameter	**Constant**	**Joint fit**	**Individual fit**
397nm laser intensity, I_{397}		$0.0172 I_{S,397}/bg$	
397nm resonance position, Δ_{397}			X
866nm laser intensity, I_{866}		$295 I_{S,866}$	
866nm laser detuning, Δ_{866}			X
397nm laser linewidth, g_{397}	1 MHz		
866nm laser linewidth, g_{866}	1 MHz		
397nm laser polarization angle, ϕ_{397}	$\pi/4$		
866nm laser polarization angle, ϕ_{866}	$\pi/2$		
Magnetic field, B		3.6 G	
Micromotion maximum velocity, v_{max}		6 m/s	
Optical detection efficiency, η		0.155%	
Background count, bg	measured		

Table 7.1: List of parameters in the fit of the recorded fluorescence spectra. Parameters noted as "constant" are set the same for all different spectra. "Joint" fit parameters are fitted as single variables for all spectra. "Individual" fit parameters are fitted separately for all spectra. Fitted parameter values are shown for "Joint" fit. Background counts are measured for every scan. The unit of 397 nm laser intensity is $I_{S,397}/bg$ = "397 nm saturation intensity / background count over dark counts in 100 ms measurement" (see text). The unit of 866nm laser intensity the 866 nm saturation intensity $I_{S,866}$. The saturation intensities are defined in Equation 5.2.

laser power. The points are scattered because of the different 866 nm laser detunings of the scans. The 866 nm laser detuning was stable to approximately ±4 MHz, which is generally not a problem. For illustration, a trend is plotted when a single common 866nm laser detuning (the average of the fitted values) is assumed and all other fitted parameters were kept the same.

The 397 nm resonance position was also stable to about ±4 MHz which is sufficient for our purposes. However, the resonance position appears to have an approx. 28 minutes periodicity, see Figure 7.4. This periodicity is close to the observed period of the air-conditioning system. The likely cause of this is temperature change in the piezo driver that was used to scan the laser frequency by the locking cavity. The piezo driver was placed on an area of airflow and its temperature is likely to be affected by the on/off cycle of the air-conditioning. This effect was discovered only during the data analysis, and does not have a substantial effect on the results.

Using the fitted laser intensities and the laser power at the position of the ion, the 397 nm beam spot-size can be determined. The laser power during the scans was measured after the beam leaves the vacuum chamber, and goes through an IR mirror and an IR filter. To be able to relate the measured laser power to the power in the trapping region, measurements were made for a number of powers at two alternative positions along the beampath: before entering the vacuum chamber, and immediately after leaving it. Table 7.2 summarizes the results of relative powers at the different positions. The power measured after the vacuum chamber is a factor of 0.615 lower than the one measured before the input window. Taking the average between the powers before and after the vacuum chamber, the relative laser power at the ion's position can be estimated as 0.96, thus the conversion factor from measured laser power to power at the ion is $\frac{0.96}{0.615}$.

The laser intensity is calculated from the laser power as

$$I_{397} = \frac{\pi}{2 w_H w_V} P_{397,\text{ion}} = \frac{\pi}{2 w_H w_V} \frac{0.96}{0.615} P_{397,\text{measured}} \tag{7.3}$$

where $P_{397,\text{measured}}$ and $P_{397,\text{ion}}$ are the measured laser power and estimated power power at the ion's position, respectively, w_H,w_V are horizontal and vertical beam parameters, and their product is estimated by the fitting procedure. The fluorescence fit and laser power measurement yields

$$w_H w_V = 2156\,\mu\text{m}^2 \tag{7.4}$$

which is close to the measured value $w_H w_V = 2175\,\mu\text{m}^2$; thus, the beam is likely to be focused to at the ion's position with good precision.

The beam size of the 866 nm beam can be similarly estimated from the fitted intensity and measured power. In the case of the 866 nm beam the power was measured only before the vacuum chamber and the 0.96 factor obtained previously is used to extrapolate to the position of the ion. The measured laser power $P_{866,\text{measured}} = 1.96\,\text{mW}$. Using a similar expression to Equation 7.3 we obtain

$$w_H w_V = 46900\,\mu\text{m}^2. \tag{7.5}$$

The magnetic field coil was operated at $I_{coil} = 379\,\text{mA}$, thus the fitted magnetic field of 3.6 G is in reasonable agreement with the expected value of 3.79 G. The maximum ion

Power measurement position	**Relative power**
Before input window	1
After output before mirror/filter	0.92
After output window and mirror/filter	0.615

Table 7.2: Laser power of the 397 nm beam measured at different positions along the beam path.

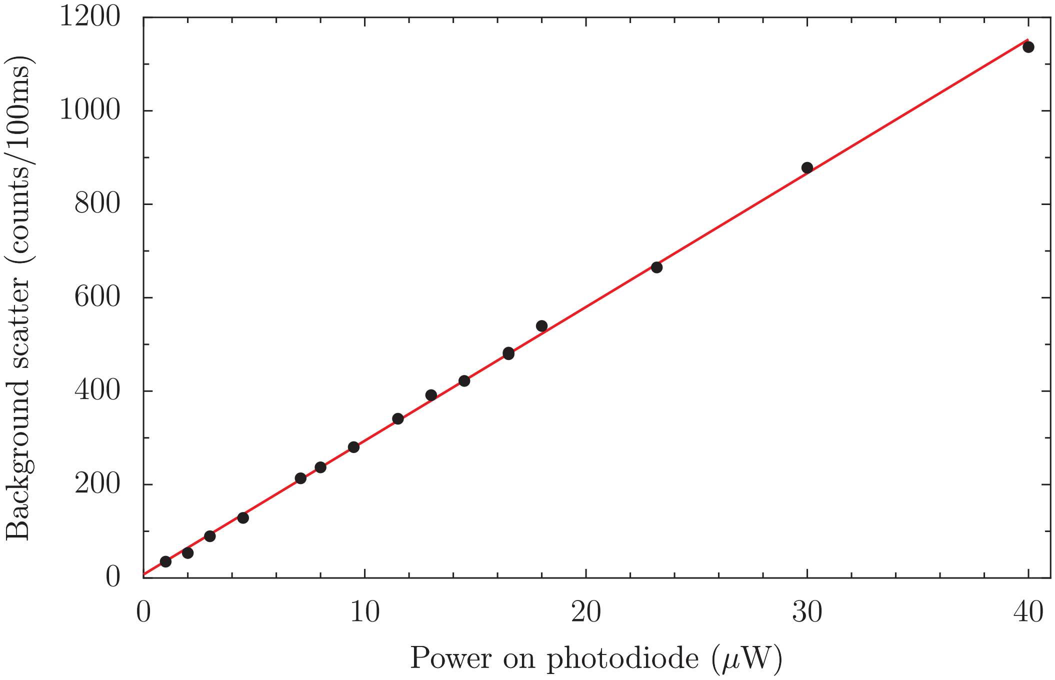

Figure 7.1: Measured background count rate as a function of measured laser power on the photodiode. The intercept of the fit (7.6 counts) provides an estimate of the dark counts of the PMT.

velocity of the micromotion is fitted as $v_{max} = 6\,\mathrm{m/s}$. In case of optimal cooling, the ion's motion is entirely due to the effect of the RF field oscillating at $\Omega_{RF} = 2\pi \times 27.25\,\mathrm{MHz}$. Taking the 45° viewing angle into account, the v_{max} corresponds to an oscillation with amplitude $A \approx 50\,\mathrm{nm}$. The detection efficiency was fitted as 0.155%, in agreement with the calculated 0.16(3)%.

The fact that the experimental parameters derived from the fits are consistent with the results of separate measurements gives confidence in the general approach.

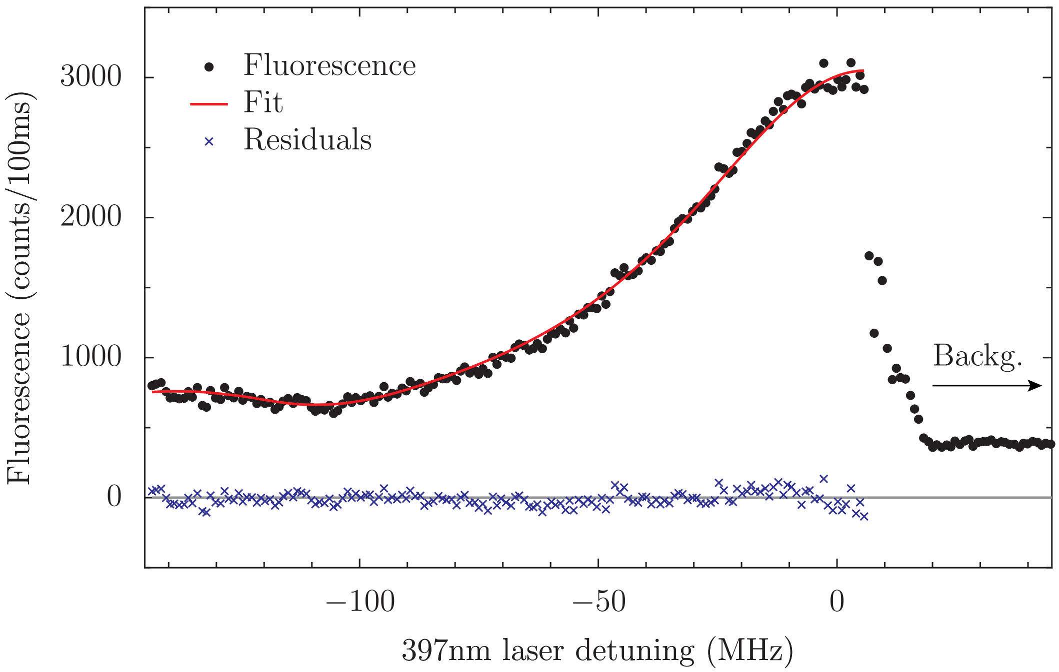

Figure 7.2: Example of fitted saturation profile. Laser parameters are $I_{397} = 6.39 I_{S,397}$, $I_{866} = 294.9 I_{S,866}$, $\Delta_{866} = -119.6$ MHz. Other fitting parameters are listed in Table 7.1. The measured power on the photodiode was 13 μW. The dropout on the blue side of the resonance is due to heating effects. The fluorescence for 397 nm laser detunings between 20 MHz and 40 MHz are considered to be only the background, as subsequent scans show the ion was lost. The background level is estimated from a total of 300 points.

7.2 Heating Rate

The scope of what can be achieved with a given ion trap depends on the motional heating rate of trapped ions. For reliable large scale operation, low heating rates are desired, since high heating rates potentially limit ion lifetimes and length of quantum logic gate operations, as well as requiring more elaborate cooling and error correction schemes.

The relatively short ion lifetime in the absence of laser cooling in the Sandia trap suggested a large motional heating rate. To quantify this observation a method recently developed by the NIST Ion Trap Group was used [59]. The method is based on time-resolved measurement of ion fluorescence during Doppler cooling; it was chosen because it is capable of measuring high ion temperatures and required no additional equipment besides the two Doppler-cooling lasers and fast PMT already being used.

An outline of the temperature measurement procedure is as follows. The Doppler-cooling is turned off for a certain amount of time (delay time, τ_d), by turning off either of

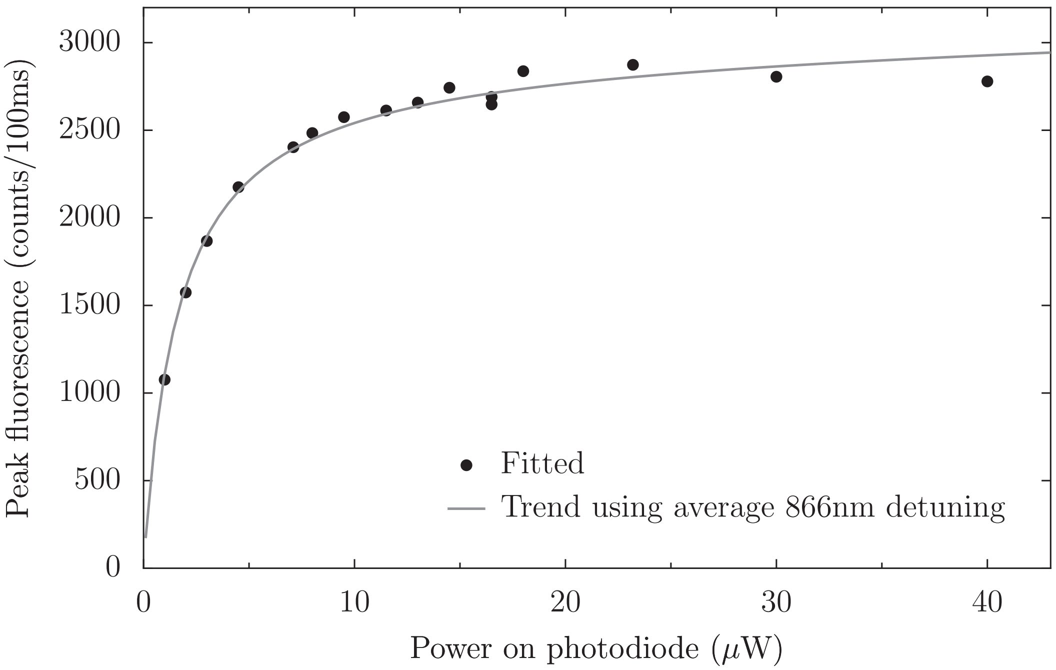

Figure 7.3: Fitted peak fluorescence counts as a function of power on the photodiode. To show the general trend, the solid line is drawn using the mean of the fitted 866 nm laser detunings for all different 397 nm laser powers.

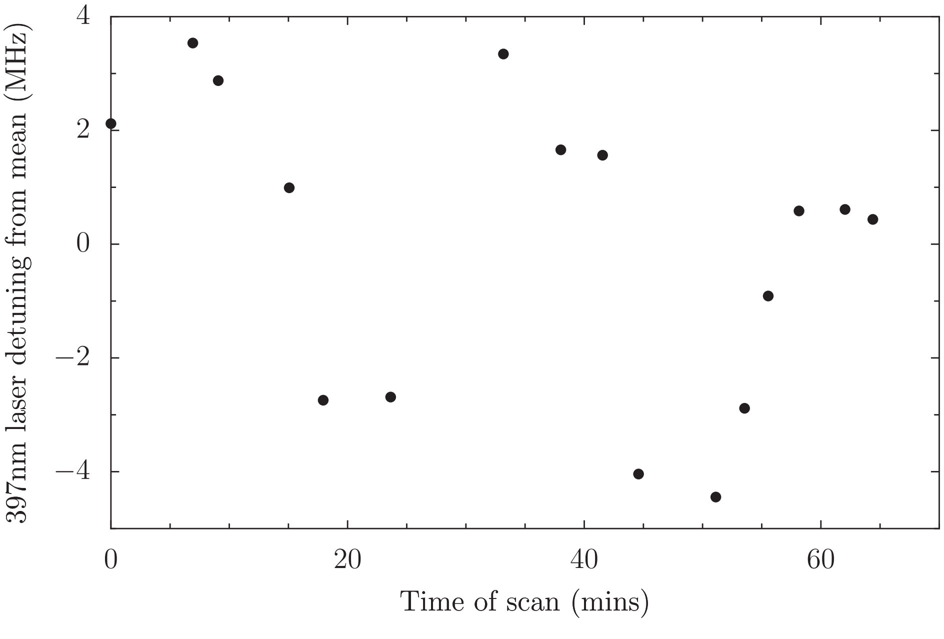

Figure 7.4: Change of the 397 nm laser frequency tuning as a function of time, shown as detuning from the mean value. The change in frequency is deduced from the fitted atomic resonance position. The change appears to be periodic, with a ≈ 28 min period, similar to a cycle of the air-conditioning system.

the two laser beams. When the Doppler-cooling is turned back on, the ion's fluorescence is recorded with fine time-resolution. The process is repeated a large number of times. The fluorescence as a function of time since the start of Doppler-cooling is fitted by a theoretical curve. In the simplest description, when the ion is assumed to have 1D motion and all laser parameters are known, the theoretical curve is described by a single parameter, the average temperature of the ion at the start of Doppler-cooling.

This method has been used by the NIST group to measure the motional heating rate of ^{25}Mg$^+$ ions in a microfabricated trap [60]. One significant difference in the case of ^{40}Ca$^+$ is that it has a Λ level structure (we used the S$_{1/2}$-P$_{1/2}$-D$_{3/2}$ levels, see Figure 1.1), as opposed to the single cycling transition used in ^{25}Mg$^+$. The ion experiences two different Doppler-shifts of the two lasers used for cooling, and requires fully numerical treatment, while the cycling transition has a good analytical description in the low laser saturation limit.

7.2.1 Theoretical description

The description of the ion's motion in 1D is as follows. The ion is assumed to be in the weak-binding regime in the z direction, when the ion's motional frequency ω_z is much smaller than the excited state decay rate Γ. Thus the level populations are approximately in steady state, for any given value of the instantaneous effective detuning

$$\Delta_{\text{eff}} = \Delta + \Delta_D \tag{7.6}$$

where Δ is the laser's detuning from the resonance, and $\Delta_D = -k_z v_z$, where v_z and k_z are the components of the velocity and the wave vector in the z direction.

The population $\rho_{22}(v_z)$ of the P$_{1/2}$ excited state is then calculated by solving the Bloch equations, taking into account the effective detunings of the two Doppler-cooling lasers at different ion velocities (see Figure 7.5).

Then the scattering rate is

$$\frac{\mathrm{d}N}{\mathrm{d}t} = \Gamma \rho_{22}(v_z) \tag{7.7}$$

and the velocity-dependent force experienced by the ion is

$$F_z(v_z) = m\frac{\mathrm{d}v_z}{\mathrm{d}t} = \hbar k_z \Gamma \rho_{22}(v_z). \tag{7.8}$$

The change in the ion's energy E due to this velocity dependent force is averaged over one motional cycle:

$$\frac{\mathrm{d}E}{\mathrm{d}t} = \langle v_z F_z(v_z) \rangle \tag{7.9}$$

(see Figure 7.5 and 7.6). In the averaging the probability distribution of velocities is assumed to be that appropriate to harmonic motion:

$$P(v_m, v) = \begin{cases} \frac{1}{\pi}\frac{1}{(v_m^2 - v^2)^{1/2}} & \text{if } |v| < v_m \\ \\ 0 & \text{otherwise} \end{cases} \tag{7.10}$$

where v_m is the maximum velocity of the ion at the given motional energy.

Starting at a given ion motional energy E, equation 7.9 is numerically integrated to calculate the cooling curve for the ion $E(t)$, and thus $v_m(t)$. Averaging Equation 7.7 for one motional cycle, as a function of $v_m(t)$, one gets the fluorescence rate of the ion as a function of time (see Figure 7.7 and 7.8).

To calculate the predicted fluorescence from a large number of experimental repeats, we assume that the temperature after the heating delay is distributed according to the Maxwell-Boltzmann distribution, where the probability of having motional energy E is

$$P(E) = \frac{1}{\bar{E}} e^{-E/\bar{E}} \tag{7.11}$$

where $\bar{E}$ is the mean energy. The calculation of the fluorescence rate as a function of time is repeated for a number of motional energies, and averaged using the probability distribution of Equation 7.11.

Figure 7.8 shows a fit of 1D motional theory to the recorded fluorescence, in the case of a delay time $\tau_d = 505\,\mathrm{ms}$ to allow the ion to heat up before the cooling lasers were switched on. The fitted temperature at the start of the cooling is $T = 31.3 \pm 2.0K$. In

[60] the temperature derived from simple 1D motional model was compared to results of different temperature estimation (Raman sideband cooling), and found to be consistent. Both [60] and our experiments had similar geometrical arrangement: the laser beam that drives the fluorescence had its k vector at 45° to the axial mode and one of the transverse modes, and close to perpendicular to the other transverse mode. The ion's motion could thus be assumed to be 2-dimensional only as the third mode is barely affected by the laser beam. It was modelled by 1D-cooling in both modes equally since the laser has the same k in both directions due to its incidence angle.

When the radial motion is assumed to be unaffected by heating, or the heating rate is proportional to $\omega^{-1.4}$ (as has been found in other studies), the fitted temperature is similar to the 1D model. When the heating rate is assumed to be independent of ω, the resulting fitted ion temperatures are reduced to about 40% of that obtained from the 1D model. These results suggest that the 1D model describes the cooling process reasonably well, and the uncertainty of the heating rate measurement is more likely to be influenced by the changing environment and uncertainty in experimental control parameters.

7.2.2 Effect of filtering the DC electrode lines

Using the method described above, a comparison was made between the heating rate with unfiltered DC control voltages, and with a low-pass filter to reduce electrical noise on the electrodes. Figure 7.9 shows the recorded noise spectrum for the DC lines when powered by the computer-connected DAC. The axial frequency of the trap is generally in the region of 300-800 kHz, so that the ion's axial motion is likely be excited by the noise on the DC line.

The heating rate was measured first without a filter (the situation for all the previous experiments), then the filter was installed and the measurement repeated (see Section 4.6.2). Figure 7.10 shows that the heating rate is significantly reduced by the filters from $206 \pm 80\,\mathrm{K/s}$ to $60 \pm 9\,\mathrm{K/s}$. An improvement in ion lifetime is also observed.

With the reduced noise on the DC electrodes, it was also possible to have even longer delay times, as it is shown on Figure 7.11. The longest delay time at which the experiments were repeatable was $\tau_d = 755\,\mathrm{ms}$. Times up to 1 s were observed occasionally, with loss a rate of a few per cent.

The heating rate was fitted to be $49 \pm 8\,\mathrm{K/\,s}$, which is in reasonable agreement with the previous experiment (experiments were conducted on different days). The mean occupation number is expressed from the temperature as

$$\langle n \rangle = \frac{1}{e^{\hbar\omega/k_{\mathrm{B}}T} - 1} \tag{7.12}$$

where ω is the trap frequency. For the axial motion of the ion with $\omega_z = 2\pi \times 800\,\mathrm{kHz}$ trap frequency, the measured heating rate corresponds to $\mathrm{d}\langle n \rangle/\mathrm{d}t \approx 1.26 \pm 0.20 \times 10^6 s^{-1}$.

The electric field noise spectral density is calculated as

$$S_E(\omega) \approx \frac{\mathrm{d}\langle n \rangle}{\mathrm{d}t} \frac{4m\hbar\omega}{e^2} \tag{7.13}$$

where m is the ion's mass and e is the elementary charge [61]. In the Sandia system, then

$$S_E(\omega) \approx 6.9(\pm 1.1) \times 10^{-9}\,\mathrm{V}^2\,\mathrm{m}^{-2}\,\mathrm{Hz}^{-1} \tag{7.14}$$

which is higher than most other traps in the literature, but fits into the general trend (see Figure 7.12).

The heating rate we infer from our observations is high. When compared with results reported in the literature for other ion traps, it is at the upper end of the range for traps of the same physical dimensions. This means that in practice this trap, as it stands, is not a viable candidate for the implementation of quantum computing. There is a chance that better filtering could reduce the electric field noise, but given that other groups reported severe problems with this sort of trap, it is more likely that the problems are mainly intrinsic to the trap itself. The evidence from the wider study of small traps in general is that they experience electric field noise due to some as yet unclear unstable behaviour at the electrode surfaces, such as fluctuating patch potentials. There is some evidence (partly anecdotal) that the choice of materials and the smoothness of the electrode surfaces is important. Rather than test the Sandia trap further (for example by attempting sideband cooling) it was decided to move on to other traps, and recommend that the next stage for this design should include a more complete gold coating, and a better surface smoothness. Both are especially important for the surfaces nearest to the ion or ions.

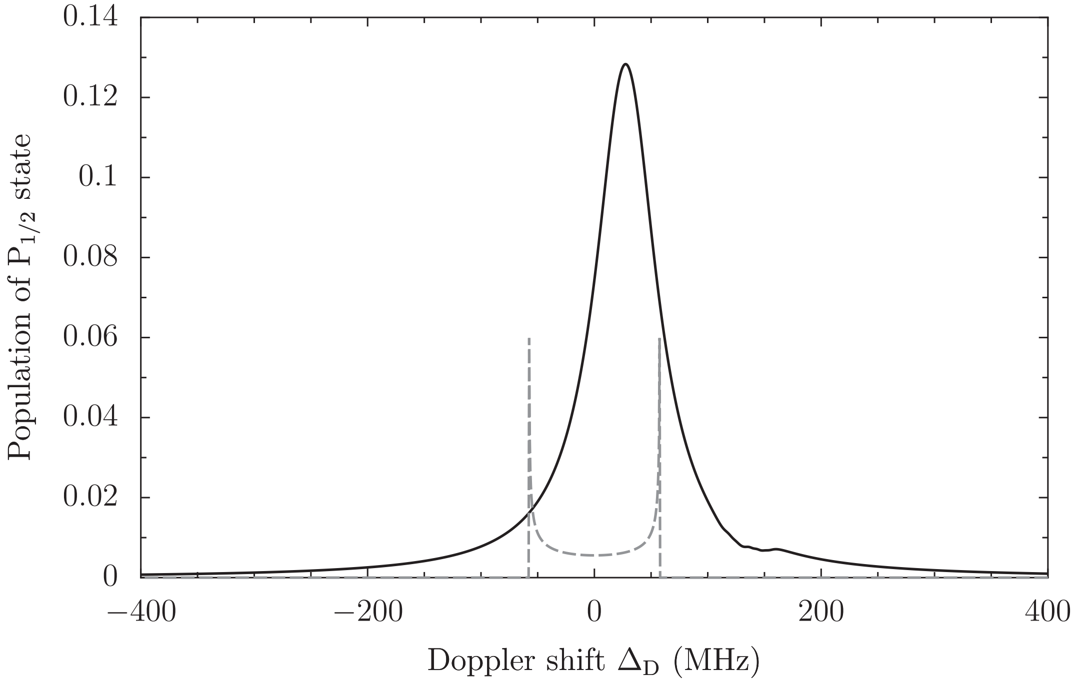

Figure 7.5: Population of the $P_{1/2}$ level as function of Doppler-shift $\Delta_D = -k_z v_z$. The probability distribution of the Doppler-shift in case of maximal cooling rate is shown by the dashed line. Experimental control parameters (laser intensity, detuning, magnetic field) are as in Figure 7.8.

7.3 Ion shuttling

As mentioned in the Introduction, to scale up existing ion trap designs the problem of storage and manipulation of a large number of ions has to be addressed. Many current proposals of designs include different trap regions optimized for storing ions and for ion-ion interaction. The ions thus have to be moved between such regions with high speed and accuracy, while keeping the information stored in the ion's quantum state intact.

Ion shuttling has been demonstrated in other trap designs previously [38]. The Sandia trap offered us an opportunity to get some initial experience of the issues involved. The shuttling of a single ion was studied in two experiments.

In the first instance voltages on most electrodes were kept constant, and only the voltage of one pair of the outermost electrodes was changed (pair #1 or #7, see Figure 4.2).

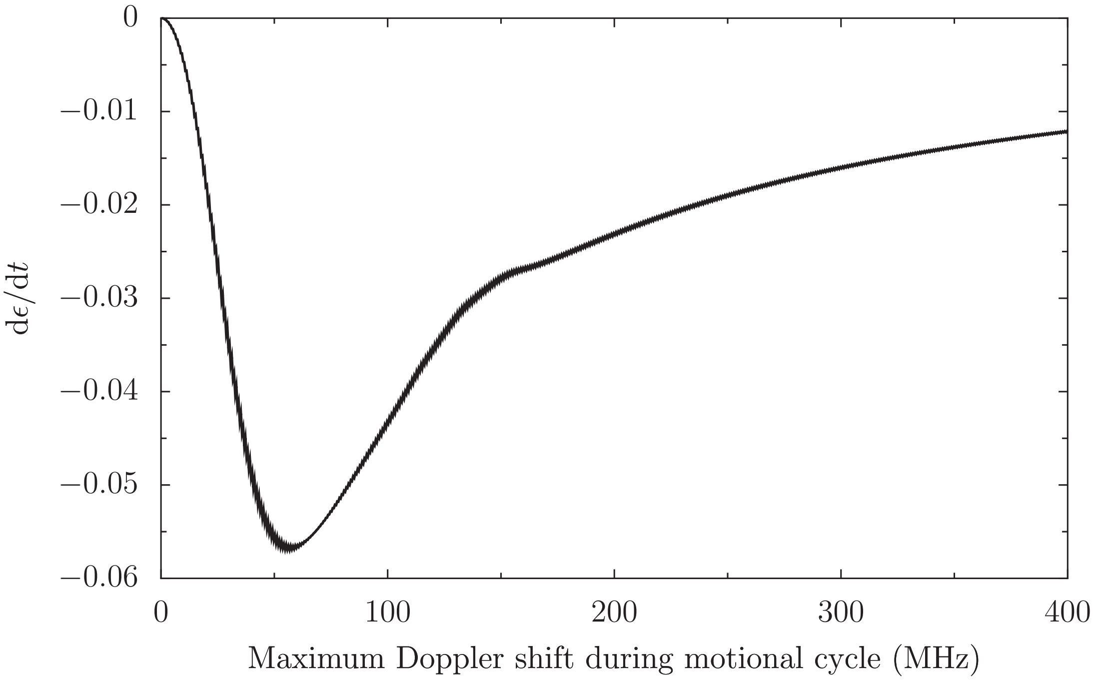

Figure 7.6: The rate of change in ion energy as function of the maximum Doppler shift of the ion's motion. The energy is scaled by $E_0 = \hbar\Gamma$, and the time by $t_0 = \Gamma^{-1}$, where $\Gamma = 2\pi \times 22.4\,\text{MHz}$ is the excited state decay rate. Calculated from curves shown in Figure 7.5.

By changing the voltage on these electrodes, the trapping potential's minimum was displaced from the geometrical trap centre. Because of symmetry, the displacement was along the trapping axis. The CCD camera had a field of vision with a length of approximately 120 μm, limited by a pinhole in the imaging system. The 397 nm beam was elongated in the horizontal direction with a tilted focusing lens before the trap (see Section 4.3.2) and the 866 nm beam had a large spot-size and high power. Thus the lasers stayed in interaction with the ion all the way through the field of view of the CCD camera, and the photon scattering could be observed.

The voltage on the electrode pairs of #1 and #7 was changed in steps, and a picture of the ion was taken. The length scale was calibrated by taking a picture of one of the centre electrodes with known width of 100 μm. Figure 7.13 shows the ion's position as a function of the difference between the voltages on electrode pairs #1 and #7. The dataset contains position information from two ions, as the trap had to be reloaded once during the experiment.

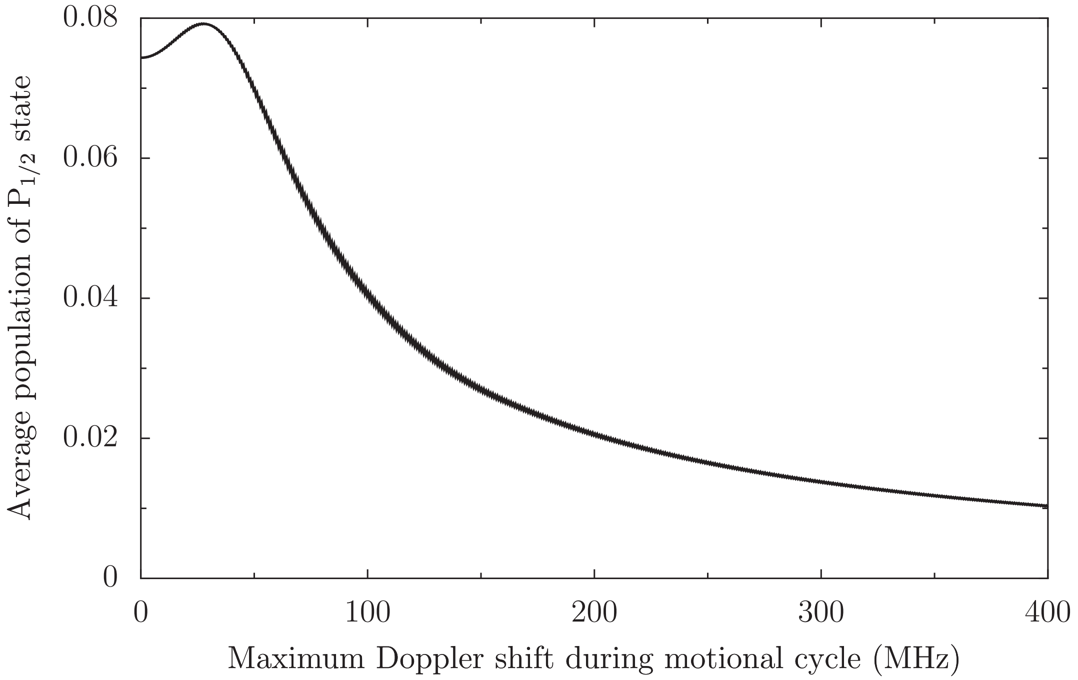

Figure 7.7: Average population of the $P_{1/2}$ level as a function of the maximum Doppler shift of the ion's motion. The scattering rate is Γ times the population of the $P_{1/2}$ level. Calculated from curves shown in Figure 7.5.

The second experiment was to demonstrate shuttling to large distances. The furthest trapping region from the trap centre is in front of the DC electrode pairs #2 or #6, since the outermost electrodes have to produce barrier fields, stopping the ion from leaving the trap along the trap axis. Thus the furthest available shuttle distance is $\pm 360\,\mu$m from the trap centre. Shuttling to such a distance requires changing the voltage on more than one electrode pair. In practice changing 4 out of the 7 DC voltages is sufficient. Depending on the required direction of movement the electrode pairs #1 to #4, or #4 to #7 have to be changed. Figure 7.15 shows the applied voltage as a function of ion distance from the trap centre.

In the experiment we shuttled the ion at a constant speed along the axis: the distance travelled along the trap axis was thus linear in time. This is a very crude initial approach, since significant ion heating is expected due to the "kicking-and-stopping" nature of the control. A smooth acceleration and deceleration would be desirable in practice, to minimize heating (see Section 3.1). However there are several factors which suggest that even the crude approach is acceptable in this case. The Sandia trap has such a high heating

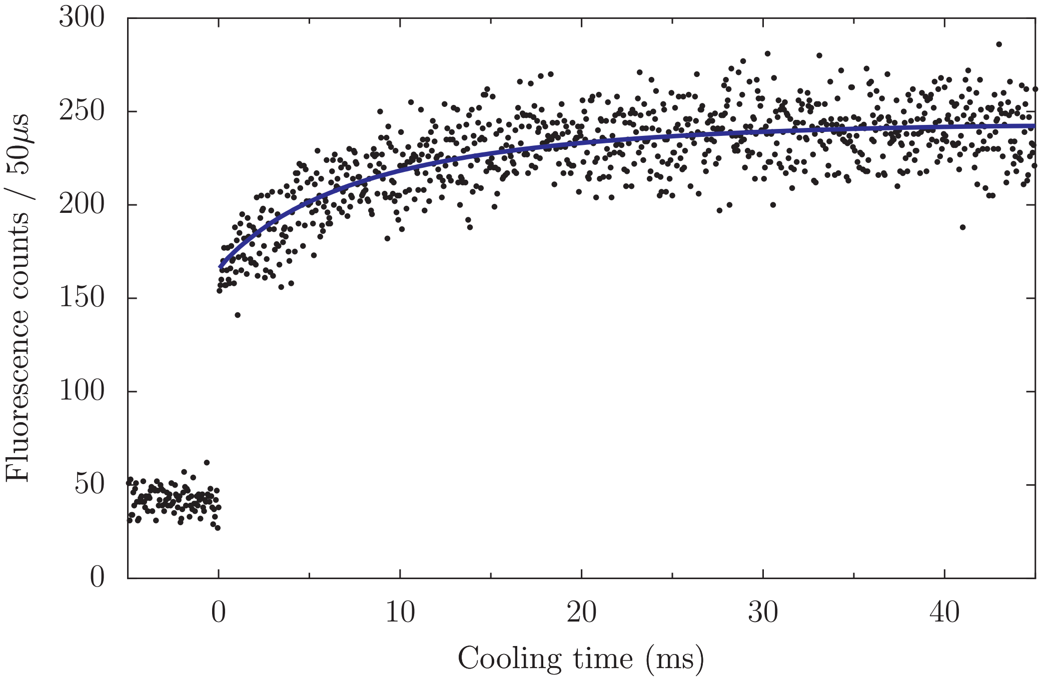

Figure 7.8: Time-resolved fluorescence during Doppler cooling. Cooling starts at $t = 0$. Delay time 505 ms, 301 repetitions, fluorescence is recorded in 50 μs bins. The signal at $-5\,\text{ms} \leq t \leq 0$, before the cooling is turned on, is used to fit the background. The fitted temperature is $T = 31.3 \pm 2.0\,\text{K}$. Experimental parameters are $I_{397} = 3.2 I_{S,397}$, $I_{866} = 39 I_{S,866}$, $\Delta_{397} = -34.2\,\text{MHz}$, $\Delta_{866} = 39.0\,\text{MHz}$, $B = 3.6\,\text{G}$, $\phi_{397} = \pi/4$, $\phi_{866} = \pi/2$.

rate that the additional heating from the ion movement is probably not significant. To experimentally realize the waveforms whose theory was presented in Section 3.1, one needs much better timing resolution that was available to us at the time. Finally, the timescale of the shuttling experiment was in the order of milliseconds, which is close to adiabatic considering the ion motion timescale set by the trap frequency of 600-900 kHz.

The speed of the shuttling was limited by two factors. First, the DAC available at the time of the experiment (PCI-DAC6703) had a maximum 1111 Hz update rate (0.9 ms/update). Second, the RC filters on the DC voltage lines have time constants of $\tau = 0.18\,\mu$s. According to computer calculations to assess the effect of the RC filters, the voltage waveforms were not significantly changed at the maximum update rate of the DAC card. However, if a faster DAC were used, the RC filters would have to be changed to have a higher cut-off frequency. This would lead to a higher level of electric noise on the DC electrodes, thus giving a higher heating rate and shorter ion lifetime. The amount of extra

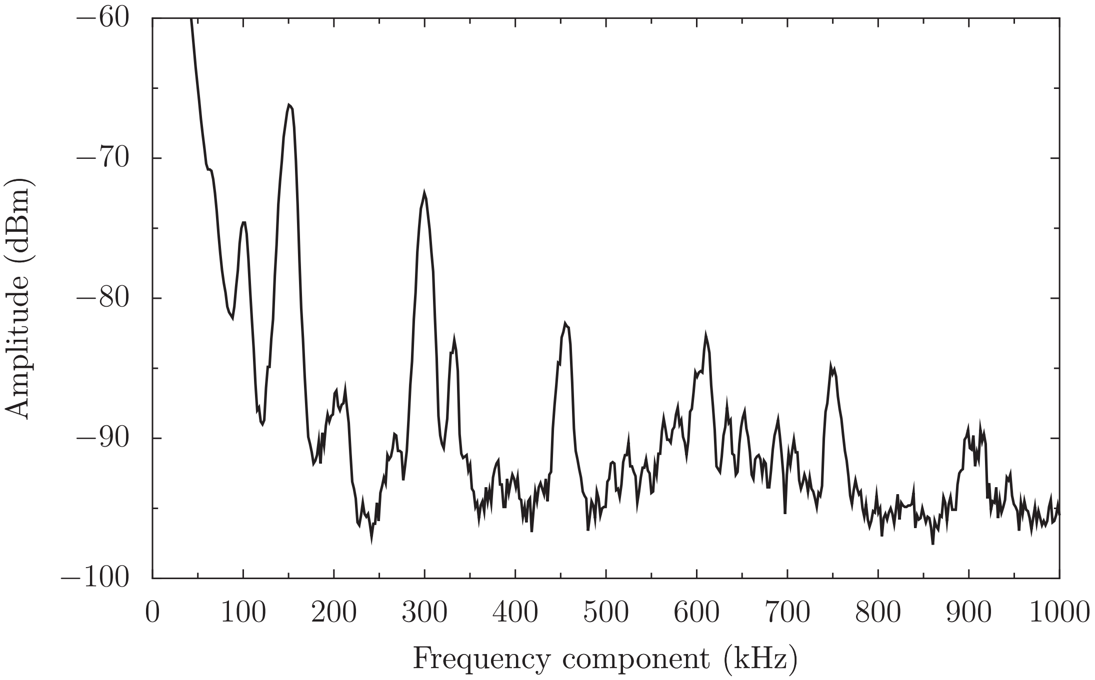

Figure 7.9: DAC noise Fourier spectrum recorded with a Tektronix TDS2024 oscilloscope. High harmonics of 100 kHz and 150 kHz are visible. The usual trap operation is in the 300-900 kHz axial frequency range.

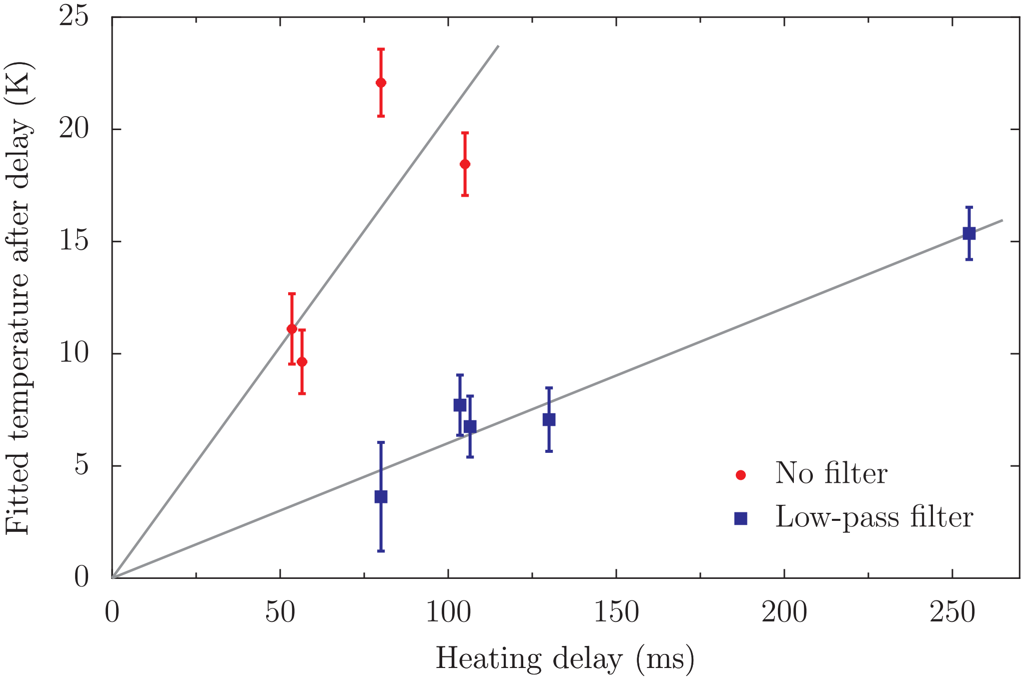

Figure 7.10: Ion temperature after heating up as a function of heating delay, with and without low-pass filters installed on the DC voltage lines. The heating rate without the low-pass filters is 206 ± 80 K/ s, while with filters it is 60 ± 9 K/ s.

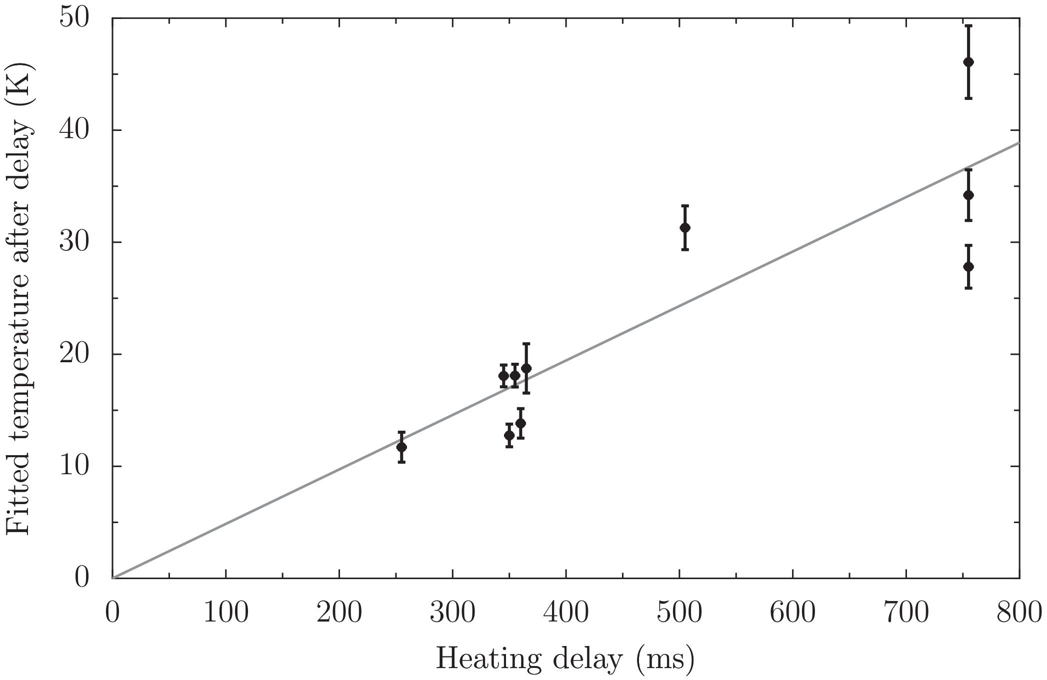

Figure 7.11: Heating rate measurement at long delay times, with DC line low-pass filters. All experiments were done with filters on the DC lines, and the best possible micromotion compensation. Delay times are $\tau_d = \{255, 355, 505, 755\}$ ms. The multiple measurements at 355 ms delay time would overlap too much on this plot, so they have been spread out slightly along the x-axis for clearer presentation. The heating rate is fitted as $49 \pm 8\,\mathrm{K/s}$, which is similar to the heating rate shown in Figure 7.10 (with filters).

heating one can afford to trade for higher shuttling speeds needs further investigation.

In the experiment, the ion was moved to the largest distance allowed in the shortest possible time. Experiments indicated that the required waveforms can be approximated in 10 steps without losing the ion during the shuttle (see Figure 7.16). Less than a 10 step voltage change lost too much detail of the waveforms to provide a reliable shuttle. The 10 step waveform together with a set minimal update time of 1 ms provides a 10 ms shuttle time away and a 10 ms shuttle back to the trap centre. In the experiment a delay was applied before shuttling back to the starting position. For reliable timing, a real-time operating system was used (GNU/Linux 2.6.23[1] , Xenomai[2] and Comedi[3]) which was superior to the DAC's own supplied control software under the Windows operating system. The reliability of timing is demonstrated in Figure 7.16, where 20 repeats of the

---

[1] GNU/Linux Kernel, `http://www.kernel.org/`

[2] Xenomai Real-Time Framework, `http://www.xenomai.org/`

[3] Linux Control and Measurement Device Interface, `http://www.comedi.org/`

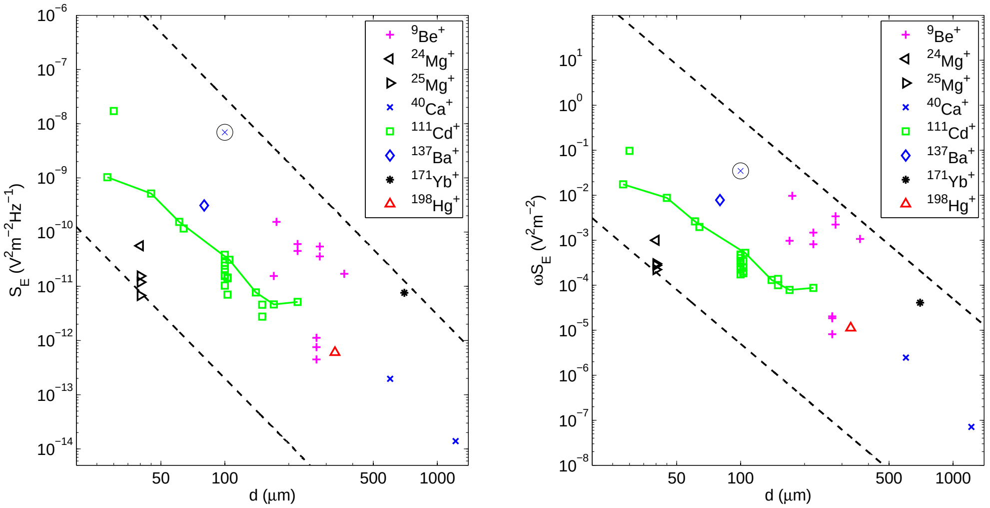

Figure 7.12: Electric field noise spectral density $S_E(\omega)$ (left) and $\omega S_E(\omega)$ (right) for a number of different traps and ion species in the literature. The results of the present work is indicated by circles. References for the other data points: $^9\text{Be}^+$ [44, 16, 61] , $^{24}\text{Mg}^+$ [35], $^{25}\text{Mg}^+$ [60], $^{40}\text{Ca}^+$ [62, 63], $^{111}\text{Cd}^+$ [64, 36, 65], $^{137}\text{Ba}^+$ [66], $^{171}\text{Yb}^+$ [67], $^{198}\text{Hg}^+$ [68]. The data for the same trap is connected by a line. The dashed lines are paralled to d^{-4}. (Colour in electronic version)

voltage waveform are recorded and show good repeatability. The remaining variability of the signal is partly due to the control electronics of the DAC: the order in which the output channels are updated seems to vary in every update round.

Figure 7.14 shows a recorded fluorescence signal during shuttling of an ion when a 120 ms delay time was applied between the outward and inward movement. With this delay time the ion was reliably shuttled more than 500 times. However, at larger delay times the ion was lost in a small number repeats. The half a second delay between repeats is due to software limitations, as the hardware was reprogrammed before every shuttle.

According to the results in the previous section, the amount of time the ion stayed reliably in the trap after loss of cooling was in the order of 500-750 ms. The fact that the observed maximum delay to reliably shuttle an ion (120 ms) is shorter suggests that either the shuttle contributed to the heating of the ion or that the trapping at the end points is inherently less stable.

The ion shuttling described was paving the way for experiments with multiple ions, when ions are stored in different trapping regions. Based on the results of the ion shuttling, with Doppler-cooling beams at the different trapping regions in addition to the trap centre, it would be possible to keep ions for a significant amount of time while moving them. One additional aspect of the multi-ion experiment is the separating and joining of ion pairs in a trapping region. It is not clear whether the Sandia trap is capable of doing this; certainly, to be able to test any ion-pair manipulation method (such as the precise shuttling sequence in Section 3.1), the ion pair lifetime in the Sandia trap would need to be improved (see Section 6.5).

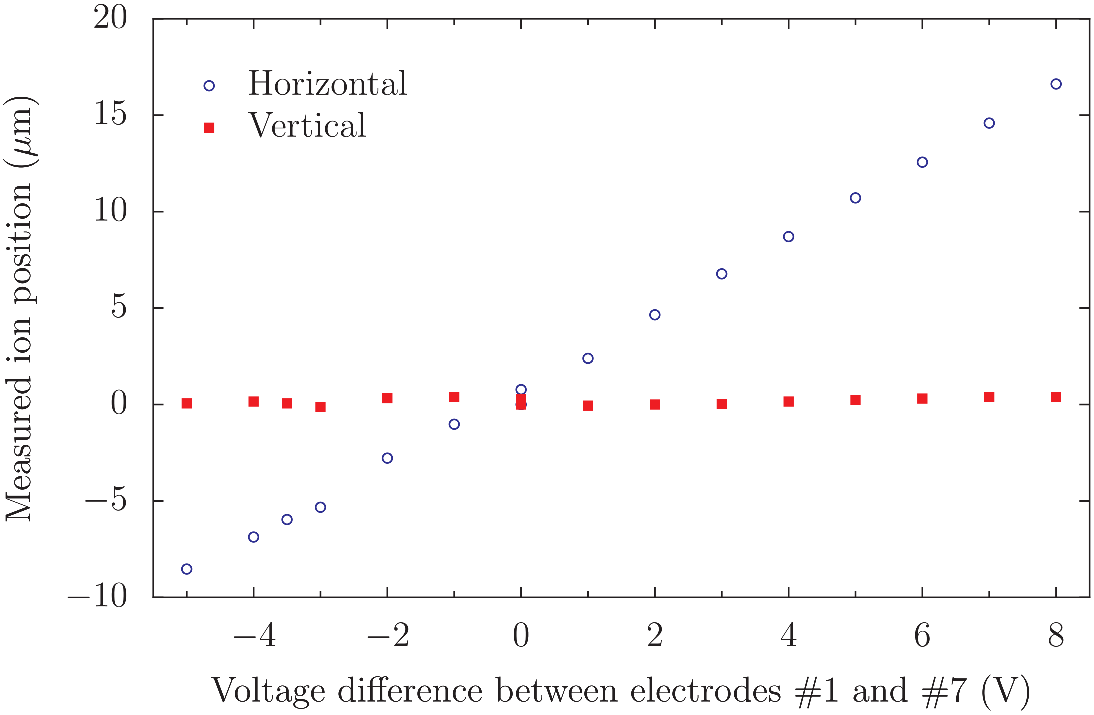

Figure 7.13: Moving the ion step by step with the outermost electrode pairs. The ion's position is plotted versus voltage difference between the #1 and #7 electrode pairs. The position is deduced by CCD pictures and known scaling factor for the images.

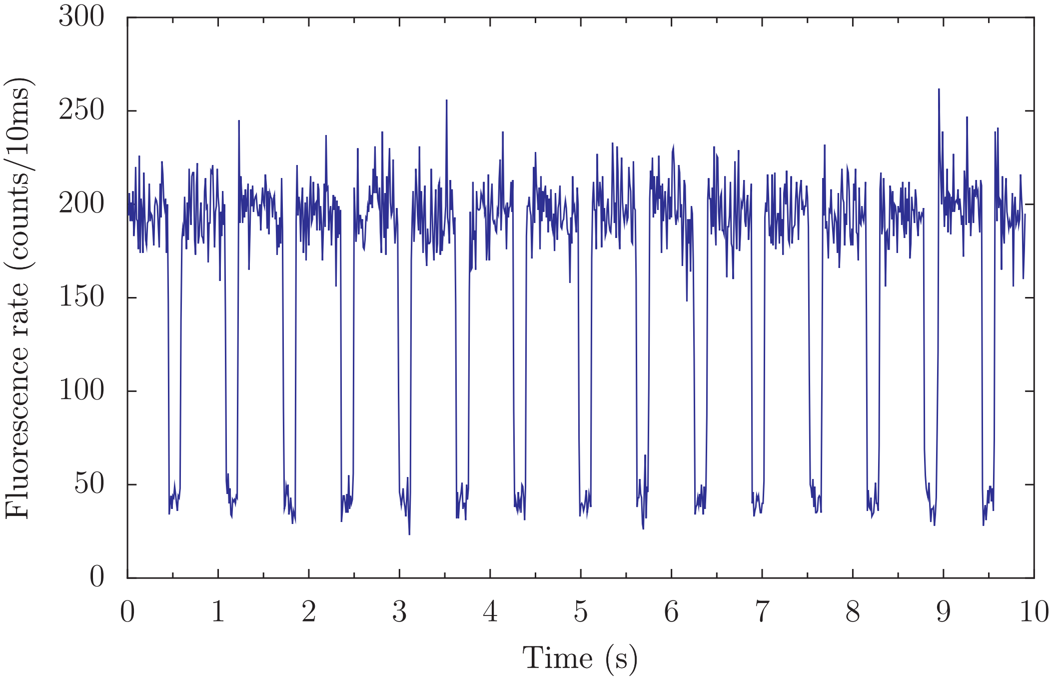

Figure 7.14: Fluorescence signal during ion shuttle. The outward and inward movement is 10 ms each, while a delay of 120 ms is applied between them. The shuttle repetition was limited to 1 every 700 ms due to the calculation overhead between shuttles.

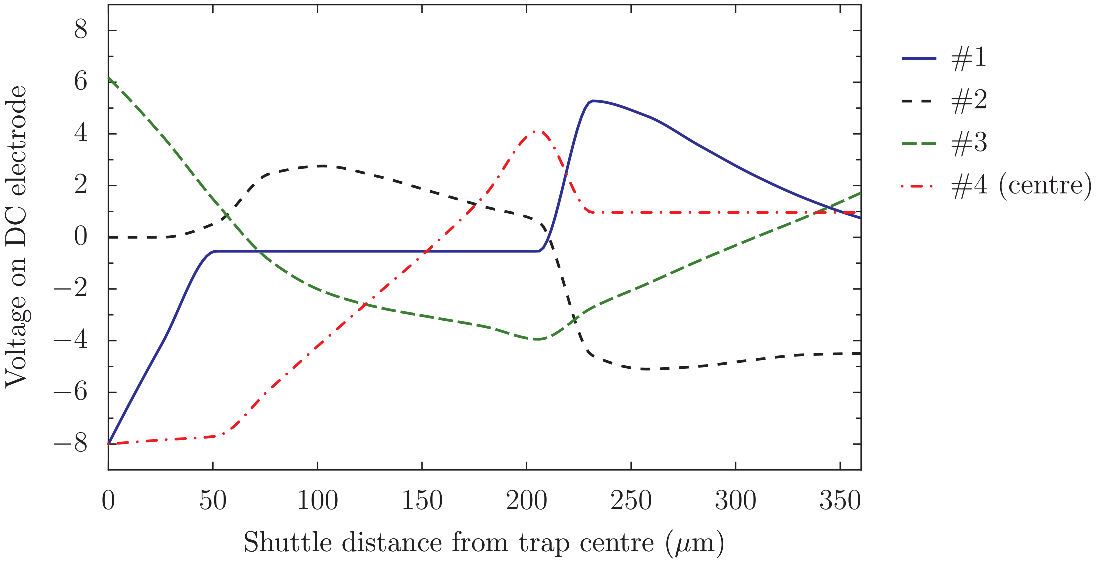

Figure 7.15: Voltages on DC electrodes as a function of ion's distance from trap centre. Only 4 of 7 possible voltages are plotted, as the other 3 voltages are kept constant during the shuttle. The electrodes used to shuttle ion to the left (right) are #1,2,3,4 (#7,6,5,4).

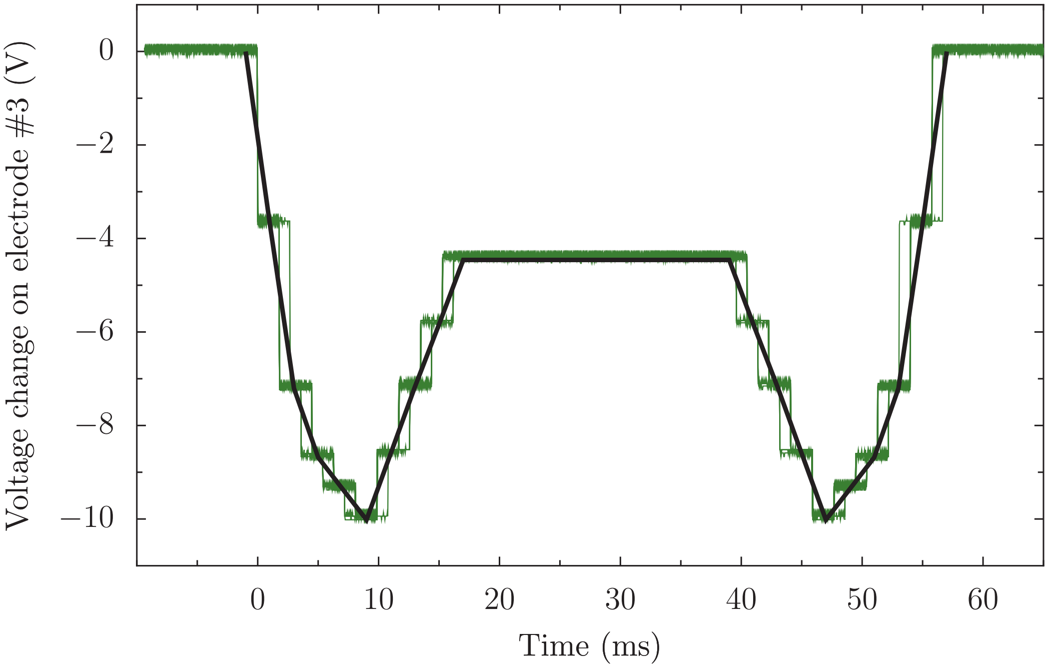

Figure 7.16: Example of recorded waveform for electrode pairs #3. The solid line connects the set voltages; update rate is 1/ ms. The voltages were recorded by an oscilloscope, and 20 repeats are plotted.

Chapter 8

Conclusion

This thesis presents a study of various issues in the extension of ion trap quantum computing experiments to small traps and arrays of traps. Two specific trap arrays were studied in some detail by numerical modelling and one of these was developed and operated experimentally.

The first is an ion trap designed for fast ion separation ("Liverpool trap"). It is a mesoscopic ion trap, which is considered a transition stage to combine easier manufacturing with the ability to test a geometry developed for microscopic segmented designs. Chapter 2 presents an overview of computer modelling of ion traps, and applies the methods to analyse the behaviour of the Liverpool trap. It was found that trapping outside the trap centre will result in large, uncompensatable micromotion along the trap axis. Differences between the original design and the actual trap geometry after assembly were evaluated, with the conclusion that in the radial direction also, micromotion compensation could be difficult due to the imperfections of electrode alignment.

The second design ("Sandia trap") is a true microfabricated segmented ion trap. A major part of this thesis is the experimental evaluation of this trap. Chapter 4 introduces the experimental equipment and several issues which arose while building up the system.

In Chapter 5 the preparation of the vacuum system is detailed together with the first testing of the calcium oven and laser system to observe neutral atom fluorescence. The neutral atom density was inferred as a function of calcium oven drive current. This allowed us to use a low drive current in order to limit both coating of the trap with calcium and the depletion of the oven. It also gave us good knowledge of the flux in the atomic beam, which is a useful diagnostic.

Previously only the NIST Ion Storage Group in the USA had been able to trap in the Sandia trap design, while the University of Innsbruck Ion Trapping Group in Austria and the University of Michigan Trapped Ion Quantum Computing Group were unsuccessful. We also experienced difficulty, though with eventual success. Chapter 3 presents a numerical study of ion loading as a function of RF voltage amplitude in the Sandia trap. The calculations showed that voltages higher than 50 V have to be present on the RF rails to have significant trapping probability, and that high energy and low energy ions tend to be trapped with different ionization positions in the trapping region: low energy ions in the central part of the trapping region, high energy ions in the outer areas. Chapter 6 is concerned with the first experiments with ions in the Sandia trap, and details the successful loading of the trap. Once ion loading was reliable, micromotion compensation was performed in both radial directions and monitored using an RF-photon correlation method. A number of factors were identified as influencing the micromotion compensation. The running of the calcium oven significantly changed the compensation, while previously suspected UV charging of the electrodes due to the photoionisation laser beams was not observed. The room lighting was shown to cause an instantaneous, reversible, significant compensation change, the mechanism of which is not yet clear.

The ion lifetime was measured with a range of parameter settings and a lifetime shortening effect of the calcium oven was established. Low oven currents significantly increased the expected lifetime. Ultimately an ion lifetime of over two hours was achieved. The axial and radial trap frequencies were measured by resonant excitation of the ion, which allowed comparison of experimental results with the predictions of the computer models of the trap. They agreed to about 10%. Loading of multiple ions in a reliable fashion was attempted. Initially it was impossible to load pairs of ions. When the axial vibrational frequency of the trap was lowered from 800-900 kHz to 300 kHz, ion pair loading was successful, though their lifetime was then only of the order of a minute.

In Chapter 7 the characterization of the Doppler-cooling beams is presented, followed by details of two additional experiments not previously attempted using the Sandia trap.

The first was to measure the motional heating rate of the ion by time-resolved recording of fluorescence during Doppler-cooling, after the ion was allowed to heat up by turning off the Doppler-cooling beams. The analysis brought to light a high heating rate due to high frequency noise on the DC electrodes. Installing low-pass filters on the DC voltage lines reduced the heating rate by a factor of 3, to 60 ± 8.5 K/s. Additional experiments showed that this value is fairly stable day-to-day. Ions were reliably stored up to about 755 ms with the cooling beams extinguished. To compare the Sandia trap with other trap designs, the electric field noise spectral density was calculated. It is shown that, while it has a very high heating rate, the Sandia trap fits into the general trend observed in ion traps, where the heating rate scales as $\omega^{-2.4}$ with the trap frequency ω, and as d^{-4} with the distance d of the ion and the nearest electrode. Our trap had an axial vibrational frequency $\omega/2\pi$ = 300-900 kHz and characteristic distance of $d = 100\,\mu$m, so a high heating rate is not surprising.

Chapter 3 contains a description of a precise ion shuttling method. The idea is to engineer the time dependence of the moving potential well to transport the ion with velocity corresponding to a predefined time-dependent function. This allows motional heating to be avoided, up to the limit set by the achievable precision of the voltage waveforms and modelling of the trap. Chapter 7 contains results of initial ion shuttling experiments in our lab. A single ion was transported to a distance of $360\,\mu$m (the maximum possible in the Sandia trap) along the trap axis and back, repeatedly, on a few millisecond time scale. When a delay was added between the outward and inward shuttle, a maximum delay time of 120 ms was achieved, over which the shuttle was still 100% reliable over 500+ repeats. Longer delay times resulted in ion loss. Comparing the 755 ms longest storage time in the absence of cooling with the maximum shuttle delay of 120 ms, it is clear that the shuttling results in a less stable system. This could be either owing to the method of shuttle, or the higher electric field noise at the position away from the trap centre, or a combination of the two.

Overall, the results suggest that microfabricated ion trap arrays are feasible and should be pursued, and that the particular designs considered here merit further studies.

8.1 Further plans

Several of the experiments described in the thesis are to be further developed. The Liverpool trap was recently made operational, successfully trapping ions, and initial testing is under way. It will allow testing of ion shuttling and ion-pair separation more readily than the Sandia trap, due to its larger trap depth and lower noise. It has already been shown that loading multiple ions is much easier and they have a long lifetime (several hours) and lower heating rate, even without precise micromotion compensation. Faster electronics are to be installed to conduct fast ion separation experiments, implementing the method presented in Section 3.1.

Despite its apparent limitations, our work has shown that the Sandia microfabrication method produced a viable trap. It is not as stable as it needs to be, e.g. having high heating rate for single ions and short lifetime for multiple ions, but these issues will partly be addressed in the new version of the trap, such as through better coating of surfaces which promises to reduce stray charge build-up and heating. Further studies are warranted to measure the heating rate of this and other new traps and implement cooling to the motional ground state.

The new experimental setup developed for this work has the advantage that it allows us to change traps relatively easily, e.g. currently the Sandia trap is switched out in order to test a different ion trap from Lucent Technologies. Other trap designs with 2D structure, such as Y-junctions, are likely to be tested in the near future. Extending the experiments such as entanglement and quantum gate operations from single trapping region to trap arrays is also in the planning stage.

In the medium and longer term, further elements of the ion trap quantum computing paradigm can be realized.

Appendix A

Calculation of voltage configurations

The following programs were developed to calculate voltages in the modelled ion traps.

A.1 Function to solve voltage configuration

The following Matlab program calculates voltages on electrodes given a number of constraints: the location and the force experienced by the ion, and that specified electrodes be kept at a fixed voltage. The potential function generated by a unit voltage on a given electrode is passed as an input parameter to this program. The output is a set of voltages satisfying the constraints. In this setting one can calculate the voltages for trapping at an arbitrary position — as e.g. in Sections 2.3.2 and 2.4, or the voltages needed for ion shuttling — as in Section 3.1.

The format in which the potential functions were stored was as follows. A chosen electrode is set to 1 volt with the other electrodes grounded, and CPO was used to calculate the potential at 1000 positions along the z axis. This set of points was then fitted with an order 34 polynomial. The 35 coefficients were stored. Other methods to store the same information are possible. For example, one could pick a set of representative points along the z axis and fit a lower order polynomial for each, or one could use another curve fitting method such as a Padé approximation [69].

```
function vout = voltprepare(elecs,params,backg,pots,f,x0)
% vout = voltprepare(elecs,params,backg,pots,f,x)
%
% Input:
% ------
% elecs : electrode #s, for which the voltages have to be calculated
% params : [w0 m a0 q] to describe the system and the trapping strength one
%        wants to achieve
% backg : [num1 volt1; num2 volt2;...] electrode numbers and voltage values for
%        those electrodes which have a constant set value
% pots : the database for the polinomials describing the potentials
% f   :  force on the ion
% x0   :  position of ion
%
% Output:
% -------
% vout : list of voltages for electrodes in 'elecs', to fullfill the set
%       requirements
%
```

```
%Getting parameters for system
w0 = params(1);
m = params(2);
a0 = params(3);
q = params(4);

%number of electrodes changed and static background electrodes
n = length(elecs);
bn = size(backg);
bl = bn(1);

%Distance conversion from dimensionless
x = x0*2*a0;

%Setting up the coefficient matrix for the equations
%Dimensionless form
A = zeros(n);
for i = 1:n
    for j = 1:n
        enum = elecs(j);
        v = pots(enum,:);
        for k = 1:i
            v = derivate(v);
        end
        A(i,j) = polyval(v,x);
    end
    A(i,:) = A(i,:)*(q/(2*a0*m*w0^2))*(2*a0)^(i-1);
end

%Setting up the other part of the equation system
%Background values
b = zeros(n,1);
if bl > 0
    for i = 1:n

          for j = 1:bl
            enum = backg(j,1);
            v = pots(enum,:);
            for k = 1:i
                v = derivate(v);
            end
            b(i) = b(i)-backg(j,2)*polyval(v,x);
          end
          b(i) = b(i)*(q/(2*a0*m*w0^2))*(2*a0)^(i-1);
    end
end
%Required values
b(1) = b(1) + f;
b(2) = b(2) - 1;

%Solving equation system and returning the solution
al = 0.0002;  % small constant to avoid singularity

% output
vout = inv(A.' * A  + al^2*eye(n)) * A.' * b;


%% Differentiation of a polinomial
function coeff_derivative=derivate(coeff_function)
der_order=size((coeff_function),2)-1;
coeff_derivative=0;
for index=1:size((coeff_function),2)-1
    coeff_derivative(index)=der_order*coeff_function(index);
    der_order=der_order-1;
end
```

A.2 Voltage to trap at arbitrary position along the trap axis

The following program uses the routine presented in the previous section to calculate the required voltages for a single potential well with 1 MHz trapping frequency along the Z axis in the Liverpool trap.

```
%% Voltage on all electrodes for single trapping point along the Z axis

%%%%parapmeters, 40Ca+
w0 = 1e6*2*pi;              % trap frequency
mamu = 1.67e-27;            % atomic mass unit
ml = 40*mamu;               % Ca-40
hbar = 1.05457148e-34;      % h-bar
a0 = sqrt(hbar/(2*ml*w0))   % distance scaling
q = -1.60217653e-19;        % unit charge

%Database polinomial coefficients of electrode potentials
pots = load('v_base.dat');

%Dimensionless unit of electrode separation of
xmax = 0.7525*1e-3/2/a0;

%Simulated points: between electrodes -2 to 2
x = linspace(-2.1*xmax,2.1*xmax,200);


%The background electrodes' voltage
backv = 0;


% Calculation of voltages
for i = 1:length(x)
    v = voltprepare([1 2 3 4 5 6 7],[w0 ml a0 q],[],pots,0,x(i));
    vl(i,1:7) = v(1:7);
end


%Plotting results
mk = {'b-','r--','g-.','kx-','b--','r-.','g+-'};
figure(2)
for k = 1:7
    plot(x*2*a0/0.7525*1e3,vl(:,k),mk{k},'LineWidth',2)
    hold on;
end
hold off;
 set(gca,'XTick',-2:1:2,'XTickLabel','#2|#3|#4|#5|#6','FontSize',14)
legend('v1','v2','v3','v4','v5','v6','v7')
xlim([-2.1 2.1])
xlabel('well-position (compared to electrode positions)','FontSize',16)
ylabel('Voltage on electrode (V)','FontSize',16);
```

A.3 Voltages for short shuttle

The following program calculates the voltages for preparing a 1 MHz potential well at a range of positions between the centre electrode and the one next to that in the Liverpool trap. Voltages changed only on those two electrodes, all other electrodes are kept constant at 12 V.

```
%% Short shuttle with two electrodes

%%%%parapmeters, 40Ca+
w0 = 1e6*2*pi;              % trap frequency
mamu = 1.67e-27;            % atomic mass unit
```

```
ml = 40*mamu;               % Ca-40
hbar = 1.05457148e-34;      % h-bar
a0 = sqrt(hbar/(2*ml*w0))   % distance scaling
q = -1.60217653e-19;        % unit charge

%Database polinomial coefficients of electrode potentials
pots = load('v_base.dat');

%Dimensionless unit of electrode separation of
xmax = 0.7525*1e-3/2/a0;

%Simulated points: between electrodes -2 to 2
x = linspace(0,xmax,200);

%The background electrodes' voltage
backv = 12;

%Calculation
for i = 1:length(x)
    v = voltprepare([4 5],[w0 ml a0 q],[1 backv; 2 backv; 3 backv; 6 backv; 7 backv],pots,0,x(i));
    vl(i,1:2) = v(1:2);
end

%Plotting
mk = {'kx-','b--','r-.'};
figure(2)
for k = 1:2
    plot(x*2*a0*1e3,vl(:,k),mk{k},'LineWidth',2)
    hold on;
end
hold off;
legend('v4','v5')
xlabel('well-position (compared to electrode positions)','FontSize',14)
ylabel('Voltage on electrode (V)','FontSize',14);
```

Bibliography

[1] R. P. Feynman. Simulating physics with computers. *Int. J. Theor. Phys.*, 21:467–488, 1982.

[2] R. P. Feynman. Quantum mechanical computers. *Found. Phys.*, 16:507–531, 1986.

[3] D. Deutsch. Quantum computational networks. *Proc. Roy. Soc. A*, 425(1868):73–90, 1989.

[4] Adriano Barenco, Charles H. Bennett, Richard Cleve, David P. DiVincenzo, Norman Margolus, Peter Shor, Tycho Sleator, John A. Smolin, and Harald Weinfurter. Elementary gates for quantum computation. *Phys. Rev. A*, 52(5):3457–3467, November 1995.

[5] Tycho Sleator and Harald Weinfurter. Realizable universal quantum logic gates. *Phys. Rev. Lett.*, 74(20):4087–4090, May 1995.

[6] P. W. Shor. Algorithms for quantum computation: Discrete logarithms and factoring. *Proc. 35th Annual Symposium of Foundations of Computer Science*, 1994.

[7] Lov K. Grover. Quantum mechanics helps in searching for a needle in a haystack. *Phys. Rev. Lett.*, 79(2):325–328, Jul 1997.

[8] M.A. Nielson and I.L. Chuang. *Quantum Computation and Quantum Information.* Cambridge University Press, 2000.

[9] E. Knill, R. Laflamme, and G. J. Milburn. A scheme for efficient quantum computation with linear optics. *Nature*, 409:46–52, 2001.

[10] J. Q. You and Franco Nori. Superconducting circuits and quantum information. *Physics Today*, 58(11):42–47, November 2005.

[11] Hans-Andreas Engel, L. P. Kouwenhoven, Daniel Loss, and C. M. Marcus. Controlling spin qubits in quantum dots. *Quantum Information Processing*, 3:115–132, 2004.

[12] H.-J. Briegel, T. Calarco, D. Jaksch, J.I. Cirac, and P. Zoller. Quantum computing with neutral atoms. *Journal of Modern Optics*, 47:415–451, 2000.

[13] Ivan H. Deutsch, Gavin K. Brennen, and Poul S. Jessen. Quantum computing with neutral atoms in an optical lattice. *Fortschritte der Physik*, 48:925–943, 2000.

[14] J. I. Cirac and P. Zoller. Quantum computations with cold trapped ions. *Phys. Rev. Lett.*, 74(20):4091–4094, May 1995.

[15] J. I. Cirac and P. Zoller. A scalable quantum computer with ions in an array of microtraps. *Nature*, 404:579–581, 2000.

[16] C. Monroe, D. M. Meekhof, B. E. King, S. R. Jefferts, W. M. Itano, D. J. Wineland, and P. Gould. Resolved-sideband raman cooling of a bound atom to the 3d zero-point energy. *Phys. Rev. Lett.*, 75(22):4011–4014, Nov 1995.

[17] F. Schmidt-Kaler, S. Gulde, M. Riebe, T. Deuschle, A. Kreuter, G. Lancaster, C. Becher, J. Eschner, H. Hffner, and R. Blatt. The coherence of qubits based on single ca+ ions. *J. Phys. B: At. Mol. Opt. Phys.*, 36:623–636, 2003.

[18] C. A. Sackett, D. Kielpinski, B. E. King, C. Langer, V. Meyer, C. J. Myatt, M. Rowe, Q. A. Turchette, W. M. Itano, D. J. Wineland, and C. Monroe. Experimental entanglement of four particles. *Nature*, 404:256–259, 2000.

[19] D. Leibfried, B. DeMarco, V. Meyer, D. Lucas, M. Barrett, J. Britton, W. M. Itano, B. Jelenkovic, C. Langer, T. Rosenband, and D. J. Wineland. Experimental demonstration of a robust, high-fidelity geometric two ion-qubit phase gate. *Nature*, 422:412–415, 2003.

[20] J. Chiaverini, D. Leibfried, T. Schaetz, M. D. Barrett, R. B. Blakestad, J. Britton, W. M. Itano, J. D. Jost, E. Knill, C. Langer, R. Ozeri, and D. J. Wineland. Realization of quantum error correction. *Nature*, 432:602–605, 2004.

[21] M. Riebe, H. Hffner, C. F. Roos, W. Hnsel, J. Benhelm, G. P. T. Lancaster, T. W. Krber, C. Becher, F. Schmidt-Kaler, D. F. V. James, and R. Blatt. Deterministic quantum teleportation with atoms. *Nature*, 429:734–737, 2004.

[22] D. Leibfried, E. Knill, S. Seidelin, J. Britton, R. B. Blakestad, J. Chiaverini, D. B. Hume, W. M. Itano, J. D. Jost, C. Langer, R. Ozeri, R. Reichle, and D. J. Wineland. Creation of a six-atom 'schrödinger cat' state. *Nature*, 438:639–642, 2005.

[23] H. Hffner, W. Hnsel, C. F. Roos, J. Benhelm, D. Chek al kar, M. Chwalla, T. Krber, U. D. Rapol, M. Riebe, P. O. Schmidt, C. Becher, O. Ghne, W. Dr, , and R. Blatt. Scalable multiparticle entanglement of trapped ions. *Nature*, 438:643–646, 2005.

[24] B. B. Blinov, D. L. Moehring, L.-M. Duan, and C. Monroe. Observation of entanglement between a single trapped atom and a single photon. *Nature*, 428:153–157, 2004.

[25] Stephan Gulde, Mark Riebe, Gavin P. T. Lancaster, Christoph Becher, Jrgen Eschner, Hartmut Hffner, Ferdinand Schmidt-Kaler, Isaac L. Chuang, and Rainer Blatt. Implementation of the deutschjozsa algorithm on an ion-trap quantum computer. *Nature*, 421:48–50, 2003.

[26] K.-A. Brickman, P. C. Haljan, P. J. Lee, M. Acton, L. Deslauriers, and C. Monroe. Implementation of grover's quantum search algorithm in a scalable system. *Phys. Rev. A*, 72:050306, 2005.

[27] J. Chiaverini, J. Britton, D. Leibfried, E. Knill, M. D. Barrett, R. B. Blakestad, W. M. Itano, J. D. Jost, C. Langer, R. Ozeri, T. Schaetz, and D. J. Wineland. Implementation of the semiclassical quantum fourier transform in a scalable system. *Science*, 308(5724):997–1000, 2005.

[28] A. Steane. The ion trap quantum information processor. *Appl.Phys. B*, 64:623, 1997.

[29] R. Ozeri, W. M. Itano, R. B. Blakestad, J. Britton, J. Chiaverini, J. D. Jost, C. Langer, D. Leibfried, R. Reichle, S. Seidelin, J. H. Wesenberg, and D. J. Wineland. Errors in trapped-ion quantum gates due to spontaneous photon scattering. *Phys. Rev. A*, 75:042329, 2007.

[30] M. J. McDonnell, J. P. Home, D. M. Lucas, G. Imreh, B. C. Keitch, D. J. Szwer, N. R. Thomas, S. C. Webster, D. N. Stacey, and A. M. Steane. Long-lived mesoscopic entanglement outside the lamb-dicke regime. *Physical Review Letters*, 98(6):063603, February 2007.

[31] J. P. Home, M. J. McDonnell, D. M. Lucas, G. Imreh, B. C. Keitch, D. J. Szwer, N. R. Thomas, S. C. Webster, D. N. Stacey, and A. M. Steane. Deterministic entanglement and tomography of ion-spin qubits. *New Journal of Physics*, 8:188, September 2006.

[32] D. M. Lucas, B. C. Keitch, J. P. Home, G. Imreh, M. J. McDonnell, D. N. Stacey, D. J. Szwer, and A. M. Steane. A long-lived memory qubit on a low-decoherence quantum bus. *Pre-print*, arXiv:0710.4421, October 2007.

[33] A. H. Myerson, D. J. Szwer, S. C. Webster, D. T. C. Allcock, M. J. Curtis, G. Imreh, J. A. Sherman, D. N. Stacey, A. M. Steane, and D. M. Lucas. High-fidelity readout of trapped-ion qubits. *Physical Review Letters*, 100(20):200502, 2008.

[34] J. P. Home, M. J. McDonnell, B. C. Keitch, D. J. Szwer, D. Lucas, D. N. Stacey, and A. M. Steane. Memory coherence of a sympatherically cooled trapped-ion qubit. *(in preparation)*.

[35] S. Seidelin, J. Chiaverini, R. Reichle, J. J. Bollinger, D. Leibfried, J. Britton, J. H. Wesenberg, R. B. Blakestad, R. J. Epstein, D. B. Hume, W. M. Itano, J. D. Jost, C. Langer, R. Ozeri, N. Shiga, and D. J. Wineland. Microfabricated surface-electrode ion trap for scalable quantum information processing. *Physical Review Letters*, 96:253003, 2006.

[36] D. Stick, W. K. Hensinger, S. Olmschenk, M. J. Madsen, K. Schwab, and C. Monroe. Ion trap in a semiconductor chip. *Nature Physics*, 2:36–39, 2006.

[37] W. K. Hensinger, S. Olmschenk, D. Stick, D. Hucul, M. Yeo, M. Acton, L. Deslauriers, C. Monroe, and J. Rabchuk. T-junction ion trap array for two-dimensional ion shuttling, storage, and manipulation. *Applied Physics Letters*, 88(3):034101, 2006.

[38] G Huber, T Deuschle, W Schnitzler, R Reichle, K Singer, and F Schmidt-Kaler. Transport of ions in a segmented linear paul trap in printed-circuit-board technology. *New Journal of Physics*, 10(1):013004, 2008.

[39] P. A. Barton, C. J. S. Donald, D. M. Lucas, D. A. Stevens, A. M. Steane, and D. N. Stacey. Measurement of the lifetime of the 3d2D5/2 state in 40Ca+. *Phys. Rev. A*, 62(3):032503, Aug 2000.

[40] J. P. Home and A. M. Steane. Electrode configurations for fast separation of trapped ions. *Quantum Information and Computation*, 6:289–325, 2006.

[41] D. M. Lucas, A. Ramos, J. P. Home, M. J. McDonnell, S. Nakayama, J.-P. Stacey, S. C. Webster, D. N. Stacey, and A. M. Steane. Isotope-selective photoionization for calcium ion trapping. *Physical Review A (Atomic, Molecular, and Optical Physics)*, 69(1):012711, 2004.

[42] R. Reichle, D. Leibfried, R.B. Blakestad, J. Britton, J.D. Jost, E. Knill, C. Langer, R. Ozeri, S. Seidelin, and D.J. Wineland. Transport dynamics of single ions in segmented microstructured paul trap arrays. *Fortschritte der Physik*, 54:666–685, 2006.

[43] D. Hucul, M. Yeo, W. K. Hensinger, J. Rabchuk, S. Olmschenk, and C. Monroe. On the transport of atomic ions in linear and multidimensional ion trap arrays. *Pre-print*, arXiv:quant–ph/0702175v3, 2008.

[44] M. A. Rowe, A. Ben-Kish, B. DeMarco, D. Leibfried, V. Meyer, J. Beall, J. Britton, J. Hughes, W. M. Itano, B. Jelenkovic, C. Langer, T. Rosenband, and D. J. Wineland. Transport of quantum states and separation of ions in a dual rf ion trap. *Quantum Information and Computation*, 2:257–271, 2002.

[45] M. J. Curtis. Micro-scale segmented ion traps. First Year Report, University of Oxford, August 2007.

[46] B. C. Keitch. *A Quantum Memory Qubit in Calcium-43*. PhD thesis, University of Oxford, 2007.

[47] R. W. P. Drever, J. L. Hall, F. V. Kowalski, J. Hough, G. M. Ford, A. J. Munley, and H. Ward. Laser phase and frequency stabilization using an optical resonator. *Appl.Phys. B*, 31:97–105, 1983.

[48] David Allcock. A multi-channel laser diagnostic system for trapped-ion quantum computing experiments. MSc Project Report, University of Oxford, 2007.

[49] A. Myerson. High precision qubit readout and microfabricated ion traps for quantum information processing. First Year Report, University of Oxford, August 2007.

[50] W. W. McAlpine and R. O. Schildknecht. Coaxial resonators with helical inner conductor. *Proc. Int. Radio. Eng.*, 47:2099–2105, 1959.

[51] J. P. Home. Trapping and cooling of ions for quantum information processing. First Year Report, 2005.

[52] D. J. Szwer. Personal communication. Report, 2007.

[53] S. C. Webster. *Raman Sideband Cooling and Coherent Manipulation of Trapped Ions*. PhD thesis, University of Oxford, 2005.

[54] I. Barin. *Thermochemical Data of Pure Substances*. VCH, Weinheim, 2 edition, 1993.

[55] D. A. Stevens. *The Quantum Manipulation of Ions*. PhD thesis, University of Oxford, 1999.

[56] John-Patrick Stacey. *Stabilization and Control In a Linear Ion Trap*. PhD thesis, University of Oxford, 2003.

[57] John D. Kalbfleisch and Ross L. Prentice. *The Statistical Analysis of Failure Time Data.* Wiley Series in Probability and Statistics. Wiley-Interscience, 2 edition, 2002.

[58] A. M. Steane. Personal communication. 2008.

[59] J. H. Wesenberg, R. J. Epstein, D. Leibfried, R. B. Blakestad, J. Britton, J. P. Home, W. M. Itano, J. D. Jost, E. Knill, C. Langer, R. Ozeri, S. Seidelin, and D. J. Wineland. Fluorescence during doppler cooling of a single trapped atom. *Phys. Rev. A*, 76,:053416, July 2007.

[60] R. J. Epstein, S. Seidelin, D. Leibfried, J. H. Wesenberg, J. J. Bollinger, J. M. Amini, R. B. Blakestad, J. Britton, J. P. Home, W. M. Itano, J. D. Jost, E. Knill, C. Langer, R. Ozeri, N. Shiga, and D. J. Wineland. Simplified motional heating rate measurements of trapped ions. *Physical Review A*, 76:033411, 2007.

[61] Q. A. Turchette, D. Kielpinski, B. E. King, D. Leibfried, D. M. Meekhof, C. J. Myatt, M. A. Rowe, C. A. Sackett, C. S. Wood, W. M. Itano, C. Monroe, and D. J. Wineland. Heating of trapped ions from the quantum ground state. *Phys. Rev. A*, 61(6):063418, May 2000.

[62] Ch. Roos, Th. Zeiger, H. Rohde, H. C. Nägerl, J. Eschner, D. Leibfried, F. Schmidt-Kaler, and R. Blatt. Quantum state engineering on an optical transition and decoherence in a paul trap. *Phys. Rev. Lett.*, 83(23):4713–4716, Dec 1999.

[63] J. P. Home. *Entanglement of Two Trapped-Ion Spin Qubits.* PhD thesis, University of Oxford, 2006.

[64] L. Deslauriers, P. C. Haljan, P. J. Lee, K-A. Brickman, B. B. Blinov, M. J. Madsen, and C. Monroe. Zero-point cooling and low heating of trapped Cd+111 ions. *Phys. Rev. A*, 70(4):043408, Oct 2004.

[65] L. Deslauriers, S. Olmschenk, D. Stick, W. K. Hensinger, J. Sterk, and C. Monroe. Scaling and suppression of anomalous heating in ion traps. *Physical Review Letters*, 97(10):103007, 2006.

[66] Ralph G. DeVoe and Christian Kurtsiefer. Experimental study of anomalous heating and trap instabilities in a microscopic 137*ba* ion trap. *Phys. Rev. A*, 65(6):063407, Jun 2002.

[67] Chr. Tamm, D. Engelke, and V. Bühner. Spectroscopy of the electric-quadrupole transition $^2S_{1/2}$(F=0)-$^2D_{3/2}$(F=2) in trapped 171Yb+. *Phys. Rev. A*, 61(5):053405, Apr 2000.

[68] F. Diedrich, J. C. Bergquist, Wayne M. Itano, and D. J. Wineland. Laser cooling to the zero-point energy of motion. *Phys. Rev. Lett.*, 62(4):403–406, Jan 1989.

[69] G. A. Baker and P. Graves-Morris. *Pad Approximants.* Cambridge University Press, 1996.